

A thesis for the degree of Ph.D. in Engineering

**Investigation into the effects of optical nonlinearities
on microresonator frequency combs**

February 2019

Graduate School of Science and Technology

Keio University

SUZUKI, Ryo



Keio University

Graduate School of Science and Technology
School of Integrated Design Engineering

**Investigation into the effects of optical nonlinearities
on microresonator frequency combs**

by

Suzuki, Ryo

A THESIS SUBMITTED
IN PARTIAL FULFILLMENT OF
THE REQUIREMENTS FOR THE DEGREE
Doctor of Philosophy

APPROVED, THESIS COMMITTEE:

T. Tanabe

Tanabe, Takasumi

F. Kannari

Kannari, Fumihiko

Takeshi Kinoshita

Kinoshita, Takeshi

Hiroyuki Sasada

Sasada, Hiroyuki

Andrew M. Weiner

Weiner, Andrew M.

Abstract

Microresonator frequency combs, which are known as microcombs or Kerr combs, can provide attractive characteristics for optical pulse lasers such as a low driving power thanks to their high quality factor (Q factor) and small mode volume, a compact size, and a high repetition frequency that corresponds to the cavity free spectral range (FSR). The repetition frequency of microcombs is typically in the 10 to 1000 GHz range, which is exceeding that of conventional optical pulse sources (<10 GHz). These characteristics are compatible with many practical applications including optical communications with wavelength division multiplexing, microwave oscillators, optical frequency synthesizers, and dual-comb spectroscopy and LiDAR.

A microcomb is formed inside a microresonator via four-wave mixing, which is driven by a continuous-wave pump laser. However, besides the four-wave mixing processes, other effects of optical nonlinearities occur owing to strong light-matter interactions in the dielectric microresonator. These effects sometimes help or disturb to generate a microcomb, and also change the properties including the repetition frequency, bandwidth, and coherence. In this thesis, the author studies the effects of cavity optomechanics, stimulated Raman scattering, and cross-phase modulation on microcombs. These understandings help to generate microcombs that have controlled-properties such as noises, operation wavelengths, spectral envelope shapes, and repetition frequencies.

Chapter 1 introduces the background to microresonators and microcombs to clarify the motivation behind this thesis. The basic generation scheme, previous researches, and microcomb applications are introduced. In addition, the related researches of effects of optical nonlinearities on microcombs are introduced.

Chapter 2 explains microresonator characteristics to make it easier to understand this thesis. The contents are basic theory of microresonators, optical coupling systems, fabrication processes of microresonators and tapered fibers, developed measurement methods for Q factors and cavity dispersions, and optical nonlinear processes in microresonators.

Chapter 3 explains the basic theory and measurement data of microcombs. The theory mainly deals with a Lugiato-Lefever equation, which can calculate microcomb formation inside a microresonator and provide an approximate analytical solution for a dissipative Kerr soliton. The measurement data includes microcomb spectra generated in three platforms (silica toroid, silica rod, and polished magnesium fluoride microresonators) and optical transmission with soliton steps while scanning the pump frequency.

Chapter 4 describes a study of cavity optomechanical behaviors on microcomb generation and demonstrates that it is possible to suppress cavity optomechanical parametric oscillations with the generation of a Turing pattern comb (microcomb) in an anomalous dispersion toroidal

microresonator.

Chapter 5 describes a study of Raman comb generation in a silica rod microresonator that has a cavity FSR in a microwave rate. The center wavelength is controlled via detuning and coupling optimizations. This study provides the explanation of the formation dynamics, of which understanding is needed to generate smooth and phase-locked Raman combs.

Chapter 6 is a numerically study of dual-comb generation and soliton trapping in a single microresonator, whose two transverse modes are excited with orthogonally polarized dual-pumping. The simulation model is described by using coupled Lugiato-Lefever equations, which take account of cross-phase modulation and the difference in repetition frequencies.

Chapter 7 summarizes the content of each chapter and discusses future work and the outlook for microcomb research.

Contents

Abstract	v
1 Introduction and motivation	1
1.1 Introduction of optical microresonators	1
1.2 Optical frequency combs in mode-locked lasers	2
1.3 Introduction of microresonator frequency combs (microcombs)	3
1.3.1 Microcomb generation in optical microresonators	4
1.3.2 Milestones in microcomb research	4
1.3.3 Microcomb applications	6
1.4 Related researches into effects of optical nonlinearities on microcombs	9
1.4.1 Cavity optomechanics	9
1.4.2 Stimulated Raman scattering	9
1.4.3 Cross-phase modulation between dual-comb	11
1.5 Motivation and chapter overview	12
2 Optical microresonators	15
2.1 Microresonator characteristics	15
2.1.1 Basic microresonator parameters	15
2.1.2 Optical coupling to microresonators	18
2.2 Fabrication of microresonators used in this thesis	20
2.2.1 Silica toroid microresonators	20
2.2.2 Silica rod microresonators	22
2.2.3 Polished magnesium fluoride microresonators	22
2.3 Tapered fiber coupling and quality factor measurement	23
2.3.1 Fabrication of tapered fibers	23
2.3.2 Quality factor measurement with a tapered fiber	24
2.3.3 Control of coupling condition between microresonator and fiber	28
2.3.4 Thermally induced resonance shift	28
2.4 Cavity dispersion	29
2.4.1 Finite element simulation for cavity dispersion	30
2.4.2 Cavity dispersion measurement	33
2.5 Optical nonlinear processes	35
2.5.1 Third order nonlinearities in dielectric materials	35

2.5.2	Optical nonlinear processes in microresonators	36
2.5.3	Cavity optomechanics	40
3	Microresonator frequency combs (microcombs)	41
3.1	Theory of microcomb formation dynamics	41
3.1.1	Spectrotemporal model: nonlinear coupled mode equation	41
3.1.2	Spatiotemporal model: Lugiato-Lefever equation	42
3.1.3	Microcomb formation via cascaded four-wave mixing	43
3.1.4	Analysis of soliton solution in a microresonator	46
3.2	Experimental observation of microcomb generation	47
3.2.1	Microcomb generation and formation in microresonators	49
3.2.2	Transmission and soliton steps while scanning pump laser	50
3.2.3	Linewidth of a generated comb line with and without optomechanical oscillations	51
4	Suppression of optomechanical parametric oscillation in a toroid microresonator assisted by a microcomb	55
4.1	Introduction	55
4.1.1	Basic theory of cavity optomechanics	55
4.1.2	Measurement and simulation of mechanical modes in toroid microresonators	59
4.1.3	Motivation	61
4.2	Experimental observation of suppression of optomechanical parametric oscillation	62
4.3	Discussion on experimental observations	65
4.3.1	Model of multi-optomechanical coupling	65
4.3.2	Excitation of mechanical mode with continuous-wave	65
4.3.3	Excitation of mechanical mode with microcomb	66
4.4	Measurement and calculation with a different toroid microresonator	68
4.5	Temporal behavior of transmission power with high pump power	71
4.6	Summary	72
5	Broadband gain induced Raman comb formation in a silica microresonator	73
5.1	Introduction	73
5.1.1	Raman response function in silica	73
5.1.2	Motivation	74
5.2	Raman comb generation in a silica rod microresonator	74
5.3	Peak transition via controlling detuning and coupling	77
5.4	Coupled mode equations with Raman processes	80
5.5	Summary	82
6	Theoretical study on dual-comb generation and soliton trapping in a single microresonator with orthogonally polarized dual-pumping	83
6.1	Introduction	83
6.1.1	Dual-comb generation scheme from a single resonator	83

6.1.2 Motivation	84
6.2 Simulation model	85
6.3 Numerical simulation results	86
6.4 Analysis of trapped soliton solution	90
6.4.1 Master equations and ansatzes	90
6.4.2 Trapped soliton solution in coupled Lugiato-Lefever equations	90
6.5 Summary	94
7 Summary and outlook	95
7.1 Summary of this thesis	95
7.2 Outlook	97
Appendix A Analysis of soliton solution in a single Lugiato-Lefever equation	99
Appendix B Delayed self-heterodyne measurement	101
Appendix C Dual-pump to a single transverse mode	103
Appendix D Coupling strength control with octagonal toroid microresonators	105
D.1 Introduction	105
D.2 Fabrication of octagonal silica toroid microresonators	106
D.3 Optical measurement of octagonal toroid microresonators	107
D.4 Calculation of coupling coefficient at zero gap with different microresonator structures	108
D.5 Summary	110
Appendix E Constants, symbols, and relations	111
Appendix F Abbreviations	113
Bibliography	115
Acknowledgements	129
List of publications and presentations	131

Chapter 1

Introduction and motivation

This chapter introduces the background of microresonators and microresonator frequency combs (microcombs) to clarify the motivation of this thesis. The basic generation scheme, important previous research, and microcomb applications are introduced. In addition, the related research into effects of optical nonlinearities on microcombs are introduced.

1.1 Introduction of optical microresonators

Developments of laser (light amplification by stimulated emission of radiation) technologies, which were first theoretically proposed by Charles H. Townes and Arthur L. Schawlow [1] and experimentally demonstrated by Theodore H. Maiman [2], improve our standard of living. The use of coherent light has opened up applications such as optical communications, material processing, precise measurements, and definitions of physical constants.

A laser mainly contains two elements: a gain medium and an optical resonator (cavity). Note that there are no significant difference between "resonator" and "cavity" in this thesis. The typical optical resonator is a Fabry-Pérot type, which consists of two mirrors with high reflectance in the air. To manipulate and modulate the resonant light, some optical elements (e.g. gain mediums, saturable absorbers, and dispersion compensation mirrors) are put on the resonator pathway. On the other hand, optical microresonators (microcavities) confine light in dielectric materials, which have a higher refractive index than surrounding materials. Since dielectric materials have third order optical nonlinearities (and also the second order optical nonlinearities in some materials) and resonant light is confined in the small structure, light-matter interactions can be efficiently created inside the microresonator [3,4]. The applications extend over microresonator frequency combs [5–7], biological and chemical sensors [8–10], optical signal processing [11], cavity quantum electrodynamics (QED) [12], and cavity optomechanics [13, 14].

Figure 1.1 shows images of typical microresonators: a whispering-gallery mode, a waveguide-integrated ring, and a fiber-based Fabry-Pérot microresonators. Whispering-gallery modes are resonances that confine light into the edge of a microresonator by total internal reflection, which is due to the difference of refractive indices between the resonator and its surrounding materials [15]. This resonant scheme can make use of various materials such as silica (SiO_2) [16–18], fluoride materials [19,20], sapphire (Al_2O_3) [21], polymers [22], chalcogenide glass [23], and

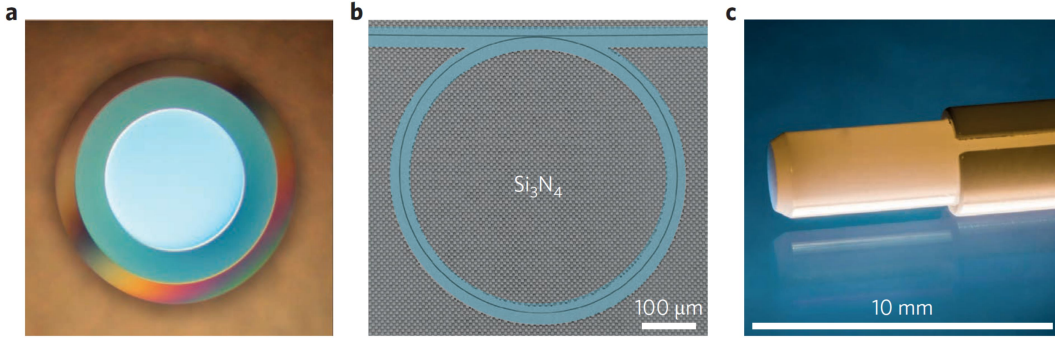


Fig. 1.1: Optical microresonators. (a) A whispering-gallery mode, (b) a waveguide-integrated ring, (c) a fiber-based Fabry-Pérot microresonators. Reprinted by permission from Macmillan Publishers Ltd.: A. M. Weiner, *Nat. Photonics* **11**, 533–535 (2017) [7]. Copyright 2017.

lithium niobate (LiNbO_3) [24]. These structures are fabricated by polishing or laser processing. Waveguide-integrated ring microresonators are fabricated by using CMOS-compatible processes, which can precisely control the structure and the resonant mode profiles. Also, simultaneous fabrication of a microresonator and a coupling waveguide is the one advantage for integration and realization of a stable coupling condition. The CMOS-compatible processes limit the materials, which are only silicon nitride (Si_3N_4) [25], silicon (Si) [26], high-index silica-glass [27], aluminium nitride (AlN) [28], aluminium gallium arsenide (AlGaAs) [29], and diamond [30]. Recently, fiber-based Fabry-Pérot microresonators, which consist of single-mode optical fibers whose facets are coated with zero group delay dielectric Bragg mirrors, have been reported [31]. This microresonator is direct-coupled to a input laser and compatible with other fiber elements. In this thesis, I used whispering-gallery mode microresonators made of silica and magnesium fluoride (MgF_2).

1.2 Optical frequency combs in mode-locked lasers

An optical frequency comb is laser light having discrete laser lines, that are equidistantly spaced and mutually coherent, in the frequency domain [32–35]. Frequency comb technologies provide a precise measurement method of optical frequencies, which is a drastic improvement and simplification of complex frequency chain systems [36]. Owing to their contributions to the development of laser-based precision spectroscopy and frequency combs, Theodor W. Hänsch and John L. Hall won the 2005 Nobel Prize in physics. In addition, frequency comb applications cover a lot of fields in research and industry, which are not only precise frequency measurement but also attosecond science, trace gas sensing, exoplanet searches, low noise microwave generation, distance measurement, and so on.

To use a frequency comb as an optical frequency ruler, it is required to know the precise frequencies of all comb lines that follow as

$$f_m = f_{\text{ceo}} + m f_{\text{rep}}, \quad (1.1)$$

where m is the large integer of around 10^6 order ($m \in \mathbb{N}$), f_{ceo} is the carrier-envelope offset

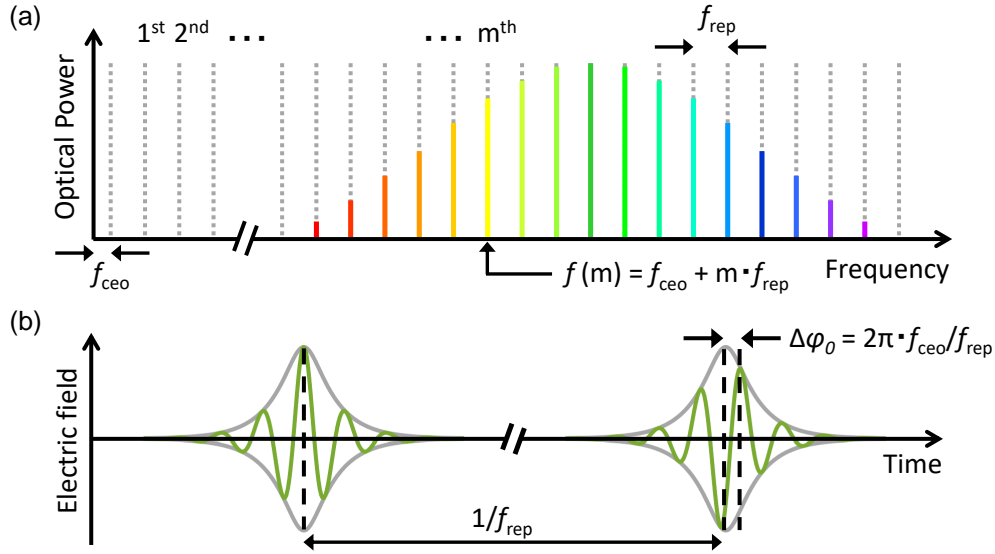


Fig. 1.2: (a) Optical spectrum and (b) pulse train in a mode-locked pulse laser. Since time and frequency domains are transformed via Fourier transformation, the repetition frequency of a pulse train is determined by the mode spacing of discrete comb lines. With the stabilization of f_{rep} and f_{ceo} , the absolute frequency is determined as follows: $f_m = f_{\text{ceo}} + m f_{\text{rep}}$. The carrier-envelope offset phase $\Delta\varphi_0$ of the pulse train depends on the ratio between f_{rep} and f_{ceo} .

frequency, and f_{rep} is the repetition frequency, as shown in Fig. 1.2. The repetition frequency is easy to measure by using a photodetector because it is typically around 100 MHz. On the other hand, the measurement of the carrier-envelope offset frequency needs a self-referencing technique. The self-referenced frequency comb consists of a mode-locked pulse laser (e.g. Ti:sapphire and fiber lasers), a highly nonlinear fiber (e.g. photonic crystal fibers), an f - $2f$ interferometer with a second-harmonic generation (SHG) crystal, and a reference microwave clock. The optical pulse train is launched to a highly nonlinear fiber, which broadens the spectral bandwidth to octave-spanning [37]. The octave-spanning comb includes comb lines that have frequencies of $f_{\text{ceo}} + m' f_{\text{rep}}$ and $f_{\text{ceo}} + 2m' f_{\text{rep}}$. The former frequency is doubled with a SHG crystal to $2f_{\text{ceo}} + 2m' f_{\text{rep}}$. In an f - $2f$ interferometer, the beatnote signal can provide the frequency difference as follows:

$$f_{\text{ceo}} = (2f_{\text{ceo}} + 2m' f_{\text{rep}}) - (f_{\text{ceo}} + 2m' f_{\text{rep}}). \quad (1.2)$$

The carrier-envelope offset and repetition frequencies are stabilized to a reference microwave clock, whose feedback loops usually control the cavity length and the angle of the end mirror (or pump power), respectively.

1.3 Introduction of microresonator frequency combs (micro-combs)

A microresonator frequency comb (known as a microcomb or a Kerr comb) is laser light that has a comb-like spectrum and is generated in a dielectric microresonator (e.g. made of silica, MgF_2 , and Si_3N_4) via cascaded four-wave mixing (FWM). Microcomb sources can provide attractive characteristics for optical pulse lasers such as a low driving power thanks to their high quality factor (Q factor) and small mode volume, a compact size, and a high repetition frequency that corresponds to the cavity free spectral range (FSR). The repetition frequency of microcombs is typically in the 10 to 1000 GHz range, which is exceeding that of conventional optical pulse sources (<10 GHz). These characteristics are compatible with many practical applications. This section introduces the microcomb generation scheme, important previous research, and applications.

1.3.1 Microcomb generation in optical microresonators

Figure 1.3(a) shows an illustration of the microcomb generation system with a dielectric microresonator driven by a continuous-wave (CW) laser through an external waveguide. The CW laser (input) is converted to the microcomb (output) via FWM because the intracavity power builds up in the microresonator thanks to its high-Q and small mode volume, and extends the threshold for FWM in the dielectric material. When the relative phases between the comb lines are zero, the output light in the time domain becomes an optical pulse train which is known as a soliton microcomb or a dissipative Kerr soliton (the detail is explained in §3.1.3).

Figures 1.3(b) and (c) are schematics of a conventional mode-locked and a microcomb lasers, respectively. A conventional mode-locked laser consists of a resonator, a saturable absorber, a gain medium, and a pump laser. The light in multiple frequencies are generated from a gain medium, that has a broad gain spectrum and is excited with a pump laser. Since the saturable absorber works to match the mutual coherence between the light in multiple frequencies, the output light becomes a mode-locked pulse train. Here, the mode spacing in the frequency domain (the repetition frequency in the time domain) corresponds to the cavity FSR (the roundtrip time in the resonator). On the other hand, a microcomb laser consists of a microresonator and a pump laser. The comb is converted from the CW pump laser, which works as a gain supplier and is a component of the comb spectrum. The relative phases between the comb lines become zero when the all comb lines propagate at the same group velocity inside the microresonator with balance between Kerr effects and anomalous dispersion (known as soliton propagation).

1.3.2 Milestones in microcomb research

The first important research for microcombs was reported in 2007 by Max-Planck-Institute for Quantum Optics (MPQ) [5], which discovered that cascaded FWM inside a microresonator has the potential to generate broadband and equally spaced comb lines in the frequency domain. Hence microcombs have been expected for novel optical frequency comb sources that have mode

1.3. Introduction of microresonator frequency combs (microcombs)

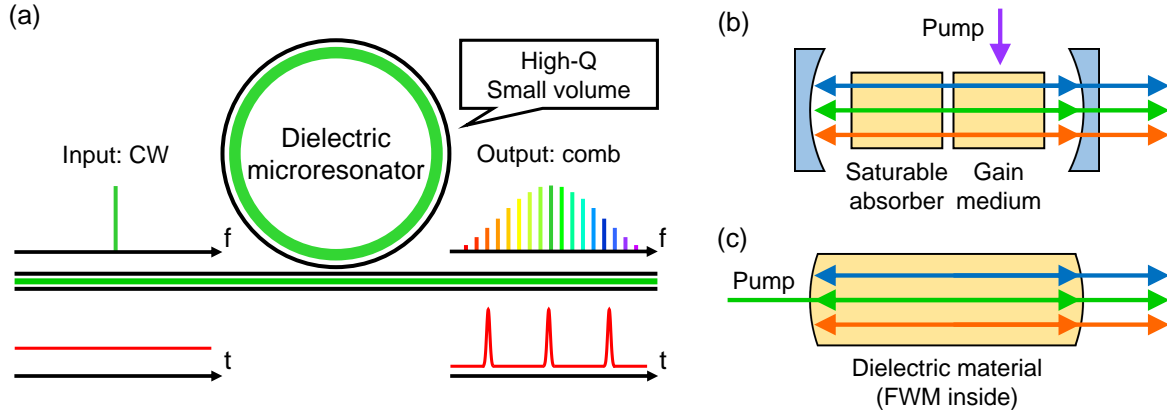


Fig. 1.3: (a) Illustration of the microcomb generation system with a dielectric microresonator driven by a CW laser through an external waveguide. The CW laser is converted to the microcomb via FWM with a low threshold thanks to its high-Q and small mode volume. When the relative phases between the comb lines are zero, the output light becomes a soliton pulse train. (b) Schematic of a conventional mode-locked laser, which consists of a resonator, a saturable absorber, a gain medium, and a pump laser. The pump laser excites the gain medium, which emits light in multiple frequencies. (c) Schematic of a microcomb laser, which consists of a dielectric microresonator and a pump laser. The comb is converted from the CW pump laser, which works as a gain supplier and is a component of the comb spectrum.

spacings over 10 GHz. To achieve the larger mode spacing is difficult with conventional pulse sources. However, at that time, the generated microcombs were not pulsed in the time domain. Against the problem, an optical temporal cavity soliton, which was first demonstrated in a fiber cavity [38], plays important roles for microcomb formation and achieving soliton microcombs (pulse generation). In 2013, soliton microcomb was demonstrated in a MgF_2 microresonator by Swiss Federal Institute of Technology in Lausanne (EPFL) [39], which provides sech^2 -shaped spectral envelope in the frequency domain and picoseconds order pulses in the time domain. To date, soliton microcomb generation [7, 40, 41] has been demonstrated in many platforms such as silica disk [42], silica rod [43], Si_3N_4 ring [44–46], AlN ring [47], and fiber-based Fabry-Pérot [31] microresonators.

As explained in §1.2, the carrier-envelope offset frequency in a frequency comb is stabilized by using a self-referencing technique with an octave-spanning comb. In microcomb sources, there are two approaches to obtain an octave-spanning comb. One approach is to generate coherent octave-spanning comb directly in a microresonator, which was demonstrated with a Si_3N_4 ring microresonator [48]. However, the octave-spanning comb generation typically requires a microresonator with a large mode spacing around 1 THz, which is not possible to measure using a photodetector. The other approach is to broaden the bandwidth of a microcomb outside by using a high nonlinearity fiber. The outside broadening was demonstrated with a silica disk microresonator with a 16.4 GHz cavity FSR [49]. In this previous research, the repetition and the carrier-envelope offset frequencies were both detected and stabilized. In the past two years or so, demonstrations of microcomb applications have been reported, which are

introduced in §1.3.3.

1.3.3 Microcomb applications

Optical communications

Technologies of wavelength division multiplexing (WDM) in coherent optical communications have been developed to meet demands for the large transmission capacity. Since, for long-haul communications, data channels need to locate within the wavelength range of optical amplifiers, WDM systems require small channel spacings that are typically from 10 to 100 GHz. Although distributed feedback (DFB) laser arrays are commonly used to generate the optical carriers, this system suffers from the channel frequency drift and the spectral overlap of neighboring channels. Therefore, all channel frequencies need to be controlled with individual heaters that make the system complex and costly. By using only a microresonator and a pump laser, microcombs can provide optical carriers for many channels that have the mode spacing of tens GHz. The microcomb system makes it easy to keep the channel spacings because the channel frequencies are determined by the microresonator resonances. Recently, the WDM data transmission system with bright soliton microcombs has been demonstrated by using Si_3N_4 ring microresonators and achieved the data rates of tens terabits per second [50]. Also, dark pulse microcombs have been used for WDM systems with Si_3N_4 ring microresonators that have normal dispersion [51]. Since dark pulse microcombs achieve high conversion efficiency, the system can provide high transmitted signal-to-noise ratios while using a pump power level of hybrid silicon lasers. In addition, it has been reported that WDM systems consist of Turing pattern microcombs (the comb state is explained in Chapter 3), which are generated with MgF_2 microresonators and robust against frequency and amplitude noise of the pump laser [52].

Spectroscopy and imaging

Conventional Fourier-transform spectroscopy, which consists of a Michelson-type interferometer with a movable mirror, is a powerful tool to measure absorption spectra of solids, liquids, and gases. The commercial instruments for molecular spectroscopy are widely used in industry and research fields. However, their applications are restricted only to monitoring slow phenomena because the scan rate is limited to a few hertz by the mechanical motion of the scanning mirror. To overcome this limitation, dual-comb spectroscopy was proposed, which replaces a movable mirror to an additional frequency comb laser [53, 54]. This replacement improves the scan rate by several orders of magnitude. In a dual-comb system, the resolution and the scan rate are determined by the pulse repetition frequency and the difference between the repetition frequencies. Since microcombs have high repetition frequencies, microcomb systems provide low resolution but a very fast scan rate (the higher repetition frequency permits the larger difference between the repetition frequencies). Such systems are compatible with spectroscopy for solids and liquids that have broad linewidths in absorption spectra. Some demonstrations of dual-comb spectroscopy with microcombs have been reported using silica disk [55], Si_3N_4 ring [56], and silicon ring [57] microresonators. Also, the demonstration of dual-comb imaging with microcombs has been reported using silica disk microresonators [58].

LiDAR

Light detection and ranging (LiDAR) is a technology to measure distances to targets, which has the advantages of high precision, long ranges, and fast scan rate. LiDAR systems can be applied to many industrial and scientific fields such as autonomous driving, industrial sensing, drone navigation, and meteorological observations. There are some approaches to providing LiDAR systems, such as utilizing an interferometer with lasers in multiple wavelengths, an electro-optically modulated CW laser, and a dual-comb laser [59]. Microcombs have the potential to realize dual-comb laser sources for LiDAR systems that have advantages including a compact size, low cost, and fast scan rates. As with dual-comb spectroscopy, the scan rate is determined by the difference of the repetition frequencies in two soliton microcombs. Recently, demonstrations of LiDAR with microcombs have been reported using silica disk [60] and Si₃N₄ ring [61] microresonators.

Astrocombs

Astronomical spectroscopy needs stable and accurate wavelength references to calibrate the radial velocity Doppler shift, which is obtained from stellar spectra, in the precision of 10 cm/s or smaller [62]. The conventional calibration method uses emission lines of hollow-cathode gas lamps. However, the irregular line spacings and drifts limit the detection in current spectrographs. Recently, optical frequency combs have been studied and adopted to the calibration source owing to their stability, accuracy, and broad bandwidth. However, conventional frequency comb sources consisting of Ti:sapphire and fiber lasers have too dense mode spacings, which are typically below 10 GHz, for spectrographs. Therefore, several stages of Fabry-Pérot cavities are required to filter out unnecessary comb lines, whose complexity and imperfect filtering induce measurement errors. Here, microcombs have the potential to provide calibration sources that have mode spacings of tens GHz and cover broad bandwidth from 380 nm to 2.4 μm. The microcomb-based calibration of spectrographs has been reported using a silica disk [63] and a Si₃N₄ ring [64] microresonators.

Optical frequency synthesizers

Optical frequency synthesizers can generate a coherent CW laser whose frequency is stabilized to an optical frequency comb [65]. The accuracy and wide range tunability help a lot of applications including frequency metrology and molecular spectroscopy. However, the size of optical frequency synthesizers is large because the frequency comb source occupies a large volume and requires complex experimental setup (e.g. a laser cavity and an f - $2f$ interferometer). Recently, optical frequency synthesizers towards on-chip integration have been developed with growing technologies of heterogeneously integrated photonics. A recent report utilized two microcombs, which were generated from two microresonators, to realize a reference comb whose repetition and carrier-envelope offset frequencies were stabilized [66]. The Si₃N₄ ring microresonator generated an octave-spanning microcomb that has the mode spacings of 1 THz. The silica disk microresonator generated a microcomb that has the mode spacing of 22 GHz. The octave-spanning microcomb is launched to a waveguide periodically poled lithium niobate

(PPLN) device in order to generate SHG for the detection of the carrier-envelope offset frequency. The 22 GHz microcomb filled the gaps between the 1 THz mode spacings to link the neighboring lines because 1 THz mode spacing is too large to detect the beatnote signal directly. In the future, it is expected that fully integrated optical frequency synthesizers for generating CW and also pulse lasers will be realized.

Microwave oscillators

Photonic microwave oscillators have the advantages of large bandwidth, large tunability, low transmission loss, and high reconfiguration [67]. Since microwave signals can be transformed from laser light in multiple frequencies by using a fast photodetector, frequency combs can generate low noise microwave signals thanks to their equally spaced comb lines [68]. However, such microwave oscillators with frequency combs are typically large in volume and high power consumption. Against the problems, microresonator-based microwave oscillators have been studied due to their potential for small and low power consumption devices. The laser light in multiple frequencies is generated inside a microresonator via nonlinear processes such as FWM, stimulated Raman scattering (SRS), and stimulated Brillouin scattering (SBS) [69–72]. The oscillation frequency is in the range up to tens of GHz. In this previous research, the microcomb, which is generated from a MgF_2 microresonator via FWM, can provide a very pure microwave signal with the phase noises of -60 dBc/Hz at 10 Hz, -90 dBc/Hz at 100 Hz, and -170 dBc/Hz at 10 MHz [69]. The phase noises of microwave signals depend on many parameters such as the thermal stability, pump intensity noise, and pump detuning.

Integration of microcomb sources

One challenge of practical microcomb applications is to integrate a microresonator and other optical devices including a pump laser and an optical input/output coupler. On-chip microresonators (e.g. Si_3N_4 rings) are compatible with the integration owing to the simultaneous fabrication of a microresonator and a coupling waveguide. In addition, it has the potential for full integration, including with pump lasers, thermal heaters, high nonlinearity waveguides, photodetectors, and other devices [66, 73, 74]. However, on-chip microresonators typically have lower Q factors that require high intense pumping to generate soliton microcombs. This problem inhibits the integration because integrable pump lasers can launch at only tens of milliwatts. On the other hand, integration of a whispering-gallery mode microresonator and a coupling waveguide (e.g. prisms and tapered fibers) has also been reported. Although whispering-gallery mode microresonators are not suitable for mass production, commercial optical devices with a prism-coupled microresonator already exist. This device is not microcomb sources but narrow linewidth lasers and optoelectronic oscillators [75].

1.4 Related researches into effects of optical nonlinearities on microcombs

Since a microcomb is generated with strong pumping to a high-Q microresonator, other optical nonlinear effects simultaneously cause in the microresonator [76]. The nonlinear effects can be used to manipulate the microcomb properties and formation, or sometimes disturb the stability and mutual coherence of microcombs. Hence, to reveal the influences of the optical nonlinearities helps to achieve stable microcomb sources whose parameters are well controlled. The three following sections introduce previous researches of effects of optical nonlinearities on microcombs, which are related to this thesis.

1.4.1 Cavity optomechanics

Cavity optomechanics is the phenomenon that involves interaction between light and mechanical motion through radiation pressure [13, 14, 77]. The radiation pressure is caused by pushing the microresonator's boundary with the high intense light. In a microresonator, a blue-detuned pumping (the pump has higher frequency than the resonance) drives optomechanical parametric oscillations (OMPOs), which modulates the resonance frequency and changes the comb line frequencies. The threshold power for OMPO becomes lower when the oscillation frequency and optical cavity decay rate are close value, for example, in a silica toroid [78] and a calcium fluoride (CaF₂) [79] microresonator. In such a microresonator system, OMPOs can still be present on microcomb generation and induce frequency noises whose frequency extends to 10 MHz [80]. There are few research on relation between microcomb and cavity optomechanics, which is important for suppression of frequency noises in microcombs, except for a study on temporal behavior of OMPO under microcomb generation [81]. In many previous studies of cavity optomechanics using a toroid microresonator, the oscillation modes were excited with a low pump power that was much smaller than the threshold power for FWM. Although the cavity optomechanical behavior in microcomb generation has been reported [81], it has not been well understood. The strong pump light generates a microcomb inside the microresonator, which leads to multi-optomechanical coupling with the resonances.

1.4.2 Stimulated Raman scattering

Stimulated Raman scattering (SRS) is an optical nonlinear process that can generate red-shifted light from pump light via the interaction between light and molecular vibrations. SRS can provide lasing action and optical amplification using very high intense pump. Therefore, previous works relied on pulse excitation for Raman lasing [82–84]. On the other hand, optical microresonators with a high-Q and a small mode volume enables us to demonstrate low threshold lasing with CW pumping. Indeed, the microresonator-based Raman lasing with a CW pump has been reported using silica [85–90], silicon [91, 92], fluoride materials [71, 93, 94], and even other materials [95–98].

Since dielectric materials for microresonators (e.g. silica, MgF₂, and Si₃N₄) typically have

broader Raman gain than the cavity FSR, Raman scattering strongly influences on microcomb properties and is sometimes used for microcomb generation. The influences of Raman scattering on microcombs have been studied, including spectrum broadening [99, 100], self-frequency shift of a soliton [101, 102], trigger for FWM generation [103], gain competition between modulation instability and Raman [104, 105], and comb generation via SRS [71, 89, 90, 94, 106]. In particular, comb generation via SRS (Raman comb) has much different approach from that via FWM and has unique properties including the operation wavelength (e.g. in visible wavelength) and mutual coherence between the comb lines (Fig. 1.4).

Recently, a phase-locked Raman comb was demonstrated using a crystalline microresonator in the weak normal dispersion regime [71, 94]. Even a soliton Raman comb is demonstrated in a silica disk microresonator at the anomalous dispersion regime, by transferring a FWM comb to a long wavelength regime via Raman processes [90]. Although microresonator-based FWM combs usually require anomalous dispersion, Raman combs have an advantage that can be generated in the normal dispersion because SRS occurs regardless of the dispersion. Phase-locked Raman combs can be used for applications such as compact pulse laser sources, sensors, optical clocks, and coherence tomography. Despite these various potential applications, methods how to control the operation wavelength have not been well studied.

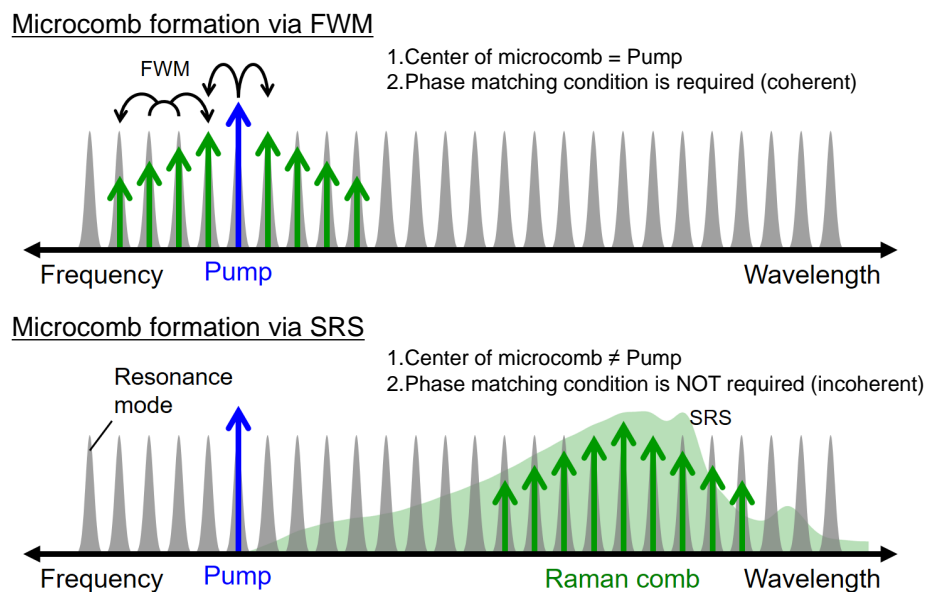


Fig. 1.4: Illustrations of microcomb formation via FWM and SRS. A Raman comb forms in a microresonator induced by broadband Raman gain spectrum of the host material that covers multiple resonance modes. Since FWM needs to satisfy with a phase matching condition, a microcomb via FWM can be mutually coherent. On the other hand, basically, a microcomb via SRS is mutually incoherent because SRS does not require a phase matching condition. However, in some previous researches, coherent Raman comb generation has been reported in a microresonator.

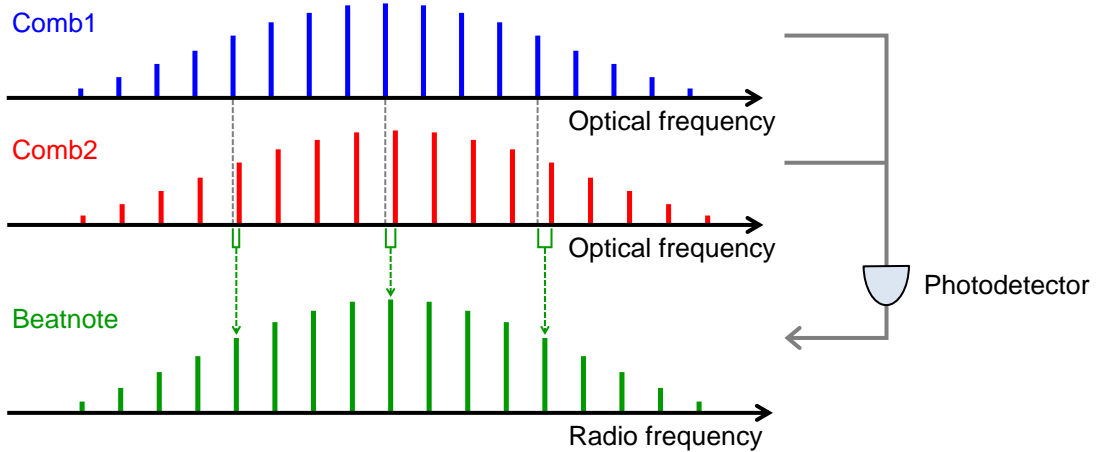


Fig. 1.5: Dual-comb in the terahertz scale and comb-like beatnote in the megahertz scale. Two combs with slightly different repetition frequencies are down-converted to the beatnote signal by detecting with a photodetector. The beatnote is useful to monitor the absorption and other variations through the dual-comb light. This is because each comb line in the terahertz scale corresponds to the each beatnote line in the megahertz scale, that is compatible with electrical equipments.

1.4.3 Cross-phase modulation between dual-comb

Optical frequency comb sources (and also optical pulses sources) have pulse trains in the time domain and broadband spectrum in the frequency domain. The paired comb source having slightly different repetition frequencies, that is known as dual-comb, can provide advantages such as high resolution, high sensitivity, and high data acquisition speed in optical spectroscopy and ranging. For example, the scan rate of a dual-comb spectrometer is several orders of magnitude faster than that of a Fourier transform spectrometer using a Michelson interferometer. This is because the second comb in a dual-comb system works as a reference and scan the delay automatically, instead of mechanically scanning the mirror in a Michelson interferometer. In the frequency domain, two combs in the terahertz scale can be down-converted to comb-like beatnote signal in the megahertz scale by detecting with a photodetector as shown in Fig. 1.5.

In a dual-comb system, which utilizes two types of optical pulse trains with slightly different repetition frequencies, microcomb platforms can achieve fast scan rates for spectroscopy [55, 57] and LiDAR [60, 61]. This is because a dual-comb system with optical pulse trains at high repetition frequencies can allow the large difference between the repetition frequencies, which corresponds to the scan rate in measurement systems, with low noise. Hence the key parameter is the repetition frequency of each soliton microcomb in the time domain, which corresponds to the mode spacing between comb lines in the frequency domain.

Recently, dual-comb generation in a single microresonator attracts much attention [55, 57, 61, 107–112] for dual-comb applications including spectroscopy and LiDAR. An experimental demonstration of dual-comb solitons in a single microresonator has been realized by utilizing clockwise and counter-clockwise directions [90] and spatially different transverse modes [111]. However, it is still challenging to generate dual-comb solitons because the two propagating

solitons interact and result in modulation of repetition frequencies through cross-phase modulation (XPM). XPM is one of Kerr effects and modulates the phase of one light with another light. In addition, although a theoretical model that takes account of XPM and the difference between repetition frequencies has been developed [108], the results of simulation and analysis for dual-comb solitons have not been well considered.

1.5 Motivation and chapter overview

A microcomb is formed inside a microresonator via FWM, which is driven by a CW pump laser. However, besides the FWM processes, other effects of optical nonlinearities occur owing to strong light-matter interactions in the dielectric microresonator. These effects sometimes help or disturb to generate a microcomb, and also change the properties including the repetition frequency, bandwidth, and coherence. In this thesis, the author studies the effects of cavity optomechanics, SRS, and XPM on microcombs. These understandings help to generate microcombs that have controlled-properties such as noises, operation wavelengths, spectral envelope shapes, and repetition frequencies.

This thesis consists of seven chapters and is organized as follows:

Chapter 1 introduces the background to microresonators and microcombs to clarify the motivation behind this thesis. The basic generation scheme, previous researches, and microcomb applications are introduced. In addition, the related researches of effects of optical nonlinearities on microcombs are introduced.

Chapter 2 explains microresonator characteristics to make it easier to understand this thesis. The contents are basic theory of microresonators, optical coupling systems, fabrication processes of microresonators and tapered fibers, developed measurement methods for Q factors and cavity dispersions, and optical nonlinear processes in microresonators.

Chapter 3 explains the basic theory and measurement data of microcombs. The theory mainly deals with a Lugiato-Lefever equation (LLE), which can calculate microcomb formation inside a microresonator and provide an approximate analytical solution for a dissipative Kerr soliton. The measurement data includes microcomb spectra generated in three platforms (silica toroid, silica rod, and polished magnesium fluoride microresonators) and optical transmission with soliton steps while scanning the pump frequency.

Chapter 4 describes a study of cavity optomechanical behaviors on microcomb generation and demonstrates that it is possible to suppress cavity optomechanical parametric oscillations with the generation of a Turing pattern comb (microcomb) in an anomalous dispersion toroidal microresonator.

Chapter 5 describes a study of Raman comb generation in a silica rod microresoator that has a cavity FSR in a microwave rate. The center wavelength is controlled via detuning and coupling optimizations. This study provides the explanation of the formation dynamics, of which understanding is needed to generate smooth and phase-locked Raman combs.

Chapter 6 is a numerical study of dual-comb generation and soliton trapping in a single microresonator, whose two transverse modes are excited with orthogonally polarized dual-pumping. The simulation model is described by using coupled LLEs, which take account of

XPM and the difference in repetition frequencies.

Chapter 7 summarizes the content of each chapter and discusses future work and the outlook for microcomb research.

Chapter 2

Optical microresonators

This chapter explains microresonator characteristics to make it easier to understand this thesis. The contents are basic theory of microresonators, optical coupling systems, fabrication processes of microresonators and tapered fibers, developed measurement methods for Q factors and cavity dispersions, and optical nonlinear processes in microresonators.

2.1 Microresonator characteristics

2.1.1 Basic microresonator parameters

Resonance frequencies

Optical resonators have the discrete resonance frequency ω_m , which is related to the optical cavity length nL . m is the mode number ($m \in \mathbb{N}$), n is the effective refractive index, and L is the cavity length. The internal electric field $E(z, t)$ is written as

$$E(z, t) = E_0 \exp\{i(kz - \omega_m t)\}, \quad (2.1)$$

where E_0 is the amplitude and k is the propagation constant. Since the phase of resonant light shifts $2\pi m$ per roundtrip ($kL = 2\pi m$), the resonance wavelength λ_m and angular frequency ω_m satisfy the following equations:

$$\lambda_m = \frac{nL}{m}, \quad (2.2)$$

$$\omega_m = \frac{2\pi mc}{nL}. \quad (2.3)$$

Here c is the speed of light. In the case of no dispersion (i. e. the effective refractive index does not depend on the frequency), the resonance frequencies have an equal mode spacing D_1 (in units of rad·Hz) as follows: $\omega_m = mD_1$. The cavity FSR is inverse to the roundtrip time as $t_r^{-1} = D_1/2\pi$ and the optical cavity length has the relation to the roundtrip time as $ct_r = nL$. The series of the resonance modes are known as transverse mode or mode family, and have the same mode profile and the polarization.

Cavity dispersion

The cavity dispersion is a parameter to represent that the effective refractive index depends on the frequency, the resonance mode profile, and the polarization in a microresonator. Hence, cavity dispersion is determined by the material and geometrical dispersions. The material dispersion follows a Sellmeier equation that determines the refractive index in the medium. The geometrical dispersion can be controlled by changing the microresonator structure because the mode profiles have different occupancies of optical intensity inside the medium. For example, a large amount of evanescent fields outside the microresonator leads to less effective refractive index.

As explained above, resonance frequencies have equal mode spacings when not taking account of cavity dispersion. However, cavity dispersion changes the mode spacings depending on the frequency. The resonance frequencies can be expressed with a relative mode number μ ($\mu \in \mathbb{Z}$) that is obtained from the absolute mode number m . The center mode number is defined as $\mu = 0$, which corresponds to the pump mode for microcomb generation. The resonance angular frequency ω_μ and the frequency f_μ are written with Taylor-expanded equations:

$$\begin{aligned}\omega_\mu &= \omega_0 + D_1\mu + \frac{1}{2}D_2\mu^2 + \frac{1}{6}D_3\mu^3 + \dots \\ &= \omega_0 + D_1\mu + D_{\text{int}}(\mu),\end{aligned}\quad (2.4)$$

$$\begin{aligned}f_\mu &= f_0 + d_1\mu + \frac{1}{2}d_2\mu^2 + \frac{1}{6}d_3\mu^3 + \dots \\ &= f_0 + d_1\mu + d_{\text{int}}(\mu).\end{aligned}\quad (2.5)$$

Figure 2.1 is an illustration to explain Eq. (2.4). D_1 is the cavity FSR that means light in the frequency ω_0 circulates in the microresonator at the roundtrip time $t_r = (D_1/2\pi)^{-1}$. D_2 and D_3 represent second and third order dispersion, respectively. D_{int} includes all dispersion terms. The higher order dispersion can be neglected in many cases because of the relation: $D_2 \gg D_3 \gg \dots$. The important point for microcomb generation is the sign of D_2 , where $D_2 > 0$ ($D_2 < 0$) denotes anomalous (normal) dispersion.

In many optical fiber researches, dispersion is expressed with group velocity dispersions (β_2

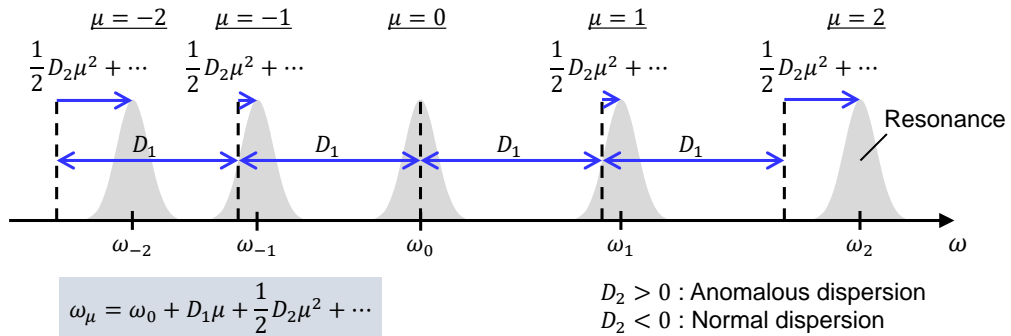


Fig. 2.1: Resonance frequencies taking cavity dispersion into account. This figure summarizes Eq. (2.4). Gray Lorentzian shapes represent resonance modes whose positions are different from black dashed lines (that have equal spacings) due to the cavity dispersion.

and β_3), which are related to D_1 and D_2 values:

$$\beta_2 = -\frac{nD_2}{cD_1^2}, \quad (2.6)$$

$$\beta_3 = \frac{3nD_2^2}{cD_1^4} - \frac{nD_3}{cD_1^3} \approx -\frac{nD_3}{cD_1^3}. \quad (2.7)$$

Cavity dispersion is a critical parameter in microcomb research for the initial comb generation, comb bandwidth, and mode-locking. The methods of measurement and calculation are introduced in §2.4.

Cavity decay rate and quality factor

The performance of each resonance mode is expressed with a cavity decay rate κ , which is related to an intrinsic decay rate κ_i and a coupling rate to the external waveguide κ_c as follows: $\kappa = \kappa_i + \kappa_c$. The intrinsic decay rate includes loss factors including scattering at the microresonator surface, absorption and scattering inside the material, and the radiation at the bending points. The coupling efficiency is determined by the relation between the intrinsic decay rate and the coupling rate (the detail is explained in §2.1.2). The intracavity optical energy $U_{\text{cav}}(t)$ decays exponentially:

$$U_{\text{cav}}(t) = U_{\text{cav}}(0) \exp(-\kappa t). \quad (2.8)$$

In general, the performance of a resonator is expressed with a quality factor (Q factor) Q and a finesse \mathcal{F} . A Q factor is defined as

$$Q = 2\pi \frac{(\text{Intracavity optical energy})}{(\text{Energy loss per optical cycle})} = 2\pi \frac{U_{\text{cav}}(t)}{-\frac{dU_{\text{cav}}(t)}{dt} \frac{2\pi}{\omega_0}} = \frac{\omega_0}{\kappa}. \quad (2.9)$$

Hence a Q factor can be determined by the cavity decay rate κ in the time domain, which corresponds to the full width at half maximum (linewidth) of the resonance mode in the frequency domain. The shape of a resonance mode is a Lorentzian function, which is explained in §2.1.2. The photon lifetime τ_{cav} is defined as $\tau_{\text{cav}} = \kappa^{-1}$, which can be evaluated by the decay of output power from a microresonator in the time domain. The finesse is defined as $\mathcal{F} = D_1/\kappa$, where $\mathcal{F} \gg 1$ denotes that each resonance mode can be distinguished.

Effective mode area

One advantage of microresonator platforms is to confine light in the small area and volume. The effective mode area A_{eff} is determined by a resonant mode profile:

$$A_{\text{eff}} = \frac{(\iint |E|^2 dA)^2}{\iint |E|^4 dA}, \quad (2.10)$$

where $|E|^2$ corresponds to the optical intensity. The effective mode volume V_{eff} can be expressed as $V_{\text{eff}} = A_{\text{eff}}L$.

2.1.2 Optical coupling to microresonators

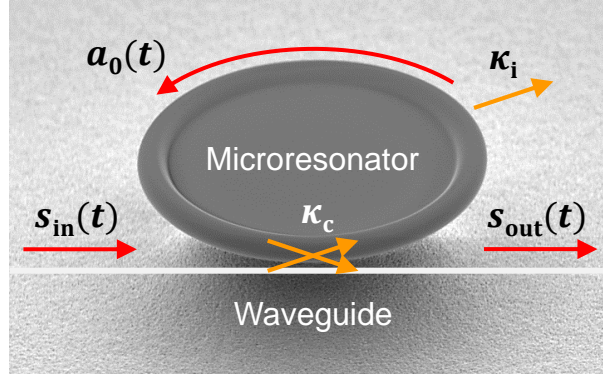


Fig. 2.2: Optical coupling system between a microresonator and a coupling waveguide. $a_0(t)$ is the intracavity field, $s_{\text{in}}(t)$ and $s_{\text{out}}(t)$ are the input and output fields, respectively. κ_i and κ_c are the intrinsic decay and coupling rates, respectively.

Optical input and output between a microresonator and a coupling waveguide are performed through an evanescent field. The typical coupling waveguides are optical tapered fibers, pigtailed fibers, prisms, and on-chip waveguides. A coupled mode equation for single resonance mode is written with a light field $A_0(t)$, which is normalized as that $|A_0(t)|^2$ corresponds to the number of intracavity photons at the resonance frequency ω_0 as

$$\frac{dA_0(t)}{dt} = -\frac{\kappa}{2}A_0(t) - i\omega_0 A_0(t) + \sqrt{\kappa_c}s_{\text{in}}(t)\exp(-i\omega_p t), \quad (2.11)$$

where $s_{\text{in}}(t)$ is the input field to the waveguide and ω_p is the pump frequency. Then, the phase transformation is applied as $a_0(t) = A_0(t)\exp(i\omega_p t)$ that can rewrite Eq. (2.11) to

$$\frac{da_0(t)}{dt} = -\frac{\kappa}{2}a_0(t) + i(\omega_p - \omega_0)a_0(t) + \sqrt{\kappa_c}s_{\text{in}}(t). \quad (2.12)$$

In addition, the output field $s_{\text{out}}(t)$ is given by

$$s_{\text{out}}(t) = \sqrt{\kappa_c}a_0(t) - s_{\text{in}}(t). \quad (2.13)$$

For the stationary-state analysis, the left-hand side in Eq. (2.12) is set to zero and $a_0(t)$, $s_{\text{in}}(t)$, and $s_{\text{out}}(t)$ in Eqs. (2.12) and (2.13) are regarded as time independent. Equations (2.12) can be transformed to

$$a_0 = \frac{\sqrt{\kappa_c}}{\frac{1}{2}\kappa - i\Delta\omega_0}s_{\text{in}}, \quad (2.14)$$

$$|a_0|^2 = \frac{\kappa_c}{\frac{1}{4}\kappa^2 + \Delta\omega_0^2}|s_{\text{in}}|^2, \quad (2.15)$$

where $\Delta\omega_0 = \omega_p - \omega_0$. Equations (2.14) and (2.15) represent the relation between the intracavity and input fields. Since $|a_0|^2$ corresponds to the number of photon stored inside the

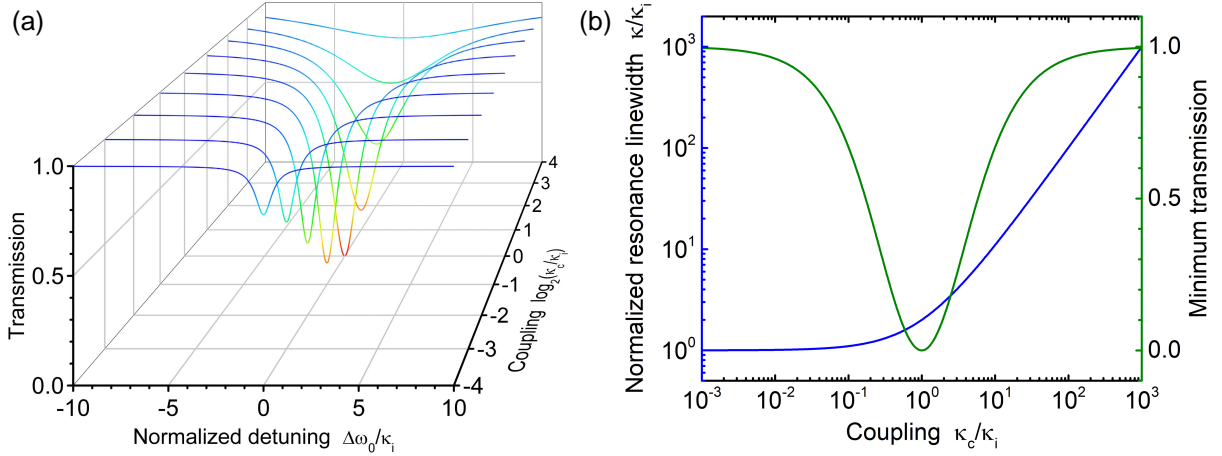


Fig. 2.3: Calculation results with Eq. (2.15). (a) Transmission of resonance modes as a function of a coupling parameter. $\kappa_c/\kappa_i = 1$ represents a critical coupling condition. (b) Normalized resonance linewidth (blue) and minimum transmission (green) as a function of a coupling parameter.

microresonator, the intracavity optical power P_{cav} can be obtained from Eq. (2.15). Also, the optical power in the coupling waveguide (P_{in} and P_{out}) can be obtained from $|s_{\text{in}}|^2$ and $|s_{\text{out}}|^2$ that correspond to the number of photons passing the waveguide per second.

$$P_{\text{cav}} = \hbar\omega_p |a_0|^2 \times (D_1/2\pi), \quad (2.16)$$

$$P_{\text{in(out)}} = \hbar\omega_p |s_{\text{in(out)}}|^2, \quad (2.17)$$

where \hbar is the Planck constant divided by 2π . In experiments, microresonators are evaluated by monitoring the relation between input and output fields, which provides parameters of the cavity linewidth, transmission, and phase response:

$$\frac{s_{\text{out}}}{s_{\text{in}}} = \frac{\frac{1}{2}(\kappa_c - \kappa_i) + i\Delta\omega_0}{\frac{1}{2}(\kappa_c + \kappa_i) - i\Delta\omega_0} = \frac{\frac{1}{2}(\frac{\kappa_c}{\kappa_i} - 1) + i\frac{\Delta\omega_0}{\kappa_i}}{\frac{1}{2}(\frac{\kappa_c}{\kappa_i} + 1) - i\frac{\Delta\omega_0}{\kappa_i}}, \quad (2.18)$$

$$\left| \frac{s_{\text{out}}}{s_{\text{in}}} \right|^2 = \frac{\frac{1}{4}(\kappa_c - \kappa_i)^2 + \Delta\omega_0^2}{\frac{1}{4}(\kappa_c + \kappa_i)^2 + \Delta\omega_0^2} = \frac{\frac{1}{4}(\frac{\kappa_c}{\kappa_i} - 1)^2 + (\frac{\Delta\omega_0}{\kappa_i})^2}{\frac{1}{4}(\frac{\kappa_c}{\kappa_i} + 1)^2 + (\frac{\Delta\omega_0}{\kappa_i})^2}. \quad (2.19)$$

In this thesis, I use the coupling parameters η and K that are defined as $\eta = \kappa_c/\kappa$ and $K = \kappa_c/\kappa_i$, respectively. The optical coupling is distinguished in three conditions: under ($K < 1$, $\eta < 0.5$), critical ($K = 1$, $\eta = 0.5$), and over ($K > 1$, $\eta > 0.5$) coupling conditions. The transmission of a resonance is described by Eq. (2.18), whose calculation examples are shown in Fig. 2.3. As shown in Eq. (2.18) and Fig. 2.3, the transmission has a Lorentzian function, which can be transformed from an exponential function by using Fourier transformation. By considering the build-up efficiency, critical coupling is an ideal condition, which can be optimized by controlling the coupling rate κ_c . Figure 2.4 shows transmission (blue) and phase (red) of a resonance mode in three coupling conditions (under, critical, and over coupling).

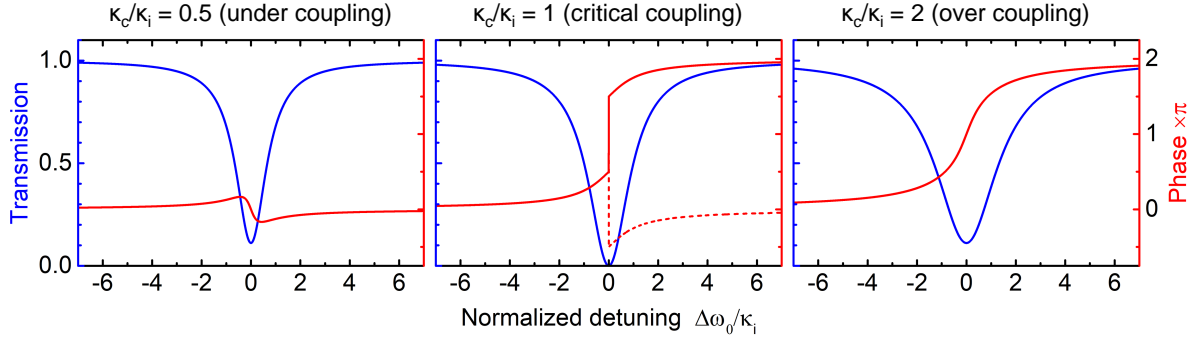


Fig. 2.4: Calculation results with Eqs. (2.14) and (2.15) in three different coupling conditions. The blue and red lines represent the transmission and the phase, respectively.

2.2 Fabrication of microresonators used in this thesis

In this thesis, I use three types of microresonators to generate microcombs: silica toroid, silica rod, and polished MgF_2 microresonators. This section explains the fabrication processes. Table 2.1 introduces the material properties of silica, MgF_2 , and other commonly used optical materials.

2.2.1 Silica toroid microresonators

Silica toroid microresonators were developed in 2003 by California Institute of Technology (Caltech) [17] and used to demonstrate equally spaced microcomb generation in the first important report in 2007 by Max-Planck-Institute for Quantum Optics (MPQ) [5]. The advantages of a toroid microresonator are on-chip fabrication, a high-Q (~ 100 million), and a small mode volume. Carbon dioxide (CO_2) laser reflow processes make the smooth toroidal surface that reduces scattering losses and achieves a high-Q.

Figure 2.5 shows the fabrication processes of a toroid microresonator, including photolithography, silicon etching with xenon difluoride (XeF_2), and CO_2 laser reflow. First, (a) a silicon wafer with an silica layer of $2\ \mu\text{m}$ thickness is prepared. Second, (b) photolithography and silica etching with a buffered hydrogen fluoride (HF) forms circular silica disks on the silicon wafer. The reaction is expressed as $\text{SiO}_2 + 6\text{HF} \rightleftharpoons \text{H}_2\text{SiF}_6 + 2\text{H}_2\text{O}$. The silica disk have diameters that are typically from 50 to $200\ \mu\text{m}$. Third, (c) silicon etching with XeF_2 forms the structure of a

Table. 2.1: Microresonator material properties [113–115].

	Fused SiO_2	MgF_2	CaF_2	Si_3N_4
n	1.44	1.38 (e), 1.37 (o)	1.43	1.98
$n_2 [\times 10^{-20}\ \text{m}^2/\text{W}]$	2.2	0.9	1.9	25
$(1/L)dL/dT [\times 10^{-6}\ /\text{K}]$	0.55	13.6 (e), 9.4 (o)	18.9	2.1 (e), 1.1 (o)
$(1/n)dn/dT [\times 10^{-6}\ /\text{K}]$	7.3	0.25 (e), 0.6 (o)	-8.0	30
Transparent wavelength [μm]	0.3-2.6	0.13-8.0	0.15-8.5	0.40-7.5
Typical microresonator Q	10^7 - 10^8	10^8 - 10^9	10^8 - 10^9	10^6 - 10^7

silica disk on a silicon pillar, which can confine light in a whispering-gallery mode at the edge of the silica disk. This reaction follows $2\text{XeF}_2 + \text{Si} \rightleftharpoons 2\text{Xe} + \text{SiF}_4$. Optimizing the ratio between diameters of the silica disk and the silicon pillar is a key to achieve a high-Q after forming the toroidal shape. Finally, (d) the CO_2 laser beam that is exposed to the silica disk from the top can melt only the edge of the silica disk because the silicon pillar works as a heat sink. The laser reflow process forms the toroidal shape that has a smooth surface. Typically, the Q factor improves from hundreds thousand in a disk to tens million in a toroid.

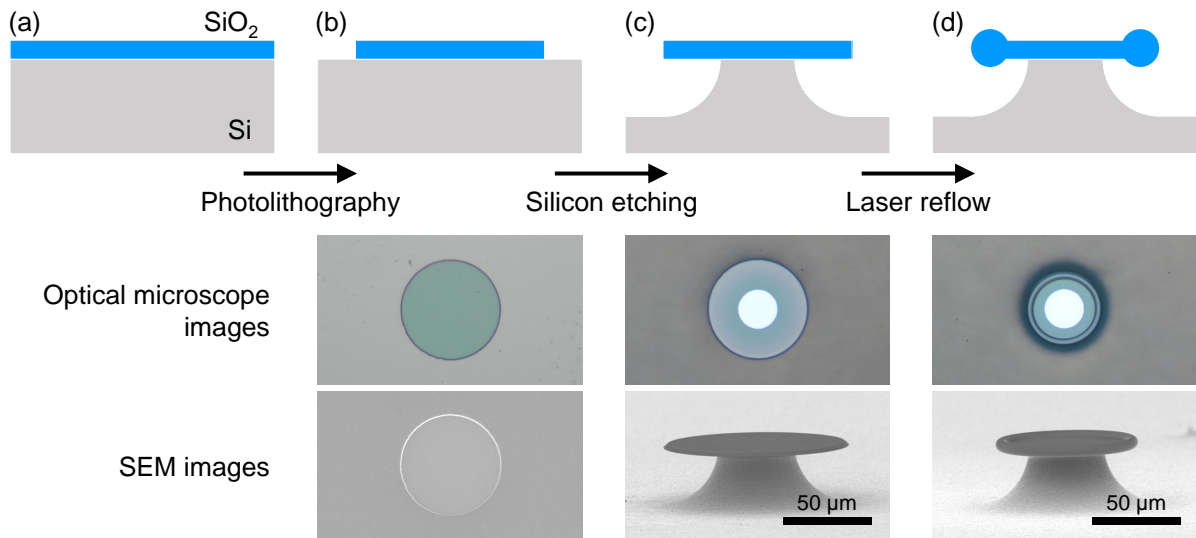


Fig. 2.5: Fabrication processes of a silica toroid microresonator. Optical microscope and scanning electron microscope (SEM) images are shown for each fabrication step. (a) Silicon wafer with a silica layer of 2 μm thickness. (b) Circular silica disk on the silicon wafer. (c) Circular silica disk on a silicon pillar. (d) Silica toroid microresonator, whose toroidal shape is formed at the edge of the silica disk by using a CO_2 laser reflow process.

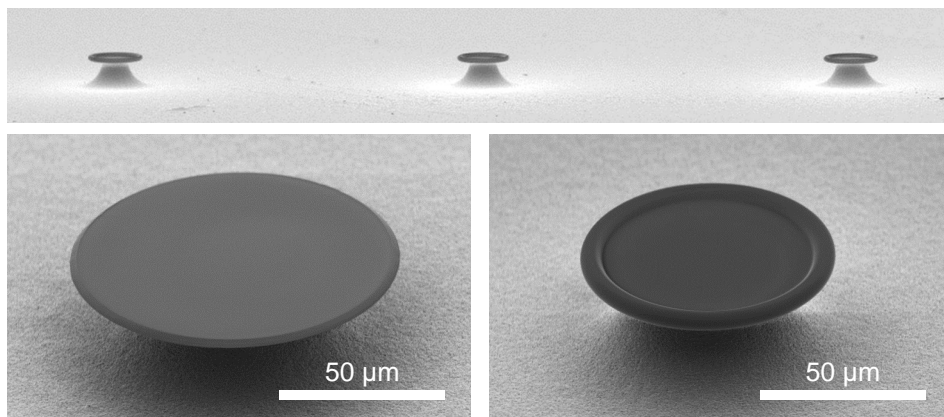


Fig. 2.6: SEM images of silica toroid and disk microresonators.

2.2.2 Silica rod microresonators

Silica rod microresonators were developed in 2013 by National Institute of Standards and Technology (NIST) [116], which have the advantage of high-Q achievability (over 100 million), easy fabrication processes, and a wide range of cavity FSR that covers from a few to hundreds of gigahertz.

Figure 2.7 shows the fabrication processes of a silica rod microresonator. First, (a) a silica rod containing low OH (<10 ppm) and other impurities is prepared and mounted on an air spindle. Second, (b) a CO₂ laser beam is focused on the silica rod surface with a zinc-selenide lens (50 mm focal length) while the silica rod rotates. By scanning the focusing position along to the rod axis, a diameter of the microresonator can be controlled by melting the material. Finally, (c) the CO₂ laser beam is focused on the two positions of the silica rod and forms the resonator shape as shown in Fig. 2.7(d). In the steps of (b) and (c), becoming clouded in silica should be avoided because it reduces the Q. The clouded silica can be observed at other than the resonator part in Fig. 2.7.

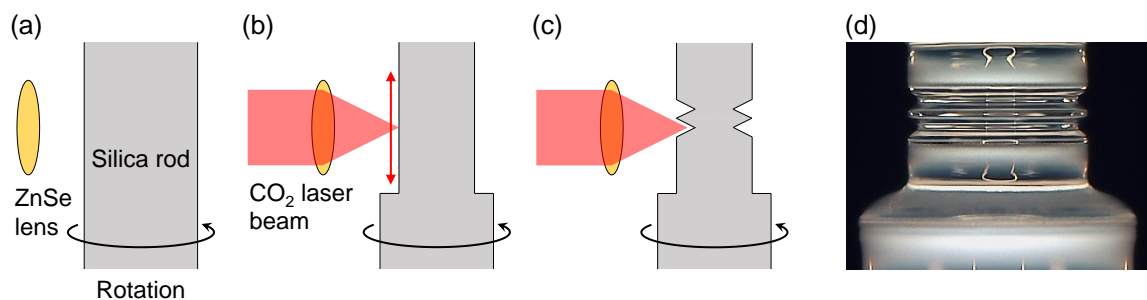


Fig. 2.7: Fabrication processes of a silica rod microresonator. (a) Silica rod is mounted and rotated on an air spindle. (b) CO₂ laser beam is focused on the surface of the silica rod. The focus position is scanned to melt the silica and control the diameter. (c) Microresonator structure is formed by focusing the laser beam at two positions. (d) Optical microscope image of a silica rod microresonator.

2.2.3 Polished magnesium fluoride microresonators

Polished magnesium fluoride (MgF₂) microresonators are ultrahigh-Q microresonators, which were used to demonstrate soliton microcomb generation in the first important report by EPFL [39]. This microresonator has the advantages of ultrahigh-Q (~1 billion) and high thermal stability thanks to its small thermo-optic coefficient. On the other hand, it is difficult to fabricate microresonators with a small diameter because of hand-cutting and polishing processes.

Figure 2.8 shows the fabricated MgF₂ microresonators that have diameters of 3.95 mm (left) and 4.17 mm (right)¹. The fabrication processes follow three steps. First, a cylindrical base material of a few mm diameter is cut out from a bulk material (e.g. commercial MgF₂ lenses).

¹ The MgF₂ microresonators used in this thesis were fabricated by M. Fuchida and A. Kubota. The images in Fig. 2.8 are provided by A. Kubota.

The base material is glued to a metal post and mounted on an air spindle. Second, the rotated base material is roughly shaped to the microresonator structure by grinding with a diamond turning. Third, the smooth microresonator surface is created by polishing with diamond particles while decreasing the particle sizes (3, 1, 0.25, and 0.05 μm), which can lead to a ultrahigh-Q.

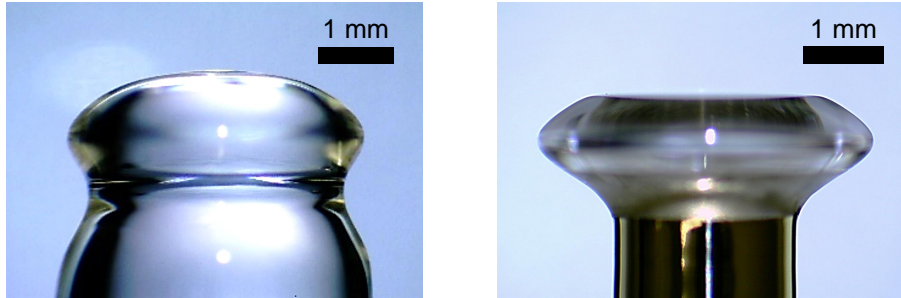


Fig. 2.8: Optical microscope images of polished MgF_2 microresonators.

2.3 Tapered fiber coupling and quality factor measurement

Whispering-gallery modes can be excited through an evanescent field by using an external waveguide such as an optical tapered fiber, a pigtailed fiber, and a prism. In this thesis, a tapered fiber was used to couple light into silica toroid, silica rod, and MgF_2 microresonators. The tapered fiber coupling has the advantages of high coupling efficiency (over 99 %), almost lossless propagation in the tapered fiber, and a lot of flexibility of the coupling position controlled by using a three-axis stage.

2.3.1 Fabrication of tapered fibers

A tapered fiber is fabricated by heating and stretching a commercial single-mode optical fiber. The smallest part of the tapered fiber has a diameter of around 1 μm (a single-mode fiber has the clad diameter of 125 μm), which is the same order as the laser wavelength ($\sim 1.55 \mu\text{m}$) to present an evanescent field outside the fiber.

Figure 2.9(a) shows the fabrication setup where a single-mode fiber is heated with a gas torch on two one-axis automatic positioning stages. The gas torch employs oxygen (O_2) and propane (C_3H_8) gases to burn. The heating position on the fiber is repeatedly scanned while pulling the fiber at the speed of 140 $\mu\text{m/s}$.

Figure 2.9(b) shows the transmission of an input laser while pulling the optical fiber. Typically, more than 95% of transmission in the fabricated tapered fiber can be achieved by optimizing the positions of the fiber, torch, and two stages that hold the fiber. The oscillation amplitude depends on the propagation mode at the thinnest point of the fiber, as described in Fig. 2.9. Hence, pulling the fiber can be stopped when the fiber diameter becomes around 1 μm by monitoring the oscillation amplitude. While pulling the fiber, there are three propagation modes. First, the propagation mode is supported by the total internal reflection between the core and clad of an optical fiber, which is the general scheme to confine light in a commercial single-mode fiber.

Second, heating and stretching crush the core that changes to the mode confined between the clad and air. In this condition, the propagation mode profiles (in a multi-mode) continuously change during pulling the fiber, that causes the transmission oscillation. Finally, since the number of propagation modes becomes one (in a single-mode), the transmission oscillation is suppressed. The diameter can be calculated with the V number (V_{num}) because the propagation mode is supported in a step-index fiber structure (between the core and air). The V number is expressed as

$$V_{\text{num}} = \frac{\pi \phi_{\text{fiber}} \sqrt{n_1^2 - n_2^2}}{\lambda}, \quad (2.20)$$

where ϕ_{fiber} is the diameter of the tapered fiber, λ is the laser wavelength, and n_1 and n_2 are the refractive indices inside and outside the waveguide, respectively. In a step-index fiber, the single-mode condition is obtained when the V number is 2.405. Therefore, the transmission oscillation is suppressed when the diameter of tapered fiber becomes smaller than $\phi_{\text{fiber}} = 1.15 \mu\text{m}$, which is calculated with $n_1 = 1.44$, $n_2 = 1$, and $\lambda = 1.55 \mu\text{m}$.

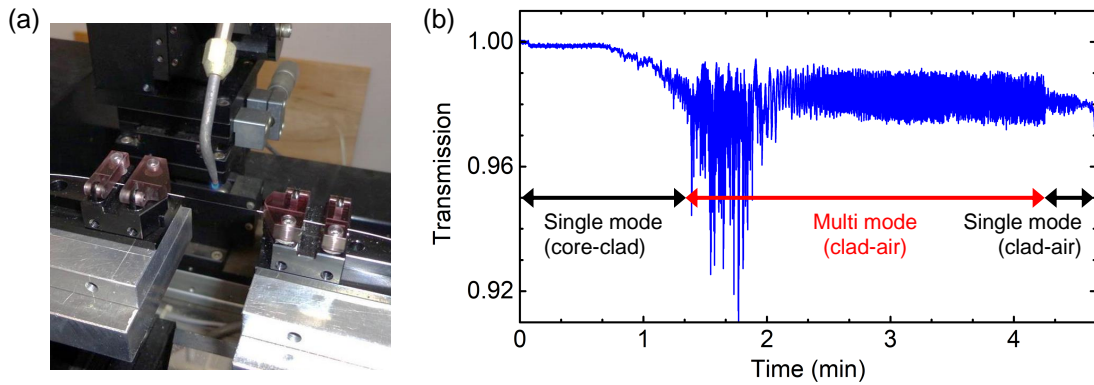


Fig. 2.9: (a) Tapered fiber pulling setup. (b) Transmission during heating and pulling the optical fiber. The amplitude oscillation indicates change of the propagation mode, which includes a single- and a multi-mode. When decreasing the oscillation, the pulled optical fiber has a diameter of around $1 \mu\text{m}$, which is compatible with coupling light to a microresonator.

2.3.2 Quality factor measurement with a tapered fiber

The Q factor is an important parameter to evaluate whether the microresonator could build up intracavity optical power and cause optical nonlinear effects. The Q factor is determined by using the cavity decay rate following Eq. (2.9), which can be evaluated by measuring the linewidth of a resonance mode in the frequency (wavelength) domain and the photon lifetime in the time domain. Figure 2.10(a) shows the tapered fiber coupling setup to measure Q factors. A toroid chip is placed on a three-axis automatic positioning stage that can control the relative position between the microresonator and fiber. The coupling position is monitored by using microscopes from the top and side, whose views are shown in Figs. 2.10(b) and (c). Figure 2.11

shows experimental setups used for Q factor measurement in (a-c) the frequency and (d,e) the time domains. Figures 2.12, 2.13, and 2.14 show measurement results with a silica toroid, a silica rod, and a MgF₂ microresonators, respectively. Fabricated microresonators in this thesis have Q factors of typically 1-10 million (silica toroid), 10-100 million (silica rod), and 100-1000 million (MgF₂).

Frequency domain measurement

As explained in §2.1.2, the transmission in a resonance mode has a Lorentzian shape as a function of the detuning between the resonance and laser frequencies. Therefore, the linewidth of a resonance mode can be evaluated by monitoring the transmission while scanning the laser frequency. Here the frequency (wavelength) axis needs to be calibrated with some frequency (wavelength) marker, that are created by using the built-in function of a commercial laser (Santec TSL-510 and TSL-710), a fiber Mach-Zehnder interferometer (MZI), and a phase modulator. For example, Figs. 2.12(a) and 2.13(a) show measured resonance modes with 50 MHz modulated sidebands that can calibrate from a time axis in an oscilloscope to a frequency axis. As written in §2.1.1, a Q factor is determined as $Q = \omega_0/\kappa (= \lambda_0/\Delta\lambda)$, where λ_0 is the resonance wavelength and $\Delta\lambda$ is the linewidth in the wavelength domain. The frequency calibration in a broad wavelength range, which is created with a fiber MZI, can also be used to measure cavity dispersions. The detail is provided in §2.4.2.

Time domain measurement

Q factors can be evaluated in the time domain by monitoring the output power after stopping the laser input to the resonance mode. The output power decreases exponentially and its decay rate corresponds to the cavity decay rate. This scheme is compatible with ultrahigh-Q microresonators ($Q \geq 10^8$) because of their long photon lifetime (corresponding to the small cavity decay rate). In this thesis, I used two methods in the time domain measurement, which are shown in Figs. 2.11 (d) and (e). In Fig. 2.11 (d), the laser frequency is scanned over the resonance mode. The scan speed (v_{scan} in units of rad·Hz/s) needs to satisfy with $\tau_{\text{cav}} \gg \kappa/v_{\text{scan}}$. After going across the resonance, the output of confined light from the microresonator interferes with the input laser that generate an interferometer signal. In Fig. 2.11 (e), the coupled laser power is modulated with an intensity modulator, where a squared signal is applied. The cavity decay rate can be obtained by fitting with an exponential function to the signal amplitude.

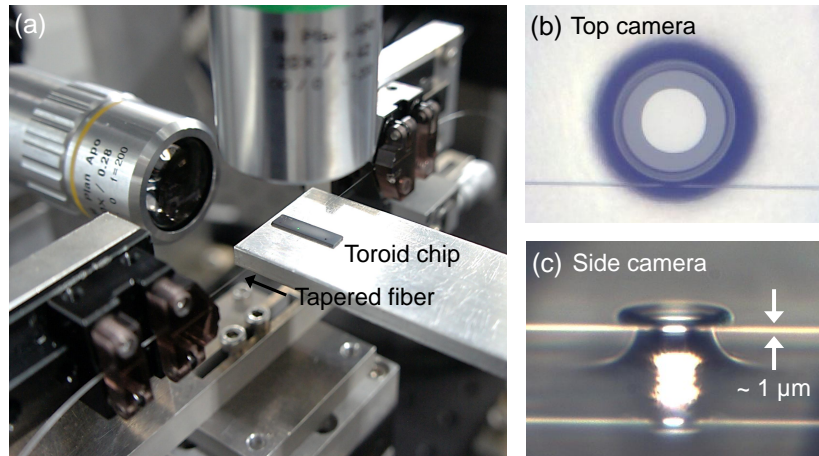


Fig. 2.10: (a) Tapered fiber coupling setup. The toroid chip is placed on a three-axis automatic positioning stage. The toroid microresonator is placed at the blue-emitted point on the chip in the picture (through THG). (b)(c) The microscope views from the top and the side.

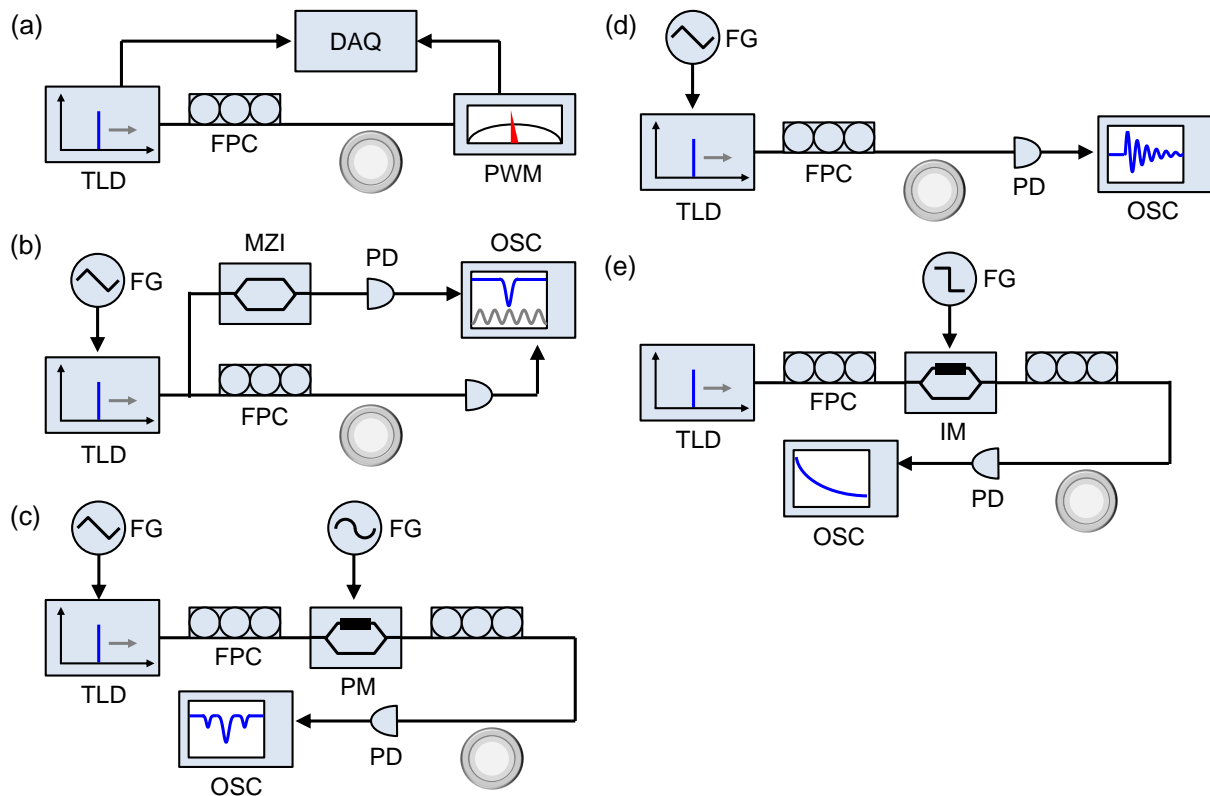


Fig. 2.11: Experimental setups for Q factor measurement in (a-c) the frequency and (d,e) the time domains. TLD: tunable laser diode, FPC: fiber polarization controller, PWM: power meter, DAQ: data acquisition, FG: electrical function generator, MZI: fiber Mach-Zehnder interferometer, PD: photodetector, OSC: oscilloscope, SG: electrical signal generator, PM: phase modulator, IM: intensity modulator, PPG: pulse pattern generator.

2.3. Tapered fiber coupling and quality factor measurement

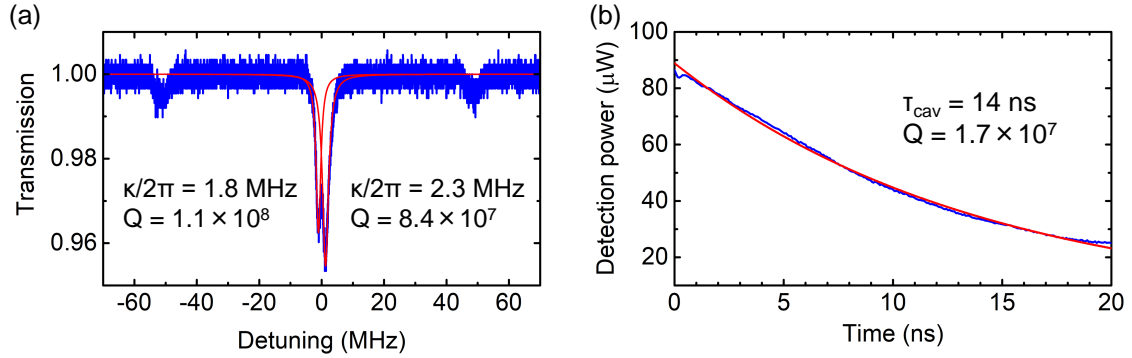


Fig. 2.12: Q factor measurement of silica toroid microresonators in (a) the frequency and (b) the time domains. (a) The phase modulated laser with 50 MHz bandwidth is scanned over the resonance mode (blue). Around the center dip, the two small dips can be observed that can be used to calibrate the frequency axis. Red lines represent Lorentzian functions, whose linewidths correspond to the cavity decay rates $\kappa/2\pi$ (here: 1.8 and 2.3 MHz). The splitting is caused by the mode coupling between clockwise and counter-clockwise propagation modes. (b) Optical power, which decreases exponentially, is monitored after turning the laser input off.

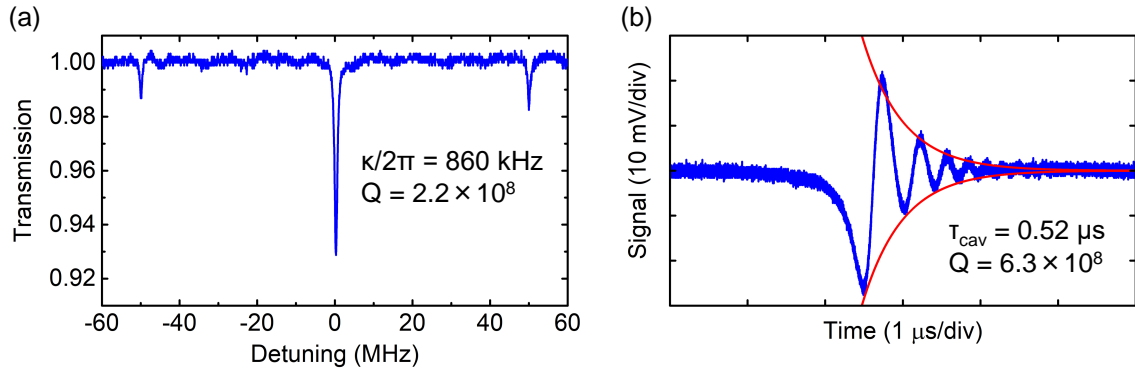


Fig. 2.13: Q factor measurement of silica rod microresonators in (a) the frequency and (b) the time domains. (a) The phase modulated laser with 50 MHz bandwidth is scanned over the resonance mode. (b) The input laser is scanned over the resonance at the scan speed (v_{scan} in units of $\text{rad}\cdot\text{Hz}/\text{s}$) that satisfies with $\tau_{\text{cav}} \gg \kappa/v_{\text{scan}}$. The interference signal can be observed while light is output from a microresonator.

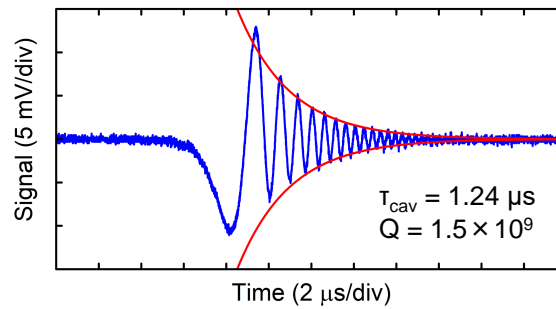


Fig. 2.14: Q factor measurement of an MgF_2 microresonator in the time domain.

2.3.3 Control of coupling condition between microresonator and fiber

To control the coupling condition between resonance and fiber modes is an important technique to input the laser light efficiently. The basic theory is explained in §2.1.2. In experiments, the coupling condition can be optimized by selecting the optimum diameter of a tapered fiber and controlling the relative position between the microresonator and tapered fiber [117–119]. Figure 2.15 shows measurement results of normalized resonance linewidths and minimum transmissions as a function of (a) the gap distance between the fiber and the toroid microresonator, and (b) the coupling parameter. Since the diameter of the tapered fiber at the coupling point is properly selected, the transmission reaches close to zero at the gap distance of $0.9\ \mu\text{m}$. A critical coupling condition, where the transmission is zero and $\kappa/\kappa_1 = 2$, is suitable for most of microresonator experiments because input laser light is efficiently coupled to a resonance mode. When the diameter is not properly selected, the transmission cannot reach zero due to the phase mismatch between resonance and fiber modes.

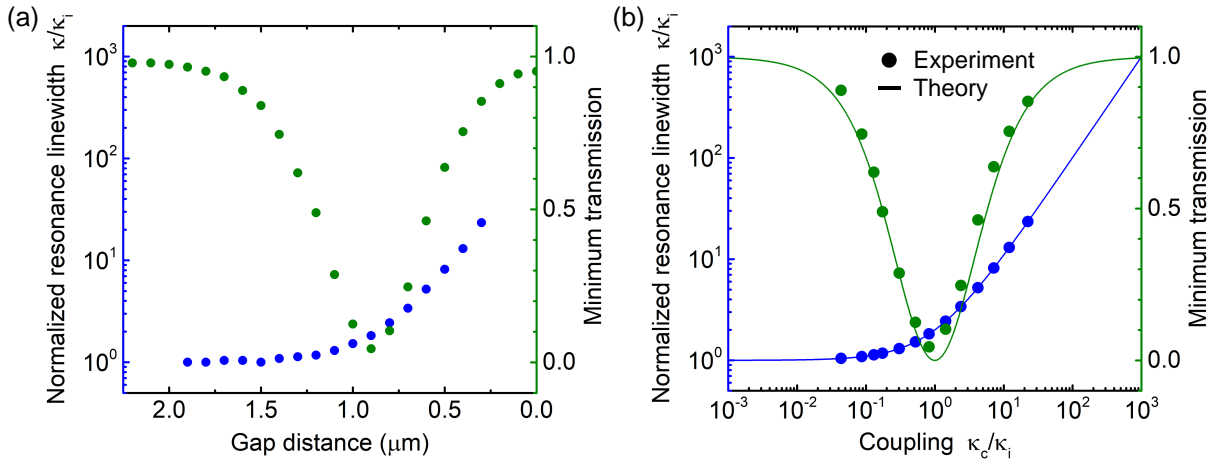


Fig. 2.15: Measurement of normalized resonance linewidths and minimum transmissions as a function of (a) the gap distance between the fiber and toroid microresonator and (b) coupling parameter. (a) The critical coupling, where the transmission is zero and $\kappa/\kappa_1 = 2$, is obtained at the gap distance of $0.9\ \mu\text{m}$. (b) Experimental data is in good agreement with the theory, which is calculated by using Eq. (2.15).

2.3.4 Thermally induced resonance shift

Thermal effects inside a microresonator have impacts on optical coupling, Q factor measurement, output noises, and other properties. For example, in order to evaluate Q factors exactly, resonance frequency shift by thermo-optic and thermal expansion effects should be avoided by reducing the input laser power. This is because the measured resonance shape is distorted from a Lorentzian shape. Figure 2.16 shows resonance modes, which are measured by scanning the pump wavelength from short to long, in a silica toroid microresonator with various input laser powers. With a higher input power, the shape of the resonance mode changes from Lorentzian to triangular. This frequency shift depends on changes of the effective refractive index and the

cavity length. By using Eq. (2.2), the resonance wavelength shift can be expressed as

$$\Delta\lambda_m = \frac{(n + \Delta n)(L + \Delta L)}{m} - \frac{nL}{m} \approx \frac{nL}{m} \left(\frac{\Delta L}{L} + \frac{\Delta n}{n} \right) = \lambda_m \left(\frac{1}{L} \frac{dL}{dT} \Delta T_{TE} + \frac{1}{n} \frac{dn}{dT} \Delta T_{TO} \right). \quad (2.21)$$

Since the first and second terms represent thermo-optic and thermal expansion effects, ΔT_{TE} and ΔT_{TO} are the temperature changes at the parts of resonator structure and resonance mode, respectively. The coefficients are shown in Table 2.1.

The thermal effects can be used to stabilize optical coupling between input laser and resonance mode. This scheme is known as the thermal locking technique [120]. Thermal locking is useful in microresonator experiments because of not requiring external locking systems. However, the locking point is limited to only the blue-detuned side from the resonance frequency in many types of microresonators. This is because many optical materials including silica, MgF_2 , and Si_3N_4 have thermal coefficients (dL/dT and dn/dT) with a positive sign. Thanks to the positive sign, when the laser frequency changes to lower (higher), the coupled power increases (decreases) and that induces increasing (reducing) temperature and shifting the resonance frequency to lower (higher). This passive locking scheme keeps optical coupling at the blue-detuned side. On the other hand, optical coupling at the red-detuned side is unstable. Hence soliton microcomb generation is suffered from thermal instability because a soliton microcomb is only generated with red-detuned pumping (the detail is described in §3.1).

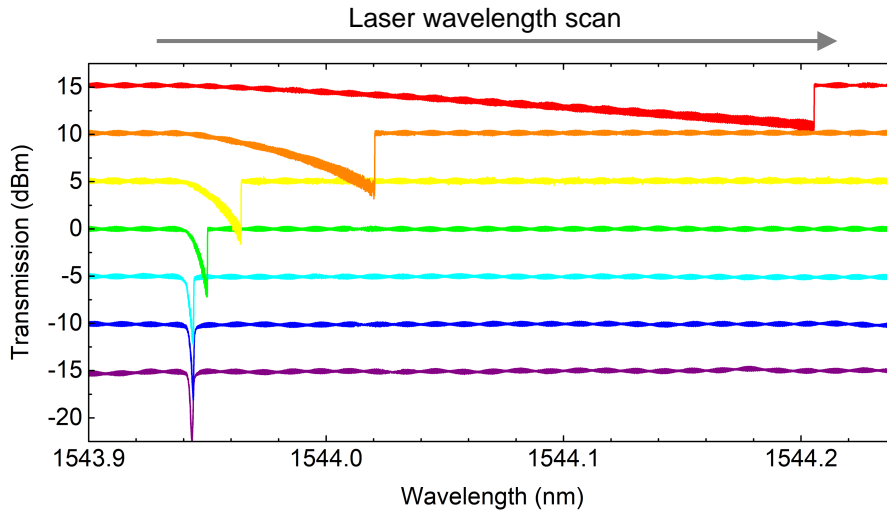


Fig. 2.16: Transmission power from a silica toroid microresonator with various input powers. With a smaller input power, the resonance mode has a Lorentzian shape. On the other hand, with a higher input power, thermo-optic and thermal expansion effects make the shape triangular.

2.4 Cavity dispersion

In microcomb researches, cavity dispersion is a critical parameter that is required to generate FWM with modulation instability and determines microcomb bandwidths. Therefore, in order

to evaluate cavity dispersion of fabricated microresonators, I developed a calculation method with a finite element simulation and a measurement method with a frequency marker.

2.4.1 Finite element simulation for cavity dispersion

Since dispersion means that effective refractive index depends on the frequency (also the mode profile and the polarization), a cavity dispersion can be calculated from resonance frequencies in a transverse mode, as explained in §2.1. The resonance frequencies can be obtained with electromagnetic field calculation, that is performed by modeling the microresonator structure and applying a finite element simulation. In this thesis, I use the software "COMSOL Multiphysics" as a finite element simulation solver that can calculate eigenvalues corresponding to resonance frequencies. When applying a constant refractive index to the material, obtained cavity dispersion considers only geometrical dispersion. However, a cavity dispersion should take account of both geometrical and material dispersions. Hence, I adopt an iterative calculation scheme to obtain exact resonance frequencies (i.e. for cavity dispersion), as shown in Fig. 2.17. The calculation follows three steps. (1) The microresonator structure and the approximate refractive index are set in the finite element simulation solver. (2) The solver calculates the eigenvalue (resonance frequency). Then, a Sellmeier equation calculates a refractive index at the eigenvalue. These processes are repeated in three times. (3) The exact eigenvalue, which takes account of the geometrical and material dispersions, is obtained. Here the finite element simulation solver and the Sellmeier equation consider geometrical and material dispersions, respectively. The Sellmeier equation is expressed as

$$n^2(\lambda) = 1 + \sum_{k=1} \frac{A_k \lambda^2}{\lambda^2 - B_k^2}, \quad (2.22)$$

where λ is the wavelength and A_k and B_k are the coefficients depending on the material, which are shown in Table 2.2. Figure 2.18 shows material dispersions, which are expressed with β_2 and D , in some optical materials as a function of wavelength. The dispersion parameters are as follows:

$$D(\lambda) = -\frac{2\pi c}{\lambda^2} \beta_2(\lambda) = -\frac{\lambda}{c} \frac{d^2 n}{d\lambda^2}. \quad (2.23)$$

Figure 2.19 shows calculated cavity FSRs (d_1) and dispersion values (d_2 and d_3) in a silica disk microresonator, whose parameters are referred to the previous research [121], to check whether the developed method could calculate exact values. The calculation results are in good agreement with those shown in the reference.

Figure 2.20 shows examples of the calculated cavity dispersions at 1550 nm in silica toroid and rod microresonators as a function of the FSR. The FSRs and cavity dispersions depend on the diameter, curvature radius (also referred as minor radius) in the cross section of the resonant part, spatially transverse mode, and TE and TM polarizations. In addition, the finite element simulation solver can calculate an effective mode area A_{eff} , which is explained in §2.1. The calculated effective mode areas in silica toroid and rod microresonators are shown in Fig. 2.21.

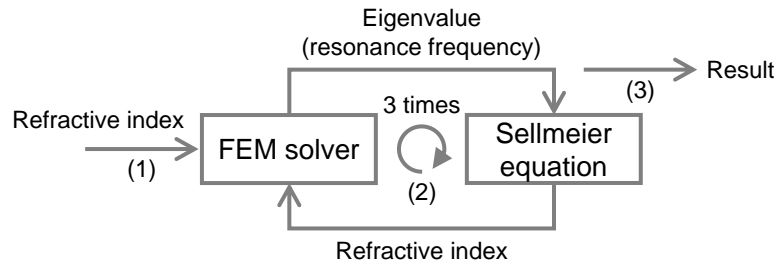


Fig. 2.17: Iterative calculation scheme for cavity dispersion that takes account of material and geometrical dispersions. FEM: finite element method.

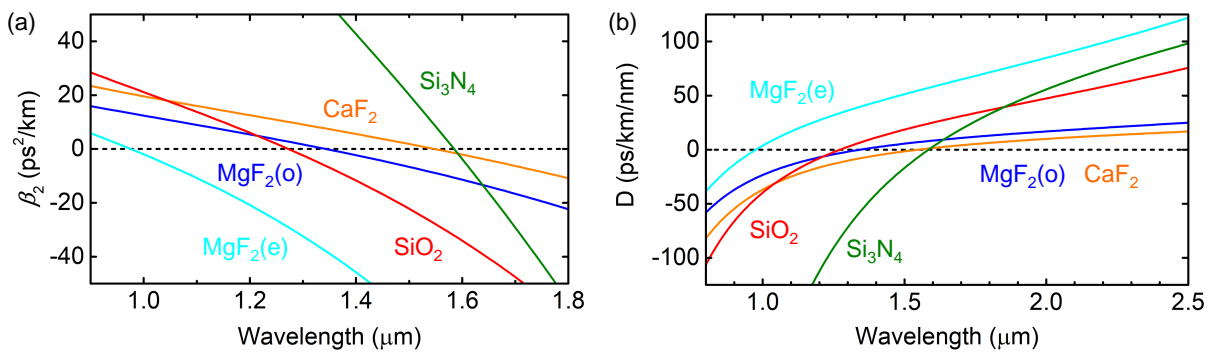


Fig. 2.18: Material dispersion calculated with a Sellmeier equation.

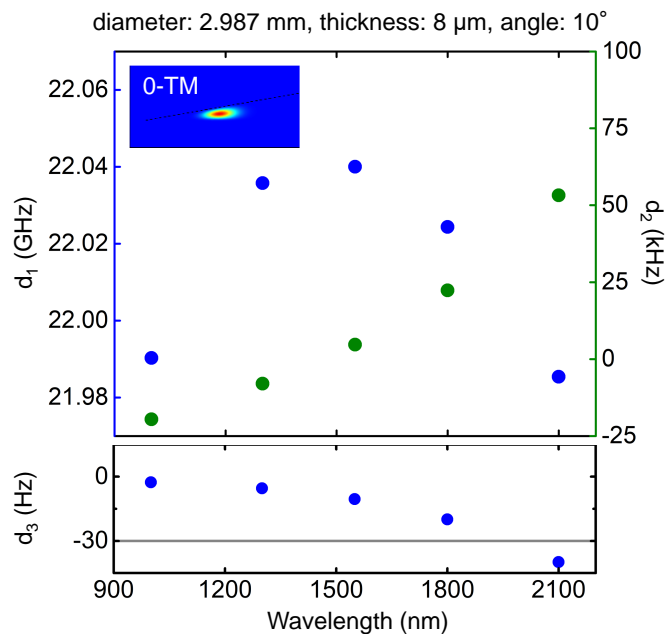


Fig. 2.19: Calculated FSR (d_1) and dispersion values (d_2 and d_3) in a silica disk microresonator that has a diameter of 2.987 mm, a disk thickness of 8 μm , and a wedge angle of 10° . These calculated values are in good agreement with those shown in Ref. [121].

Table. 2.2: Coefficients of Sellmeier equations [113, 122].

	A_1	A_2	A_3	B_1 [μm]	B_2 [μm]	B_3 [μm]
SiO ₂	0.6961663	0.4079426	0.8974794	0.0684043	0.1162414	9.896161
MgF ₂ (o)	0.48755108	0.39875031	2.3120353	0.04338408	0.09461442	23.793604
MgF ₂ (e)	0.41344023	0.50497499	2.4904862	0.03684262	0.09076162	12.771995
CaF ₂	0.5675888	0.4710914	3.8484723	0.050263605	0.1003909	34.649040
Si ₃ N ₄	3.0249	40314		0.1353406	1239.842	

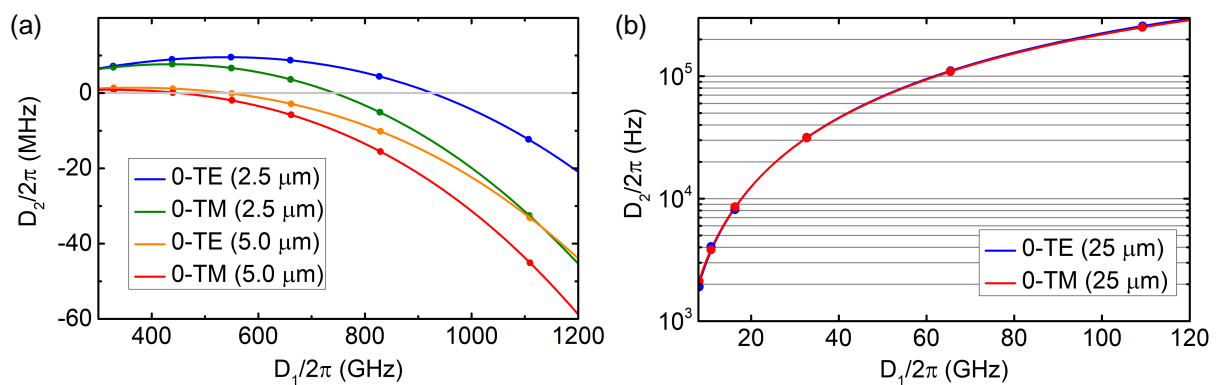


Fig. 2.20: Calculated cavity dispersions in (a) silica toroid and (b) silica rod microresonators as a function of the cavity FSR. The values in parentheses are the curvature radius (minor radius) of the cross section of the resonant part.

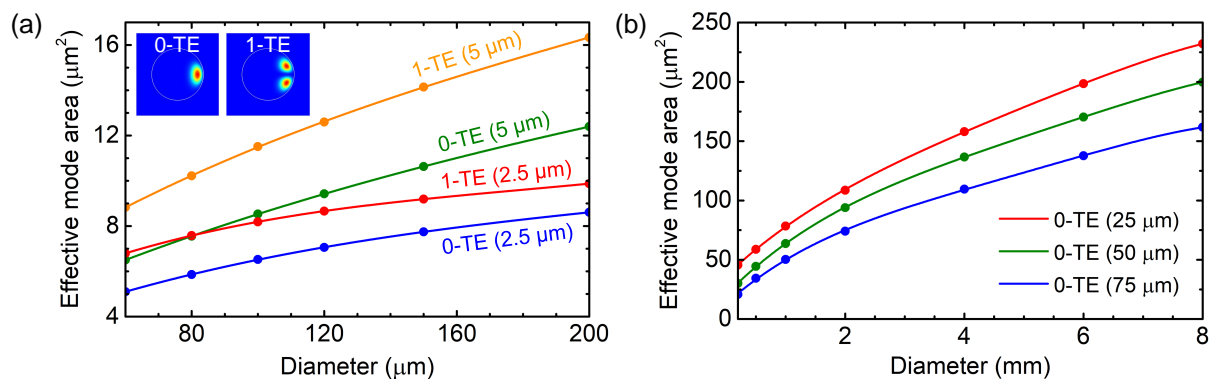


Fig. 2.21: Calculated effective mode areas in (a) silica toroid and (b) silica rod microresonators. The values in parentheses are the curvature radius (minor radius) of the cross section of the resonant part. The insets in (a) represent intensity profiles of fundamental (0-) and higher order (1-) TE modes. In most cases, the mode areas in TE and TM modes are close values.

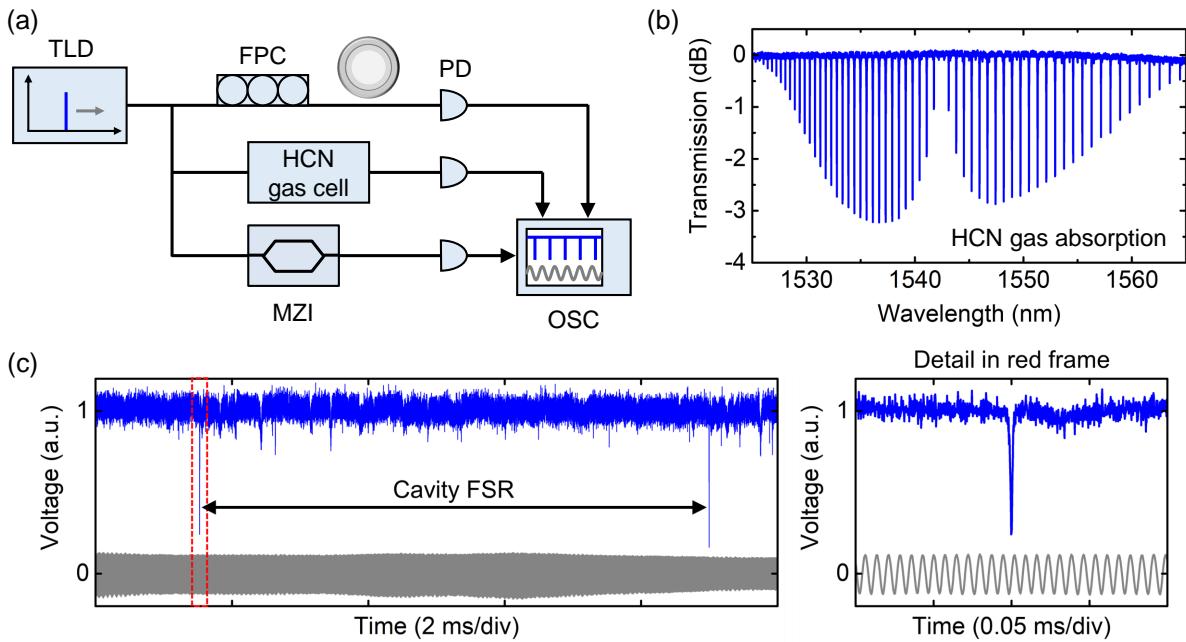


Fig. 2.22: (a) Cavity dispersion measurement setup. A fiber MZI creates a frequency marker that is sinusoidal interferometer signals with a FSR of around 19.7 MHz. Absorption lines of HCN gases determine the absolute wavelength. TLD: tunable laser diode, FPC: fiber polarization controller, PD: photodetector, MZI: fiber Mach-Zehnder interferometer, OSC: oscilloscope. (b) Measured absorption spectrum of the HCN gas. The branch at 1549.73051 nm determines the absolute frequency in the measured resonance spectrum. (c) A part of measured resonance spectrum of a silica rod microresonator (blue) and the MZI signal (gray).

2.4.2 Cavity dispersion measurement

The measurement of cavity dispersion is an important technique in microcomb research to evaluate cavity FSRs, second and higher order dispersions, and also mode coupling between different transverse modes. Since the evaluation of cavity dispersion requires the measurement of resonance frequencies precisely, frequency markers are needed to calibrate the measurement data. A reliable method is to use an optical frequency comb source whose interference signals with a probe CW laser can make frequency markers through two electrical bandpass filters [123]. Although this method can provide very precise and stable frequency markers, the disadvantages are complex measurement setup and requirement of the frequency comb source. In this thesis, a simpler method consisting of a fiber MZI, whose sinusoidal interferometer signal works as a frequency marker in the frequency domain, is used to measure cavity dispersions [124, 125].

Figure 2.22(a) shows the dispersion measurement setup. A fiber MZI and a hydrogen cyanide (HCN) gas cell determine mode spacings between resonance modes and the absolute frequency, respectively. The oscilloscope acquires three pieces of data: resonance spectrum, MZI signal, and HCN gas absorption spectrum.

Figure 2.22(c) shows a part of the measured resonance spectrum of a silica rod microresonator (blue) and the MZI signal (gray). The cavity FSRs are measured by counting periods of the

MZI signal. A fiber MZI is easy to fabricate by connecting two 50:50 optical couplers and two single-mode optical fibers that have different lengths. The length difference in the two pathways (ΔL_{fiber}) determines the period of a sinusoidal interferometer signal in the frequency axis (Δf_{MZI}), which follows

$$\Delta f_{\text{MZI}}(\lambda) = \frac{c}{n(\lambda)\Delta L_{\text{fiber}}} . \quad (2.24)$$

Since I use a length difference of around 10 m, the interferometer signal has periods of around 19.7 MHz. However, as expressed in Eq. (2.24), dispersion of the fiber MZI itself should be compensated to use as a frequency marker. The dispersion value D of a single-mode fiber in ps/(km·nm) units follows:

$$D(\lambda) = \frac{1}{4}S_0\left(\lambda - \frac{\lambda_{\text{zero}}^4}{\lambda^3}\right) \quad (2.25)$$

in the range from 1200 to 1625 nm, where S_0 is the zero dispersion slope ($S_0 \approx 0.09$ ps/(nm²·km)) and λ_{zero} is the zero dispersion wavelength ($\lambda_{\text{zero}} \approx 1310$ nm). Since the single-mode optical fiber (Furukawa Electric, AllWave Fiber) has the effective refractive index of 1.468 at 1550 nm, frequency dependent effective refractive index can be calculated as shown in Fig. 2.23(a). By using the calculated effective refractive index of the optical fibers, frequency dependent FSRs of the fabricated MZI can be calculated as shown in Fig. 2.23(b). In this calculation, I used the measured FSR of 19.6924 MHz at 193.582 THz. The FSR curve in Fig. 2.23(b) is Taylor-expanded as a function of the relative number of the MZI periods (μ_{MZI}) from the center that is at 193.582 THz:

$$\Delta f_{\text{MZI}}(\mu_{\text{MZI}}) = \Delta f_{\text{MZI},0} + d_1\mu_{\text{MZI}} + \frac{1}{2}d_2\mu_{\text{MZI}}^2 . \quad (2.26)$$

The fabricated MZI has parameters of $\Delta f_{\text{MZI},0} = 19.6929$ MHz, $d_1 = 10.8015$ mHz, and $d_2 = -7.87933$ nHz. The MZI dispersion in Eq. (2.26) and the acquired three pieces of experimental data with an oscilloscope are processed using a developed MATLAB code, which automatically searches resonance modes in the same transverse mode and counts the periods of the MZI signal.

To confirm whether the developed measurement system and MATLAB code could work well, I measured dispersion of a fiber loop cavity, which is shown in Fig. 2.24. $\omega_0/2\pi$ and $D_1/2\pi$ are 193.556 THz and 93.3964 MHz, respectively. A fiber loop cavity is easy to fabricate by connecting the one input to the one output in a commercial 99:1 coupler. The light-blue points in Fig. 2.24(a) represent the dispersion (D_{int}) when not taking account of the compensation of the MZI dispersion. The fiber loop cavity and the fiber MZI have almost the same dispersion because they consist of single-mode fibers. Therefore, the measured dispersion value in light-blue points is close to zero ($D_2/2\pi = 0.006$ Hz) by canceling between dispersions of the fiber loop cavity and the fiber MZI. The blue points represent the dispersion of the fiber loop cavity when taking account of the compensation of the MZI dispersion. Figure 2.24(b) shows the detail of measurement data around the mode number offset of zero, whose variation was below 2 MHz. These results mean that the developed system can measure cavity dispersions. Finally, I measured dispersion in silica toroid and rod microresonators, and they were in good agreement with the finite element simulations. The measurement results are shown in §4.7 and §5.4.

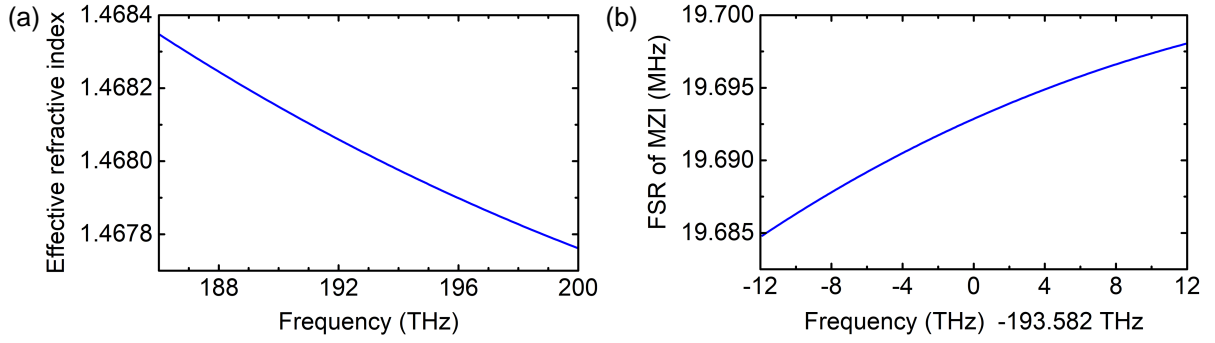


Fig. 2.23: (a) Calculated effective refractive index of a single-mode optical fiber, which has a refractive index of 1.4680 at 1550 nm. The dispersion follows Eq. (2.25). (b) FSR of the fabricated MZI that has 19.6924 MHz at 193.582 THz.

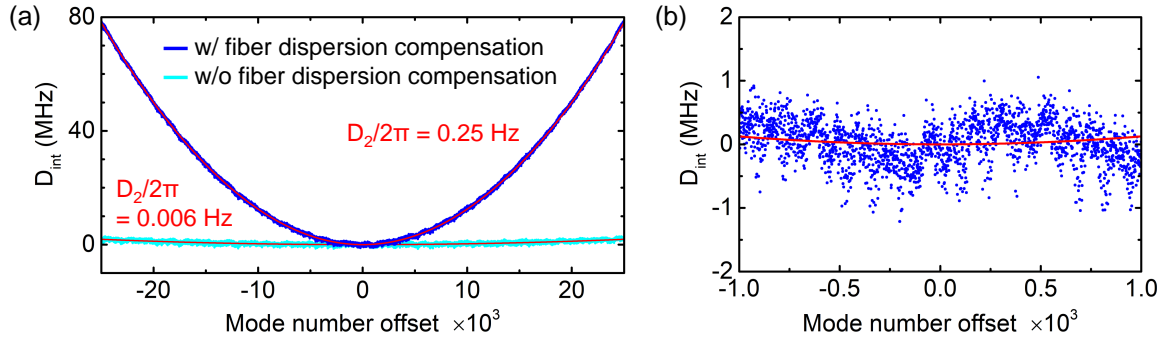


Fig. 2.24: (a) Measured dispersions of a fiber loop cavity with/without compensation of the fiber dispersion, which is expressed in Eq. (2.26). The $\omega_0/2\pi$ and $D_1/2\pi$ are 193.556 THz and 93.3964 MHz, respectively. Since the fiber loop cavity consists of single-mode fibers, the measured dispersion is almost canceled ($D_2/2\pi = 0.006$ Hz) in the case with not considering the fiber dispersion of the fiber MZI. Red lines represent parabolic curve fittings. (b) The detail of measurement data around mode number offset of zero.

2.5 Optical nonlinear processes

2.5.1 Third order nonlinearities in dielectric materials

Optical nonlinear processes mean that polarization \mathcal{P} in dielectric materials scales nonlinearly with externally applied electric fields E , whose relation is represented as

$$\mathcal{P} = \epsilon_0 \{ \chi^{(1)} E + \chi^{(2)} E^2 + \chi^{(3)} E^3 + \dots \}. \quad (2.27)$$

Here ϵ_0 is the vacuum permittivity, $\chi^{(1)}$ is the linear electric susceptibility, and $\chi^{(2)}$ and $\chi^{(3)}$ are the second and third order nonlinear electric susceptibilities, respectively. Although the higher order terms can be neglected when the amplitude of electric fields is small, the higher order terms become dominant with strong electric fields. The second order term works in dielectric materials that are inversion asymmetric at the molecular level ($\chi^{(2)}$ materials) such as LiNbO_3 . In this

thesis, the nonlinear contribution takes account of only the third order term because of using silica and MgF₂ that are symmetric molecules ($\chi^{(3)}$ materials). The third order nonlinearity can play in all dielectric materials. Therefore, the nonlinearity-contributed polarization \mathcal{P}_{NL} can be extracted from Eq. (2.27):

$$\mathcal{P}_{\text{NL}} = \epsilon_0 \chi^{(3)} E^3 . \quad (2.28)$$

Since the third order nonlinear process interacts between four electric field components, the total electric field is described as

$$E = \sum_{j=1}^4 E_j \exp\{i(k_j z - \omega_j t)\} . \quad (2.29)$$

By substituting Eq. (2.29) into Eq. (2.28), the following equation is obtained

$$\mathcal{P}_{\text{NL}} = \sum_{j=1}^4 \mathcal{P}_j \exp\{i(k_j z - \omega_j t)\} . \quad (2.30)$$

\mathcal{P}_j has a large number of terms including three electric field components such as

$$\begin{aligned} \mathcal{P}_4 \propto \{ & |E_4|^2 E_4 + 2(|E_1|^2 + |E_2|^2 + |E_3|^2) E_4 \\ & + 2E_1 E_2 E_3 \exp(i\theta_+) + 2E_1 E_2 E_3^* \exp(i\theta_-) + \dots \} , \end{aligned} \quad (2.31)$$

where θ_+ and θ_- are expressed as

$$\theta_+ = (k_1 + k_2 + k_3 - k_4)z - (\omega_1 + \omega_2 + \omega_3 - \omega_4)t , \quad (2.32)$$

$$\theta_- = (k_1 + k_2 - k_3 - k_4)z - (\omega_1 + \omega_2 - \omega_3 - \omega_4)t . \quad (2.33)$$

In Eq. (2.31), the terms which are proportional to E_4 represent self- and cross-phase modulation (SPM and XPM). The term with θ_+ represents frequency conversion processes of THG and sum frequency generation. Also, the term with θ_- represents frequency conversion processes of FWM.

2.5.2 Optical nonlinear processes in microresonators

Self- and cross-phase modulation

Self- and cross-phase modulation (SPM and XPM) are phenomena to change an effective refractive index in dielectric materials, whose shift depends on the propagating light intensity [126]. SPM refers to the self-induced phase shift, which is caused by interaction of one optical field. XPM refers to the phase shift induced by another optical field that has the different frequency, direction, polarization, or transverse mode. For example, in Eq. (2.31), $|E_4|^2 E_4$ and $2(|E_1|^2 + |E_2|^2 + |E_3|^2) E_4$ represent SPM and XPM, respectively. Since XPM effects work twice as much as SPM effects, change of the effective refractive index $\Delta n(t)$ is expressed as

$$\Delta n(t) = n_2 I_4(t) + 2n_2 \{I_1(t) + I_2(t) + I_3(t)\} , \quad (2.34)$$

where n_2 is the nonlinear refractive index and I_* is the light intensity ($* \ni 1 - 4$). Assuming the case that a microresonator is pumped with a CW laser, the wavelength shift via SPM is as follows

$$\Delta\lambda_m = \frac{(n + \Delta n)L}{m} - \frac{nL}{m} = \frac{n_2 I_4 L}{m} = \frac{n_2 P_{\text{cav}} L}{mA_{\text{eff}}} = \lambda_m \frac{n_2 P_{\text{cav}}}{nA_{\text{eff}}}, \quad (2.35)$$

where the second term on the right-hand side in Eq. (2.34) is neglected because the term represents XPM effects.

The amount of effective refractive index change via SPM and XPM is typically smaller than that via thermal effects, which is expressed in Eq. (2.21). Hence the resonance shift shown in Fig. 2.16 is almost caused by thermal effects. On the other hand, the response time of SPM and XPM (nanoseconds order or below) is much faster than that of thermal effects (\sim microseconds order).

Third-harmonic and sum frequency generation

Third-harmonic generation (THG) is an optical nonlinear process to generate one photon from three photons, which satisfies with energy conservation as $\hbar\omega + \hbar\omega + \hbar\omega = 3\hbar\omega$ [127, 128]. Usually, THG in $\chi^{(3)}$ materials has lower conversion efficiency than SHG in $\chi^{(2)}$ materials. Sum frequency generation is also an optical nonlinear process to generate one photon from three photons, which satisfies with energy conservation as $\hbar\omega_1 + \hbar\omega_2 + \hbar\omega_{3(2)} = \hbar\omega_4$. These processes require the phase matching condition as $k_1 + k_2 + k_3 = k_4$ expressed in Eq. (2.32). Figure 2.25 shows measured THG signal with a spectrometer when pumping to a silica toroid microresonator. The THG wavelength of 513.6 nm is one third of the pump wavelength of 1540.8 nm. The inset in Fig. 2.25 is the captured image with a side camera, which clearly shows green light emission. THG is prone to creation simultaneously with microcombs.

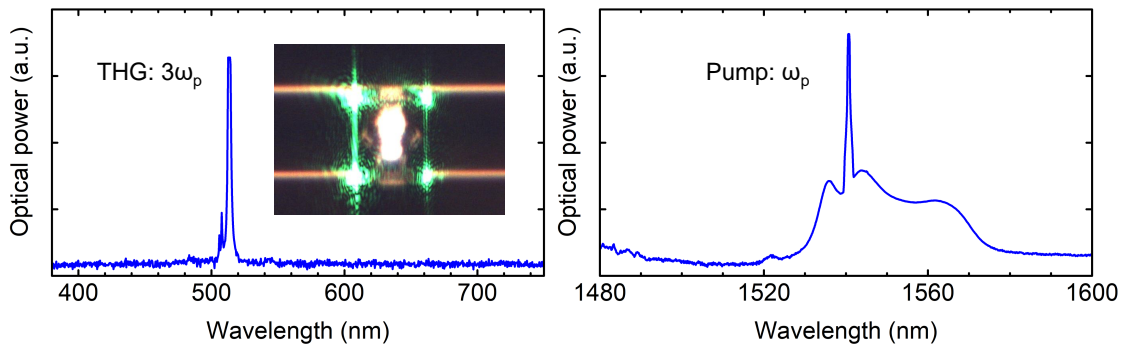


Fig. 2.25: Measured pump signal with an optical spectrum analyzer and THG signal with a spectrometer when pumping to a silica toroid microresonator. The inset shows the captured image with a side camera.

Four-wave mixing

Four-wave mixing (FWM) is an optical nonlinear process to generate new two photons from two photons, which satisfies with energy conservation as $\hbar\omega_1 + \hbar\omega_{2(1)} = \hbar\omega_3 + \hbar\omega_4$ [129, 130]. When

the annihilation photons are in different (same) frequencies, the conversion process is called non-degenerate (degenerate) FWM. These processes require the phase matching condition as $k_1 + k_{2(1)} = k_3 + k_4$ shown in Eq. (2.33). Degenerate FWM can be generated in anomalous dispersion regime with modulation instability. The threshold input power to a coupling waveguide with zero detuning follows:

$$P_{\text{in}}^{\text{FWM}} \approx \frac{\kappa^2 n^2 A_{\text{eff}} L}{8c\omega_0 n_2 \eta}. \quad (2.36)$$

Basically, a microcomb starts to generate by triggering via degenerate FWM by a CW pump laser. A detailed explanation of FWM processes inside a microresonator is provided in Chapter 3. Figure 2.26 shows measured FWM signal when pumping to a silica toroid microresonator. The degenerate FWM generated equally spaced sidebands from the pump laser.

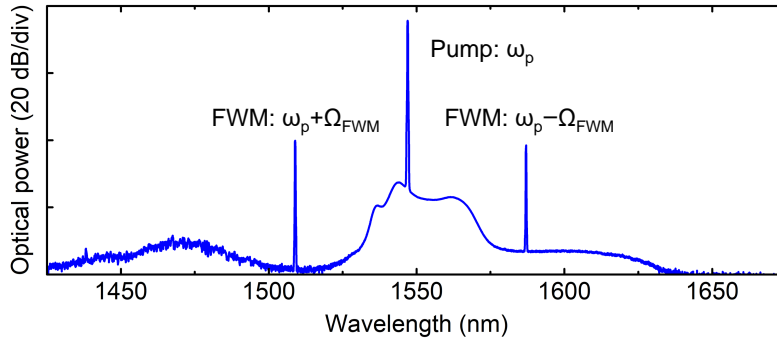


Fig. 2.26: Measurement of sidebands via degenerate FWM when pumping to a silica toroid microresonator. The sidebands have equal spacings from the pump laser in the frequency domain.

Stimulated Raman scattering

Stimulated Raman scattering (SRS) is an optical nonlinear process that generates red-shifted photons from pump photons via interaction between light and molecular vibrations. The amount of frequency shift (Ω_{SRS}) is determined by the host material property (e.g. $\Omega_{\text{SRS}} \sim 14$ THz in silica). The threshold input power to a coupling waveguide with zero detuning is expressed as

$$P_{\text{in}}^{\text{SRS}} \approx \frac{\kappa^2 n^2 A_{\text{eff}} L}{4c^2 \eta g_{\text{R(max)}}}, \quad (2.37)$$

where $g_{\text{R(max)}}$ is the maximum Raman gain in units of m/W (6.2×10^{-14} m/W in silica at 1550 nm). Thanks to the high-Q factor and small mode volume, microresonator-based Raman lasers with low threshold power have been demonstrated [85, 93]. Since Raman gain typically has a broadband spectrum, the influence of SRS is difficult to avoid in most of microcomb researches except for cases using very small microresonators and the material that has a narrow gain spectrum.

With a silica microresonator in anomalous dispersion, the competition between SRS and FWM thresholds in Eqs. (2.36) and (2.37) is given as $P_{\text{in}}^{\text{SRS}}/P_{\text{in}}^{\text{FWM}} \approx (2\omega_0 n_2)/(c g_{\text{R(max)}}) \approx 2.9$, which implies that the FWM occurs before generating SRS. On the other hand, in normal dispersion, SRS becomes dominant because FWM generation is suppressed due to the lack of modulation instability. Figure 2.27 shows the first and second order SRS light in a silica toroid microresonator, which are separated from the pump laser at around 14 and 28 THz, respectively. In this case, multi-mode SRS in a transverse mode occurs due to the broadband spectrum of Raman gain in silica.

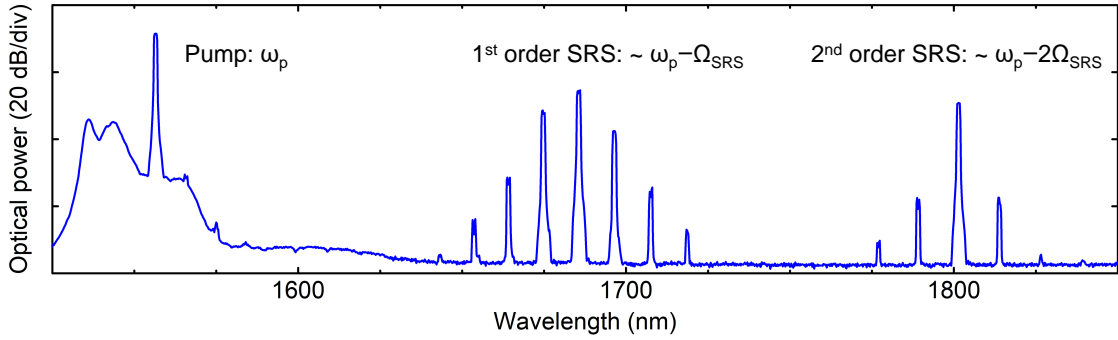


Fig. 2.27: Measurement of SRS signal which is generated by pumping to a silica toroid microresonator. Since silica has a Raman gain peak at around Ω_{SRS} of 14 THz, the first and second order SRS are separated from the pump in around 14 and 28 THz, respectively.

Stimulated Brillouin scattering

Stimulated Brillouin scattering (SBS) is an optical nonlinear process that can generate red-shifted photons, which propagate in the backward direction, from pump photons via the interaction between light and acoustic waves [126]. The amount of frequency shift (Ω_{SBS}) is determined by the host material property (e.g. $\Omega_{\text{SBS}} \sim 11$ GHz in silica). The threshold input power to a coupling waveguide with zero detuning is expressed as

$$P_{\text{in}}^{\text{SBS}} \approx \frac{\kappa^2 n^2 A_{\text{eff}} L}{4c^2 \eta g_{\text{B}}}, \quad (2.38)$$

where g_{B} is the Brillouin gain in units of m/W ($\sim 6 \times 10^{-11}$ m/W in silica at 1550 nm). Since the Brillouin gain is three order of magnitude larger than the Raman gain, the influence of SBS is typically larger than SRS in silica optical fibers. However, in optical microresonators, covering resonance modes with Brillouin gain is required to generate SBS. Hence, SBS does not disturb microcomb research except for some cases such as using a large size microresonator with a cavity FSR below Ω_{SBS} (e.g diameter of a silica microresonator is larger than 6 mm). This is because the spectral bandwidth of Brillouin gain has below 100 MHz in dielectric materials which is typically narrower than the cavity FSR. On the other hand, optimizing the microresonator structure makes it possible to achieve Brillouin lasers with a low threshold power [18, 131].

2.5.3 Cavity optomechanics

Cavity optomechanics is the phenomenon that involves interaction between light and mechanical motion through radiation pressure [13, 14, 77]. The radiation pressure is caused by momentum transfer in the reflection of photons and is a useful technique in many fields, including biology, atomic physics, and gravity wave detection. In particular, the system with a resonator and laser light can enhance the radiation pressure effects which lead to amplifying or damping the motion of the resonator mirror, whose phenomenon is known as dynamical backaction. However, even though this phenomenon was predicted in around 1970 [132], the experimental observation was challenging due to the weak optomechanical coupling and the small oscillator displacement. In recent years, progresses in fabrication processes of micro- and nanodevices have opened up the way to perform various optomechanical experiments. In particular, observation of radiation pressure amplification and damping in a silica toroid microresonator is impressive in this field [78, 133, 134].

Figure 2.28 shows (a) a simulated mechanical mode and (b) a measured photodetector signal when OMPOs occur. Although a toroid structure has many eigenmodes in mechanical modes, the breezing mode is considered to be excited through the laser input because momentum transfer is easily caused between optical and mechanical modes. As shown in Fig. 2.28(b), the photodetector signal has some peaks at multiples of 49 MHz which is the mechanical oscillation frequency. The harmonic signals result from that the optomechanical system working as a phase modulator (and also an intensity modulator). The measured mechanical frequency agrees with the simulated frequency of 50.7 MHz.

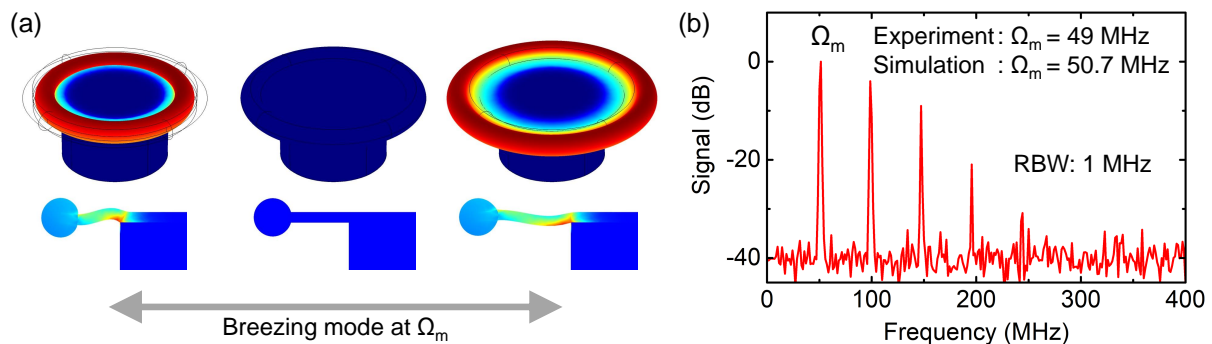


Fig. 2.28: (a) Simulated mechanical mode with finite element simulation. The breezing mode is excited through the laser input to a toroid microresonator because the momentum transfer is easily caused between optical and mechanical modes. The color codes represent displacement (top) and stress (bottom). (b) Measured photodetector signal, which is modulated via optomechanical oscillations at the mechanical frequency Ω_m , through the toroid microresonator. The measured and simulated mechanical frequencies are 49 and 50.7 MHz, respectively. The toroid microresonator has a diameter of $78 \mu\text{m}$, a minor diameter of $7.5 \mu\text{m}$, a disk thickness of $2 \mu\text{m}$, and a pillar diameter of $40 \mu\text{m}$.

Chapter 3

Microresonator frequency combs (microcombs)

This chapter explains the basic theory of microcombs to help in the understanding of Chapter 4, 5, and 6. The theory mainly deals with a Lugiato-Lefever equation, which can calculate microcomb states inside a microresonator and provide an approximate analytical solution for a dissipative Kerr soliton. In experiments, microcomb generation with silica toroid, silica rod, and MgF₂ microresonators was observed. The measured comb spectra and transmission are in good agreement with results of an LLE.

3.1 Theory of microcomb formation dynamics

Microcomb dynamics inside a microresonator can be simulated by two approaches [125, 135]: a spectrotemporal model with a nonlinear coupled mode equation [130, 136] and a spatiotemporal model with a Lugiato-Lefever equation (LLE) [137–139]. A spatiotemporal model is used in Chapter 4 and 6.

3.1.1 Spectrotemporal model: nonlinear coupled mode equation

The first proposed approach is the spectrotemporal model [135], which is developed from a coupled mode equation by increasing the number of calculating modes and adding a Kerr effect term. On the basis of Eq. (2.11), the internal field in a mode number offset from the pump mode (A_μ) can be written as

$$\frac{dA_\mu(t)}{dt} = -\frac{\kappa}{2}A_\mu - i\omega_\mu A_\mu + \delta_{\mu,0}\sqrt{\kappa_c}s_{\text{in}} \exp(-i\omega_p t) + ig \sum_{\mu_1\mu_2\mu_3} A_{\mu_1}A_{\mu_2}A_{\mu_3}^*, \quad (3.1)$$

where $\delta_{\mu,0}$ is the Kronecker delta function ($\delta_{\mu,0} = 1$ at $\mu = 0$), g is the nonlinear coefficient as $g = (\hbar\omega_0^2 n_2 D_1)/(2\pi n A_{\text{eff}})$, ω_μ is the resonance angular frequency at the mode number offset μ , and other parameters are referred in §2.1.2. The third term on the right-hand side only becomes available at the pump mode ($\mu = 0$) because one resonance mode is pumped with a CW laser.

The fourth term on the right-hand side represents Kerr effects including SPM, XPM, and FWM. Then, phase transformation $a_\mu(t) = A_\mu(t) \exp\{i(\omega_p + \mu D_1)t\}$ is applied:

$$\begin{aligned} \frac{da_\mu(t)}{dt} = & -\frac{\kappa}{2}a_\mu + i(\omega_p + \mu D_1 - \omega_\mu)a_\mu + \delta_{\mu,0}\sqrt{\kappa_c}s_{\text{in}} \\ & + ig \sum_{\mu_1\mu_2\mu_3} a_{\mu_1}a_{\mu_2}a_{\mu_3}^* \exp\{-iD_1(\mu_1 + \mu_2 - \mu_3 - \mu)t\}. \end{aligned} \quad (3.2)$$

The phase matching conditions are satisfied when $\mu_3 = \mu_1 + \mu_2 - \mu$ on the Kerr effect term. Also, the resonance angular frequencies can be described as $\omega_\mu = \omega_0 + D_1\mu + D_{\text{int}}(\mu)$ as shown in §2.1.1. By using these relations, Eq. (3.2) can be simplified as

$$\frac{da_\mu(t)}{dt} = -\frac{\kappa}{2}a_\mu + i\Delta\omega_0a_\mu - iD_{\text{int}}a_\mu + \delta_{\mu,0}\sqrt{\kappa_c}s_{\text{in}} + ig \sum_{\mu_1\mu_2} a_{\mu_1}a_{\mu_2}a_{\mu_1+\mu_2-\mu}^*. \quad (3.3)$$

Eq. (3.3) is a nonlinear coupled mode equation to describe microcomb dynamics.

3.1.2 Spatiotemporal model: Lugiato-Lefever equation

The other approach is the spatiotemporal model [125, 135], which calculates Kerr effects in the time domain (in the space domain as azimuthal angle inside a microresonator) by utilizing Fourier transformation. The spatiotemporal model has been employed to simulate microcomb dynamics in many researches owing to the fast calculation time. This is because the spectrotemporal model requires the calculation of a large number of combinations between light fields on the Kerr effect term. On the other hand, in a spatiotemporal model, Kerr effects are calculated with the internal field including light in multiple resonance modes $a(\phi, t)$, which follows:

$$a(\phi, t) = \sum_{\mu} a_{\mu}(t) \exp(i\mu\phi), \quad (3.4)$$

where ϕ is the angular coordinate in the microresonator. Equation (3.4) is differentiated by referring to Eq. (3.3) as

$$\begin{aligned} \frac{\partial a(\phi, t)}{\partial t} &= \sum_{\mu} \frac{\partial a_{\mu}(t) \exp(i\mu\phi)}{\partial t} \\ &= -\frac{\kappa}{2} \sum_{\mu} a_{\mu} \exp(i\mu\phi) + i\Delta\omega_0 \sum_{\mu} a_{\mu} \exp(i\mu\phi) \\ &\quad - i \sum_{\mu} D_{\text{int}} a_{\mu} \exp(i\mu\phi) + ig \sum_{\mu} \sum_{\mu_1\mu_2} a_{\mu_1} a_{\mu_2} a_{\mu_1+\mu_2-\mu}^* \exp(i\mu\phi) + \sqrt{\kappa_c} s_{\text{in}}, \end{aligned} \quad (3.5)$$

which can be simplified as

$$\frac{\partial a(\phi, t)}{\partial t} = -\frac{\kappa}{2}a + i\Delta\omega_0a - i \sum_{k \geq 2} \frac{D_k}{k!} \left(\frac{\partial}{i\partial\phi} \right)^k a + ig|a|^2a + \sqrt{\kappa_c}s_{\text{in}}. \quad (3.6)$$

Equation (3.6) is a Lugiato-Lefever equation (LLE), which can describe microcomb dynamics. Here from Eq. (3.5) to Eq. (3.6), transformation of the dispersion term uses following relations:

$$\left(\frac{\partial}{\partial\phi}\right)^k a = i^k \sum_{\mu} \mu^k a_{\mu}(t) \exp(i\mu\phi), \quad (3.7)$$

$$\sum_{\mu} D_{\text{int}}(\mu) a_{\mu}(t) \exp(i\mu\phi) = \sum_k \left\{ \frac{D_k}{k!} \sum_{\mu} \mu^k a_{\mu}(t) \exp(i\mu\phi) \right\} = \sum_k \frac{D_k}{k!} \left(\frac{\partial}{i\partial\phi}\right)^k a. \quad (3.8)$$

Also, the transformation of the Kerr effect term uses following relation:

$$\begin{aligned} & \sum_{\mu} \sum_{\mu_1 \mu_2} a_{\mu_1} a_{\mu_2} a_{\mu_1 + \mu_2 - \mu}^* \exp(i\mu\phi) \\ &= \sum_{\mu_1} a_{\mu_1} \exp(i\mu_1\phi) \sum_{\mu_2} a_{\mu_2} \exp(i\mu_2\phi) \sum_{\mu_3} a_{\mu_3}^* \exp(-i\mu_3\phi) \\ &= |a|^2 a. \end{aligned} \quad (3.9)$$

An LLE can include Kerr effects, which is shown in Eq. (3.6), and also Raman effects. Although Kerr effects are considered to cause instantaneously, the response of Raman effects is delayed from the carrier light field. Hence the response of Kerr and Raman effects need to be calculated with integral calculus as a function of the angular coordinate, which is related to the (fast) time domain in the microresonator ϕ . The nonlinear response function $h(\tilde{t})$ including Kerr and Raman effects can be expressed as

$$h(\tilde{t}) = (1 - f_R)\delta(\tilde{t}) + f_R h_R(\tilde{t}), \quad (3.10)$$

where \tilde{t} is the fast time frame, f_R is the Raman contribution coefficient ($f_R = 0.18$ in silica), $\delta(\tilde{t})$ is the Kronecker delta function ($\delta(\tilde{t}) = 1$ at $\tilde{t} = 0$), and $h_R(\tilde{t})$ is the Raman response function which is normalized as $\int_0^{\infty} h_R(\tilde{t}) d\tilde{t} = 1$. The Raman response in silica is explained in §5.1. Therefore, an LLE that can take account of Raman effects can be expressed as

$$\frac{\partial a(\phi, t)}{\partial t} = -\frac{\kappa}{2} a + i\Delta\omega_0 a - i \sum_{k \geq 2} \frac{D_k}{k!} \left(\frac{\partial}{i\partial\phi}\right)^k a + i g a \int_0^{2\pi} h\left(\frac{\phi'}{D_1}\right) |a(\phi - \phi')|^2 d\phi' + \sqrt{\kappa_c} s_{\text{in}}. \quad (3.11)$$

3.1.3 Microcomb formation via cascaded four-wave mixing

Microcomb formation and the states

A microcomb is generated in a microresonator via cascaded FWM driven by a CW pump laser through an external waveguide. The commonly used method is to scan the pump frequency over the resonance mode to the lower side. The pump scanning changes the intracavity conditions from the CW state: Turing pattern and chaotic combs with blue-detuned pumping; breather soliton, multi-soliton, and single soliton combs with red-detuned pumping [39]. The understanding

Table 3.1: Characteristics of microcomb states

	Turing pattern	Chaos	(Single) soliton
Relative phases between comb lines	Fixed	Random	Zero
Number of comb lines	Small	Large	Large
Pump detuning from resonance	Blue-side	Blue-side	Red-side

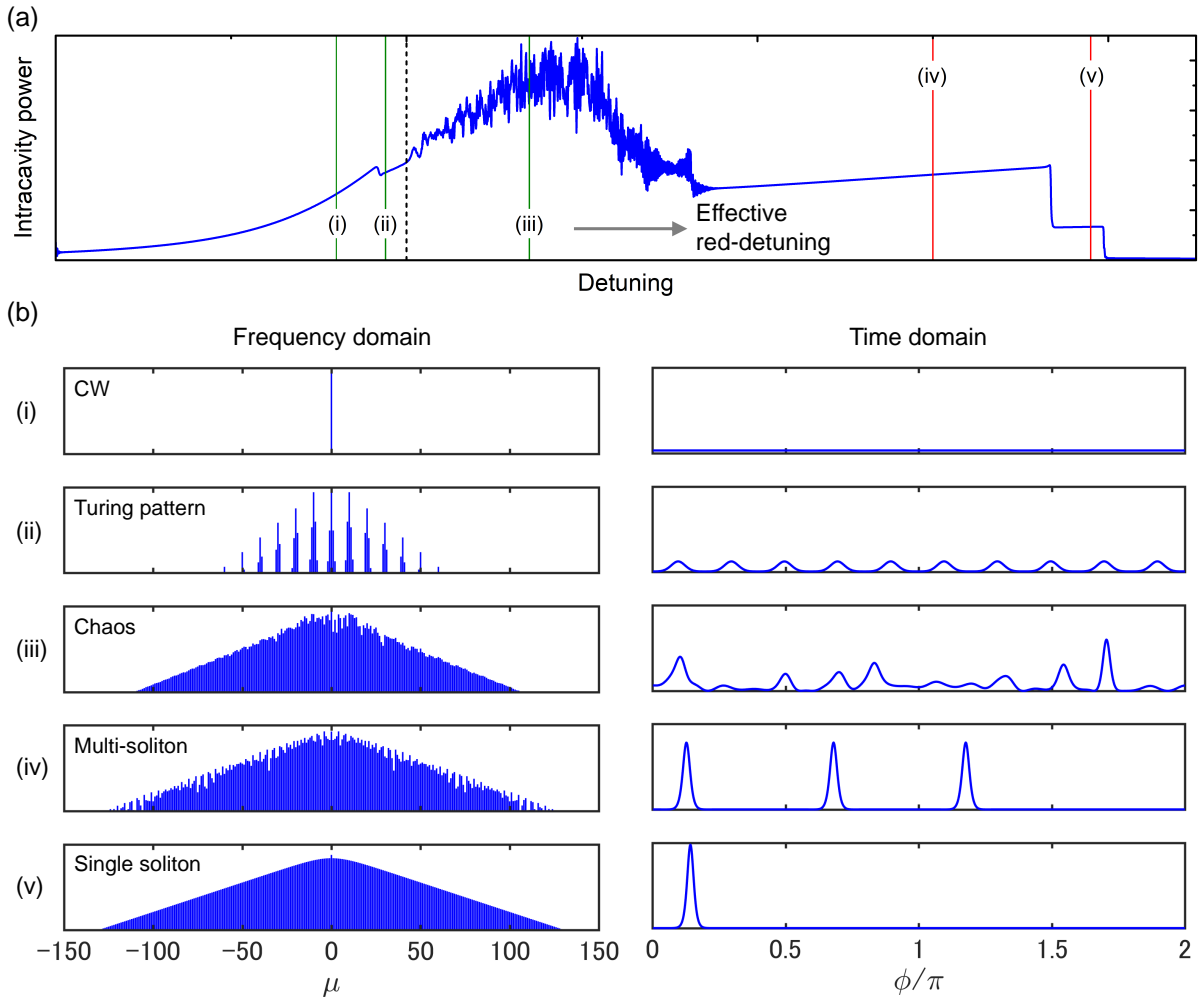


Fig. 3.1: Microcomb formation calculated with an LLE shown in Eq. (3.6). The parameters follow $D_2/\kappa = 0.05$ and $(2s_{\text{in}}/\kappa)\sqrt{2g\kappa_c/\kappa} = 4$. (a) Intracavity power as a function of pump detuning. The microcomb state depends on the pump detuning: (i) CW, (ii) Turing pattern, (iii) chaos, (iv) multi-soliton, and (v) single soliton states. The soliton states are achieved with effective red-detuned pumping. The step-like power transition at (iv) and (v) are called "soliton steps". (b) Microcomb spectra and waveforms in a microresonator at different states.

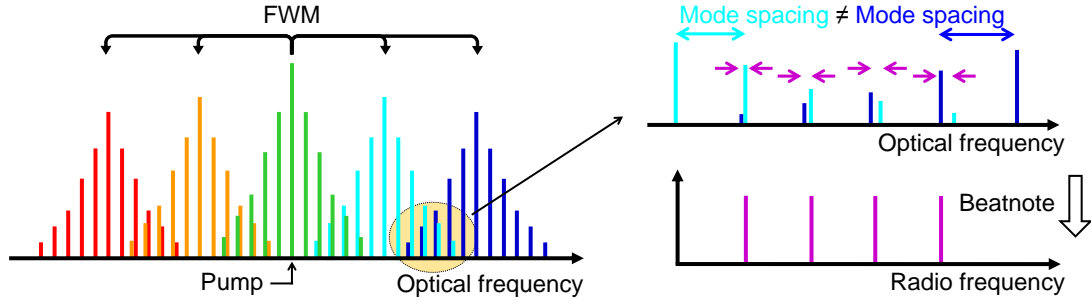


Fig. 3.2: Illustration of a chaotic microcomb spectrum and the amplitude noise. The primary comb lines are generated via degenerate FWM driven by a CW pump laser. Since the each primary comb line generates sub comb lines in different mode spacings, multiple laser lines exist in a single resonance mode and cause amplitude noises of the microcomb. The noises can be evaluated with a photodetector by monitoring beatnote signal of the microcomb.

of the formation and properties in each state is key to follow this thesis's results (particularly in Chapter 4 and 6). Therefore, in this section, the general formation and properties of microcombs are shown using an LLE.

Figure 3.1 shows simulation results of microcomb formation depending on the pump detuning, which are calculated with Eq. (3.6). First, the coupled CW laser builds up intracavity power and causes degenerate FWM that forms a microcomb called a Turing pattern comb or a primary comb. A Turing pattern comb has equal mode spacings between comb lines due to the pure FWM. Second, a chaotic comb (also known as a modulation instability comb) is formed by sub comb lines being generated from each primary comb line independently and overlapping. [140, 141]. Since the each primary comb line generates sub comb lines in different mode spacings, multiple laser lines exist in a single resonance mode and cause amplitude noises of the microcomb, as shown in Fig. 3.2. Third, when the effective pump detuning changes from blue to red, the intracavity field becomes in mode-locked condition where the microcomb propagates as soliton pulses inside the microresonator. As shown in Fig. 3.1(a), soliton states have discrete intracavity powers that depend on the number of soliton pulses. The step-like power transitions are called "soliton steps". The analysis of a stationary-state soliton microcomb is explained in §3.1.4.

First sidebands of microcomb via degenerate four-wave mixing

The first sidebands of a microcomb are generated via degenerate FWM driven by a CW pump laser. Degenerate FWM generates in anomalous dispersion regime with modulation instability that amplifies amplitude noises of the coupled CW laser in the time domain. Also, in the frequency domain, the CW laser is coupled to a resonance mode at the blue-detuned side and generates sidebands at the centers of resonance modes, as illustrated in Fig. 3.3. The mode number offsets μ_{th} , where first sidebands generate, are determined by as follows [142]:

$$-\Delta\omega_0 + \frac{1}{2}D_2\mu_{th}^2 \approx 0, \quad (3.12)$$

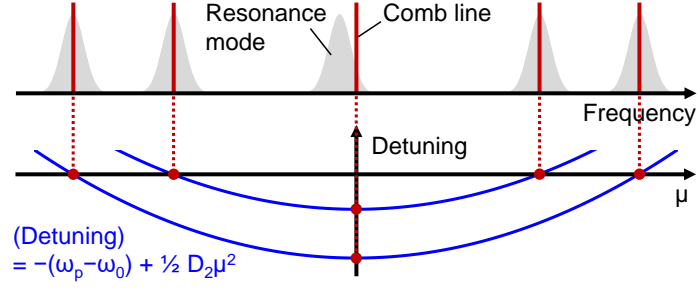


Fig. 3.3: Schematic of first sidebands generated at the center of resonance modes. $(\omega_p - \omega_0) + \frac{1}{2}D_2\mu^2 \approx 0$ is satisfied when reaching the intracavity power to the threshold for degenerate FWM.

when reaching the intracavity power to the threshold for degenerate FWM. To satisfy with Eq. (3.12), the blue-detuned pumping ($\Delta\omega_0 = \omega_p - \omega_0 > 0$) is required in anomalous dispersion regime ($D_2 > 0$). The threshold intracavity power for degenerate FWM $P_{\text{cav}}^{\text{FWM}}$ can be expressed as

$$P_{\text{cav}}^{\text{FWM}} = \frac{\kappa n A_{\text{eff}}}{2\omega_0 n_2} \quad (3.13)$$

by using Eq. (2.36) and the relation between input power P_{in} and intracavity power P_{cav} :

$$P_{\text{cav}} = \frac{\kappa_c}{\frac{1}{4}\kappa^2 + \Delta\omega_0^2} \frac{D_1}{2\pi} P_{\text{in}}. \quad (3.14)$$

Therefore, the pump detuning to generate the first sidebands can be calculated as

$$\Delta\omega_0 = \sqrt{\frac{2c\omega_0 n_2}{n^2 \eta A_{\text{eff}} L} P_{\text{in}} - \frac{1}{4}\kappa^2}. \quad (3.15)$$

The first sideband generation at close to the center of resonance modes is experimentally confirmed in §4.3.

In a case with normal dispersion regime, the lack of modulation instability obstructs the creation of degenerate FWM, which is a trigger to form a microcomb. However, when mode coupling between different transverse modes in a microresonator (or different transverse modes in two microresonators) shifts a resonance frequency that makes effectively anomalous dispersion, first sidebands can oscillate at the shifted resonance mode [143, 144]. As a result of the microcomb formation, microresonators with a normal dispersion can generate a mode-locked pulse that propagates as a dark soliton pulse [145].

3.1.4 Analysis of soliton solution in a microresonator

The analytical approach for soliton microcomb can be performed using an LLE that considers lossless, no input, and the dispersion with only the second order [125, 146]:

$$\frac{\partial a(\phi, t)}{\partial t} = i\Delta\omega_0 a + i\frac{D_2}{2} \frac{\partial^2 a}{\partial \phi^2} + ig|a|^2 a. \quad (3.16)$$

To analyze the stationary-state soliton solution, I assume the ansatz of a single soliton as¹

$$a(\phi) = \mathcal{B} \operatorname{sech}(\phi/\phi_s) \exp(i\varphi_0), \quad (3.17)$$

where \mathcal{B} is the soliton amplitude, ϕ_s is the soliton pulse width in the angular coordinate domain following $\phi_s = \tilde{t}_s/D_1$, \tilde{t}_s is the soliton pulse width in time domain, and φ_0 is the phase of the soliton envelope relative to the pump. By substituting Eq. (3.17) for Eq. (3.16),

$$0 = \left\{ \Delta\omega_0 + \frac{D_2}{2\phi_s^2} \right\} + \operatorname{sech}^2\left(\frac{\phi}{\phi_s}\right) \left\{ g\mathcal{B}^2 - \frac{D_2}{\phi_s^2} \right\} \quad (3.18)$$

is obtained. Hence the stationary soliton condition can be written as

$$D_2 = g\mathcal{B}^2\phi_s^2 > 0, \quad (3.19)$$

$$\Delta\omega_0 = -\frac{D_2}{2\phi_s^2} = -\frac{1}{2}g\mathcal{B}^2 < 0, \quad (3.20)$$

which mean anomalous dispersion and red-detuned pumping are required for soliton microcombs.

3.2 Experimental observation of microcomb generation

Microcomb generation with silica toroid, silica rod, and MgF₂ microresonators was observed. The measured comb spectra and transmission are in good agreement with results of an LLE.

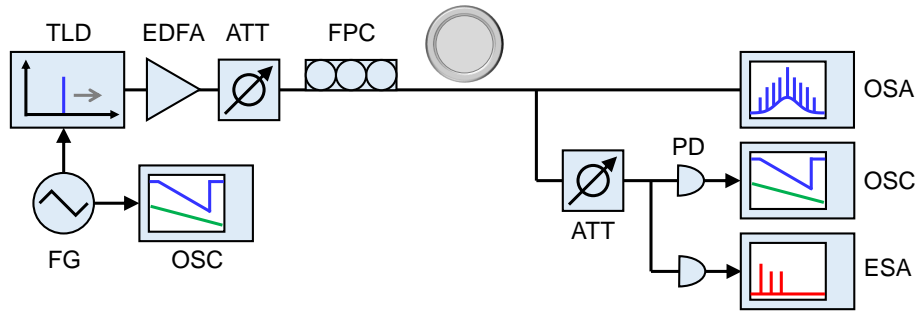


Fig. 3.4: Basic experimental setup for microcomb generation. The pump laser is scanned over the resonance mode from higher to lower frequency to generate a microcomb. Although not shown in this figure, sometimes ASE noise from an EDFA is filtered out by using a bandpass filter. TLD: tunable laser diode, FG: electrical function generator, EDFA: erbium-doped fiber amplifier, ATT: optical variable attenuator, FPC: fiber polarization controller, PD: photodetector, OSA: optical spectrum analyzer, OSC: oscilloscope, ESA: electrical spectrum analyzer.

¹ Hyperbolic function: $\operatorname{sech}x = \frac{2}{e^x + e^{-x}}$, $\frac{d^2}{dx^2}(\operatorname{sech}x) = \operatorname{sech}x(1 - 2\operatorname{sech}^2x)$

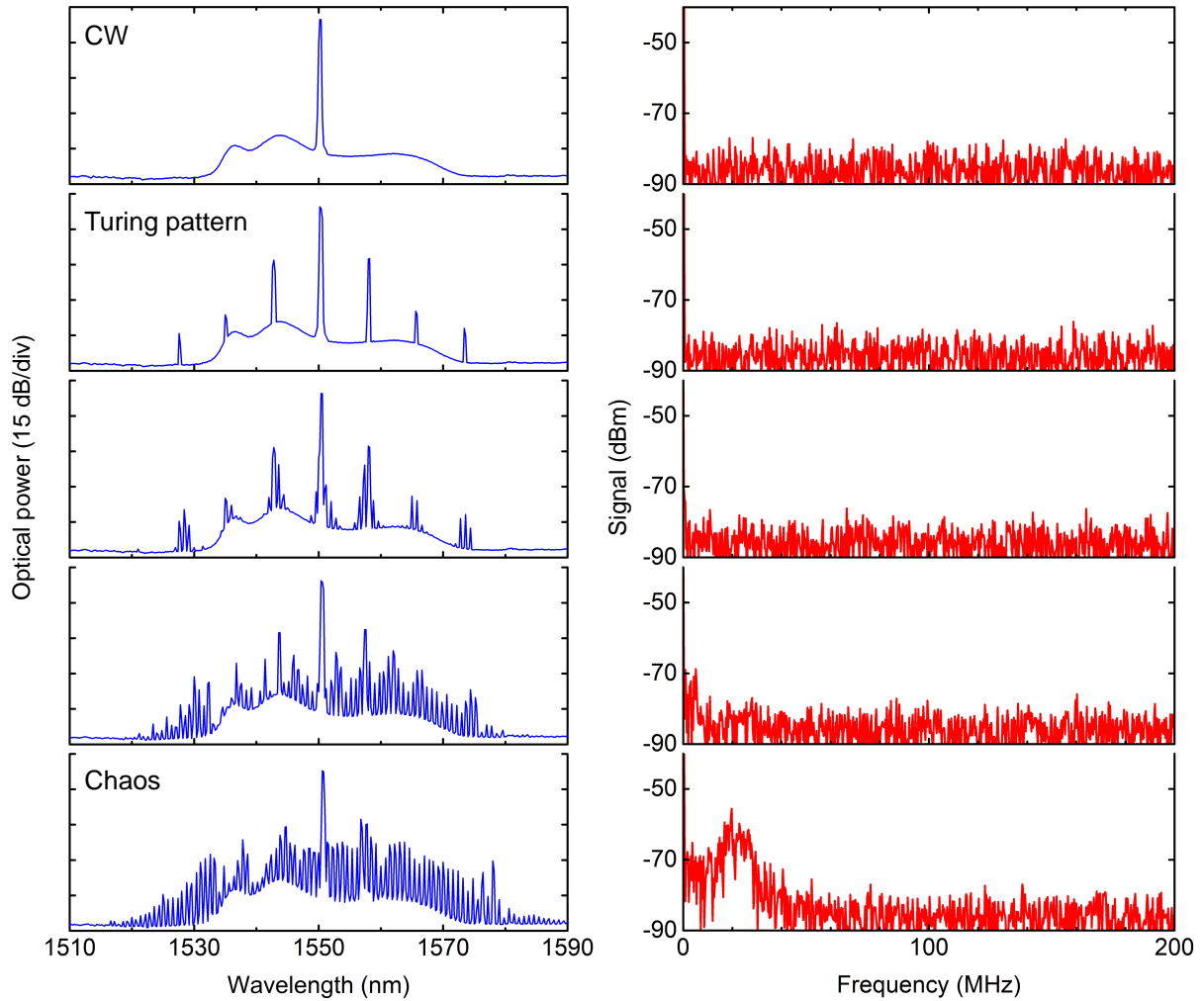


Fig. 3.5: Optical spectra and the photodetector signals while changing the microcomb states in a silica rod microresonator. From the top to bottom, the pump laser is scanned to lower frequency over the resonance mode. First, the coupled CW light builds up inside a microresonator that generates primary comb lines via degenerate FWM. Second, sub comb lines are generated from primary comb lines and overlap each other which causes noise in the photodetector signal.

3.2.1 Microcomb generation and formation in microresonators

The basic experimental setup for microcomb generation is shown in Fig. 3.4. The amplified CW laser, whose frequency is controlled with a function generator, is coupled to a high-Q microresonator through a tapered fiber. The output light is monitored by using an optical spectrum analyzer and photodetectors connected to an oscilloscope and an electrical spectrum analyzer. Although not shown in Fig. 3.4, amplified spontaneous emission (ASE) noises from an EDFA is sometimes filtered out by using a bandpass filter. The pump laser is scanned over the resonance mode from higher to lower frequency to generate a microcomb. This is because the resonance frequency shifts to lower due to Kerr and thermal effects. The scanning keeps the pump-resonance coupling to generate Turing pattern, chaotic, and also soliton microcombs.

Figure 3.5 shows microcomb formation in a silica rod microresonator while scanning the pump frequency from high to low (from the top to bottom). The microcomb formation follows calculation results shown in Fig. 3.1. First, the CW pump laser is converted to a Turing pattern comb when the intracavity power exceeds to the threshold for degenerate FWM. The positions of first sidebands are determined by the dispersion and pump detuning, as explained in §3.1.3. Second, primary comb lines cause degenerate FWM that generates sub comb lines. Finally, the sub comb lines overlap each other that make a noisy photodetector signal as shown at the bottom of Fig. 3.5. This is because multiple comb lines exist in one resonance mode, due to that the primary comb lines individually cause degenerate FWM processes in different mode spacings, as explained in Fig. 3.2. Finally, a soliton microcomb can be formed when the pump frequency reaches to red-detuned side. Although I have not measured the microcomb spectrum and photodetector signal in a soliton state, the transmission with soliton steps have observed, which is introduced in §3.2.2.

To show typical microcomb spectra, I performed the experiment using silica rod and toroid microresonators. Figures 3.6 and 3.7 show experimentally observed microcombs at chaotic states. Typically, the broad bandwidth can be obtained with a microcomb that has large mode spacings.

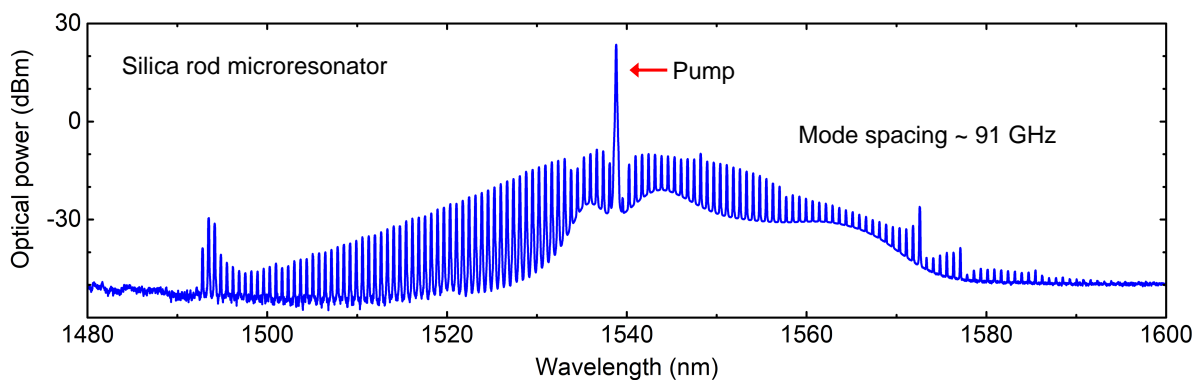


Fig. 3.6: Microcomb generation in a silica rod microresonator which has a cavity FSR of around 91 GHz. The ASE noise was not filtered out. The spikes (e.g. at 1494 nm) are caused by mode coupling between different transverse modes.

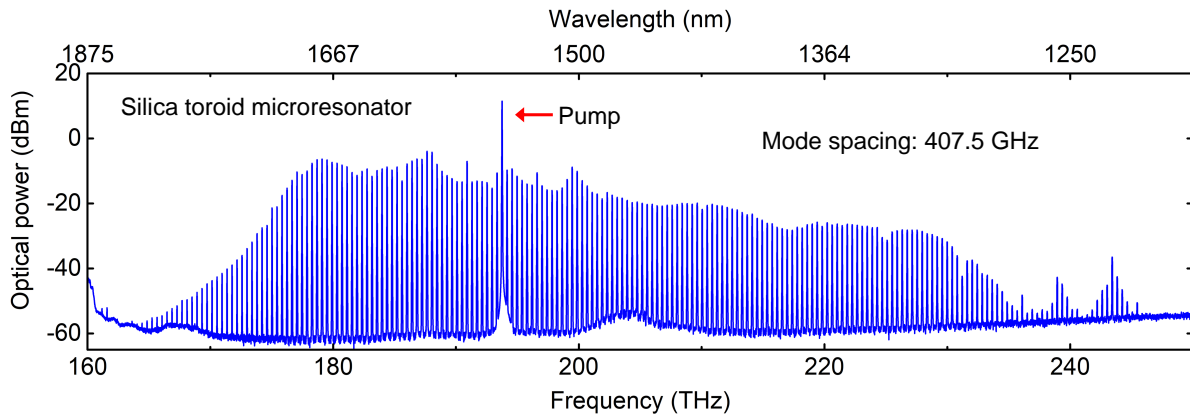


Fig. 3.7: Broadband microcomb generation in a silica toroid microresonator which has a cavity FSR of 407.5 GHz. The 20 dB bandwidth, whose reference is the power of comb line next to the pump, is 414 nm and the pump is 1547 nm. Basically, the bandwidth is limited by the cavity dispersion, which is anomalous dispersion at the pump frequency and zero dispersion at higher frequency side from the pump. The lower frequency side around 180 THz is amplified by the assistance of Raman effects.

3.2.2 Transmission and soliton steps while scanning pump laser

Measured transmission and soliton trapping while scanning a pump laser are in good agreement with an LLE simulation result. Soliton steps, which indicate that a generated microcomb is mode-locked and propagates as soliton pulses, were observed in polished MgF_2 and silica rod microresonators. The amplified CW laser is scanned from a short to a long wavelength by controlling the applied voltage to the laser. Figure 3.8 shows the transmission data in a polished MgF_2 microresonator, which represent (a) a single and (b) multiple soliton steps. The optical power at the steps are determined the soliton power such as the peak power and the number of solitons inside a microresonator.

A chaotic comb is easy to measure due to the stable optical coupling at blue-detuned side from the resonance that is assisted by thermal effects. On the other hand, to keep the generation of a soliton microcomb, the pump wavelength needs to be maintained to couple the resonance mode at red-detuning side. However, as explained in §2.3.4, the red-detuned coupling becomes unstable due to thermally induced resonance shift. Hence, MgF_2 microresonators are compatible with soliton microcomb generation due to the small thermo-optic coefficient [39]. In addition, to overcome the instability, feedback techniques need to be performed and a stable pump laser is required (e.g. fiber lasers have better stability against frequency fluctuation than external cavity diode lasers) especially for high-Q microresonators because of its narrower cavity linewidth.

Another point to observe the soliton steps is that mode coupling with other transverse modes around the pump mode should be avoided by selecting a suitable pump frequency and engineering the cavity FSRs and dispersion values [147]. Figure 3.9 shows spectral envelopes which are distorted by the mode couplings.

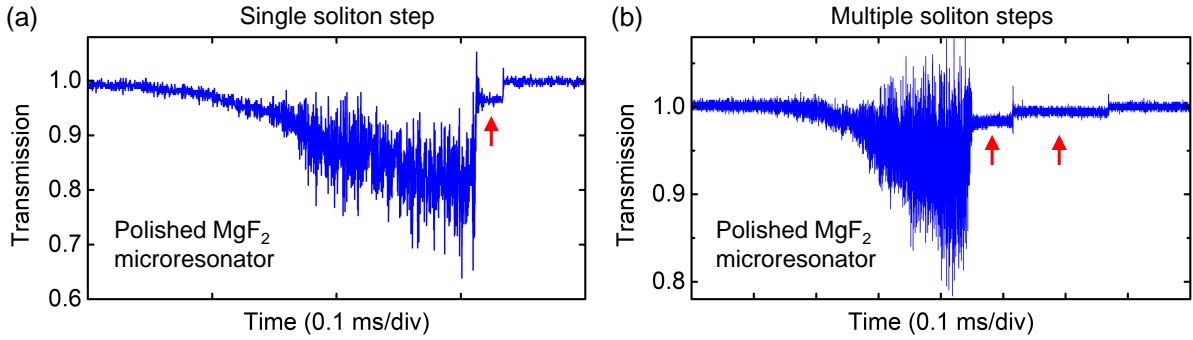


Fig. 3.8: Soliton steps (shown with red arrows) while scanning the pump frequency to lower over the resonance mode in a MgF_2 microresonator, which has a cavity FSR of 17.6 GHz. The soliton steps can be observed with red-detuned pumping as explained in §3.1.4. The multiple soliton steps indicate changing the number of soliton pulses inside a microresonator.

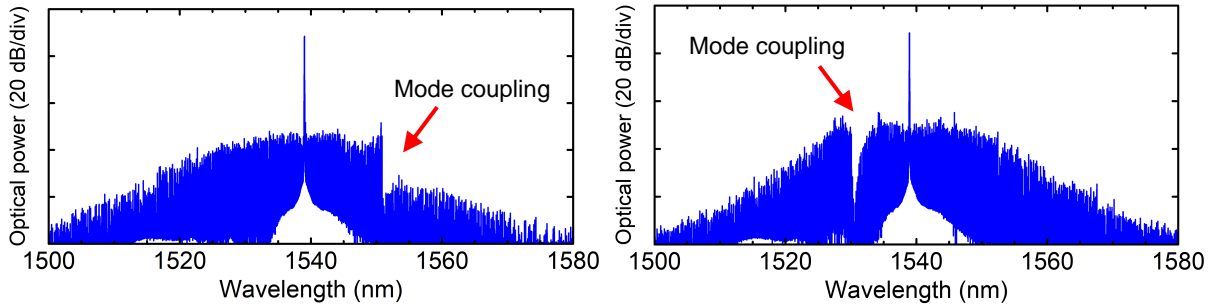


Fig. 3.9: Micrcomb spectra generated in a MgF_2 microresonator. The spectral envelopes are distorted by mode coupling between pump and other transverse modes. The mode coupling around the pump mode sometimes disturbs the generation of soliton microcombs.

3.2.3 Linewidth of a generated comb line with and without optomechanical oscillations

To evaluate the linewidth of generated comb lines, I performed heterodyne measurement between a comb line and a reference laser. The pump and reference lasers are external-cavity diode lasers (Santec TSL-510 and TSL-710), whose linewidths are 356 and 220 kHz, respectively (the detail is shown in Appendix B). Figure 3.10 shows the experimental setup for the comb linewidth measurement. A microcomb was generated from a toroid microresonator by scanning the pump wavelength. The one comb line was filtered out using a bandpass filter and was interfered with the reference laser. Figure 3.11(a) shows filtered comb power while scanning the pump wavelength. The comb power drastically changed at the wavelength from (i) to (ii), simultaneously with disappearing the optomechanics-induced signals. This behavior is explained in §4.3. Figure 3.11(b) shows microcomb spectra at the wavelengths (i) and (ii), whose yellow areas represent filtered comb lines. Figure 3.11(c) shows heterodyne signals between the filtered comb line and the reference laser. When optomechanical oscillations occurred at the wavelength (i), the heterodyne signal was very broad and weak. On the other hand, when optomechanical oscillations did not occur at the wavelength (ii), the heterodyne

linewidth was hundreds of kilohertz that is same order as that of the pump and reference lasers. Hence, the generated comb has same order or narrower compared with the pump laser. Also, OMPOs cause the phase noise that broadens the linewidth of generated comb lines.

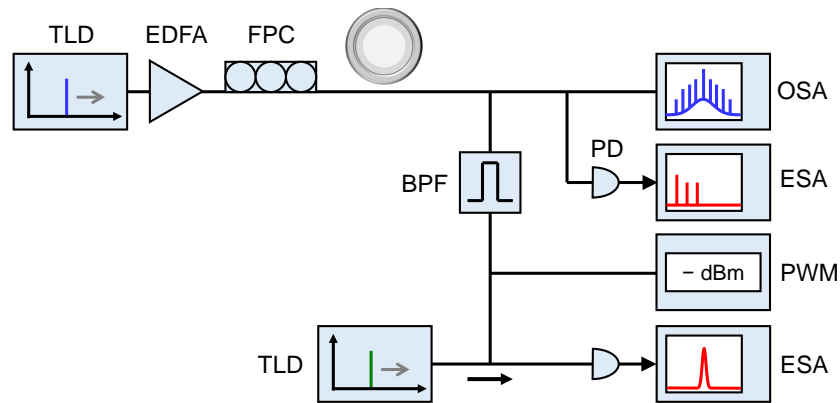


Fig. 3.10: Experimental setup for comb linewidth measurement by interfering the microcomb with a reference laser. A comb line is filtered out using a bandpass filter and is combined with the reference laser to measure the heterodyne signal. TLD: tunable laser diode, EDFA: erbium-doped fiber amplifier, FPC: fiber polarization controller, OSA: optical spectrum analyzer, PD: photodetector, ESA: electrical spectrum analyzer, BPF: bandpass filter, PWM: power meter.

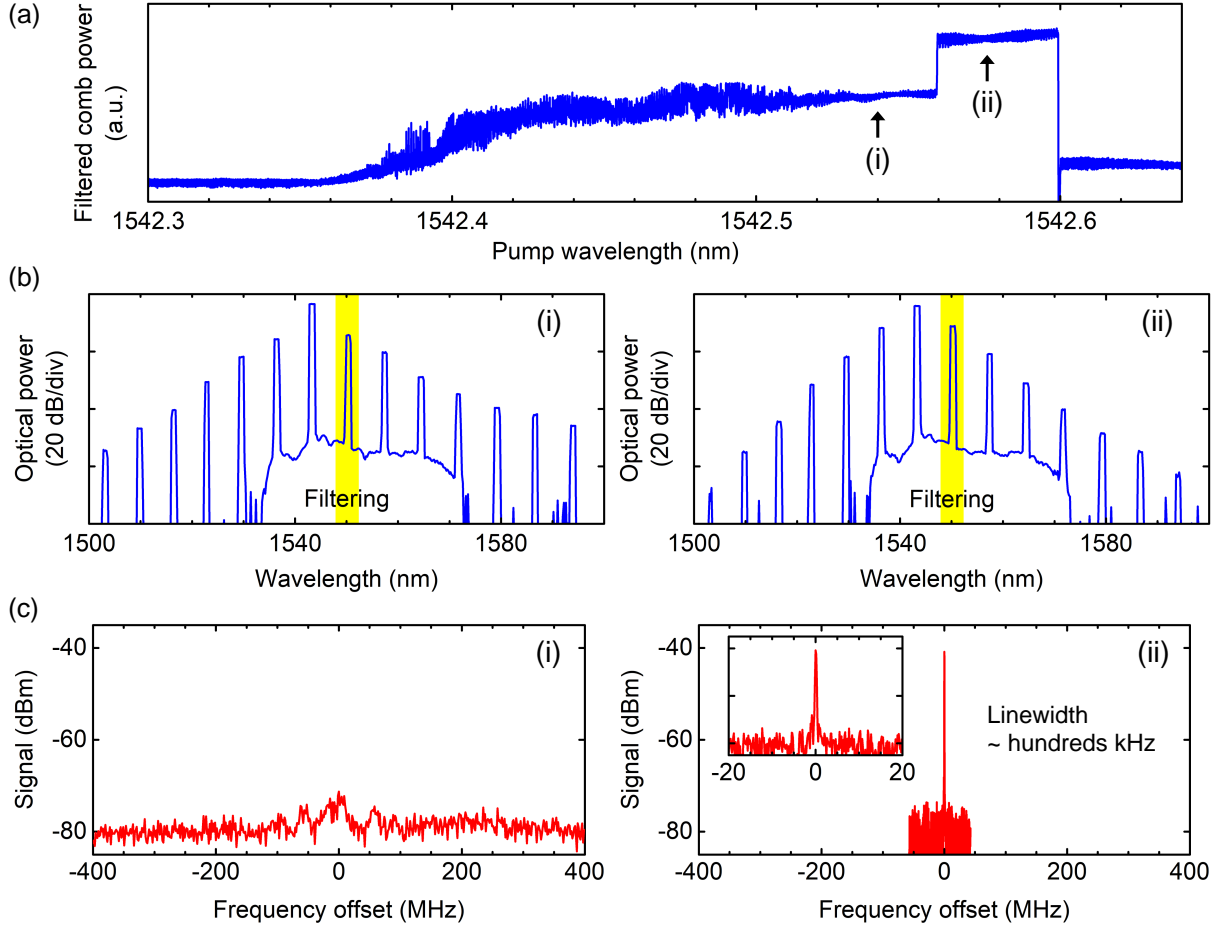


Fig. 3.11: (a) Filtered comb power while scanning the pump wavelength. The comb power drastically changed at the wavelength from (i) to (ii). In this transition, the optomechanics-induced signal in an electrical spectrum analyzer disappeared, whose behavior is explained in §4.3. (b) Microcomb spectra generated from a toroid microresonator at wavelengths (i) and (ii). The comb has a mode spacing that corresponds to the cavity FSR. The yellow areas represent filtered comb lines. (c) Heterodyne signals between the filtered comb line and the reference laser at the wavelengths (i) and (ii). At the wavelength (i) in optomechanical oscillations, the heterodyne signal was very broad and weak. On the other hand, at the wavelength (ii) in no optomechanical oscillations, the heterodyne linewidth was hundreds of kHz that is the same order as that of the pump and reference lasers.

Chapter 4

Suppression of optomechanical parametric oscillation in a toroid microresonator assisted by a microcomb

4.1 Introduction

4.1.1 Basic theory of cavity optomechanics

In this section, the basic theory of cavity optomechanics is explained to help in the understanding of my research results. The following discussion on the basic theory of optomechanics follows the work by Albert Schließer who studied amplification and cooling of mechanical motion in a toroid microresonator [148].

Radiation pressure backaction: static phenomena

A cavity optomechanical system is driven by the input field $s_{\text{in}}(t)$ which excites the internal field $a_0(t)$ and oscillation of the resonator boundary $x(t)$, as shown in Figs. 4.1(a) and (b). Since the oscillation changes the cavity length, the effective resonance frequency $\omega_0^{\text{eff}}(t)$ depends on the displacement as

$$\omega_0^{\text{eff}}(t) = \omega_0 + Gx(t), \quad (4.1)$$

where ω_0 is the cold resonance frequency (which does not take account of resonance shift by structure displacement and Kerr and thermal effects) and G is the resonance frequency shift per displacement as $G \equiv \partial\omega_0/\partial x$. Here, a whispering-gallery mode resonator with a radius R follows $G = -\omega_0/R$. Using Eq. (4.1), the optical coupling equation in Eq. (2.12) can be rewritten as

$$\frac{da_0(t)}{dt} = -\frac{\kappa}{2}a_0(t) + i\{\omega_p - (\omega_0 + Gx(t))\}a_0(t) + \sqrt{\kappa_c}s_{\text{in}}(t). \quad (4.2)$$

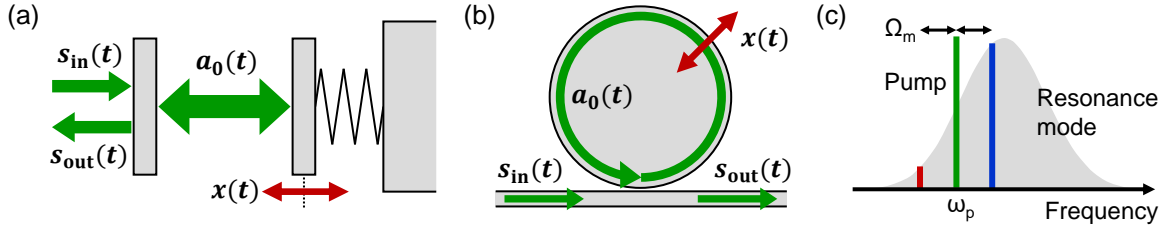


Fig. 4.1: Illustrations of cavity optomechanical systems with (a) a Fabry-Pérot resonator and (b) a whispering-gallery mode resonator. $a_0(t)$ and $x(t)$ represent the internal field and displacement of the resonator boundary, respectively. (c) Anti-Stokes and Stokes light which is generated from the pump laser with modulation at the oscillation frequency Ω_m .

In addition, since the optomechanical oscillation can be regarded as damped and forced oscillation, the behavior is given by

$$\frac{d^2x(t)}{dt^2} + \Gamma_m \frac{dx(t)}{dt} + \Omega_m^2 x(t) = -\frac{\hbar G}{m_{\text{eff}}} |a_0(t)|^2, \quad (4.3)$$

where Γ_m , Ω_m , and m_{eff} are the mechanical damping rate, the mechanical oscillation frequency, and the effective mass, respectively. Here, the radiation pressure force $F_{\text{rp}}(t)$, which is included on the right-hand side in Eq. (4.3), follows as

$$F_{\text{rp}}(t) = -\hbar G |a_0(t)|^2. \quad (4.4)$$

First, I calculate the static state in the optomechanical system with the constant input as $s_{\text{in}}(t) = \bar{s}_{\text{in}}$, which considers that the internal field and displacement become constant values as $a_0(t) = \bar{a}_0$ and $x(t) = \bar{x}$. Equations (4.2) and (4.3) can be written as

$$\bar{a}_0 = \frac{\sqrt{\kappa_c}}{\frac{1}{2}\kappa - i(\Delta\omega_0 - G\bar{x})} \bar{s}_{\text{in}}, \quad (4.5)$$

$$\bar{x} = -\frac{\hbar G}{m_{\text{eff}} \Omega_m^2} |\bar{a}_0|^2. \quad (4.6)$$

Figure 4.2 shows one example of stationary solutions in an optomechanical system. Since the radiation pressure pushes the boundary of the resonator which shifts the resonance frequency, the bistable behavior can be achieved with a sufficient input power and a high-Q resonator.

Radiation pressure backaction: dynamic phenomena

Next, I analyze the dynamics with fluctuations in the system around the equilibrium. The internal field $a_0(t)$ and displacement $x(t)$ are represented as

$$a_0(t) = \bar{a}_0 + \delta a_0(t), \quad (4.7)$$

$$x(t) = \bar{x} + \delta x(t), \quad (4.8)$$

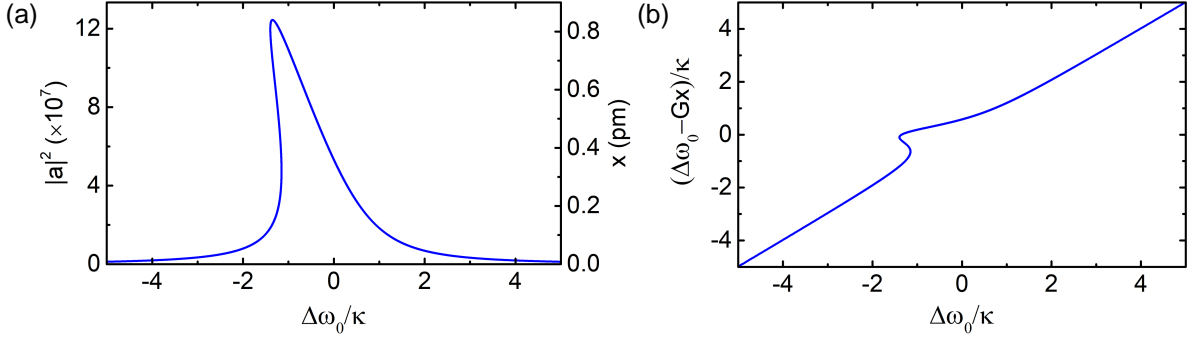


Fig. 4.2: Stationary solutions which are calculated with Eqs. (4.5) and (4.6) under the optomechanical system having $\kappa/2\pi = 4$ MHz, $\eta = 0.5$, $\omega_0/2\pi = 193$ THz, $\Omega_m/2\pi = 40$ MHz, $R = 30$ μm , $P_{\text{in}} = 0.2$ mW, and $m_{\text{eff}} = 1 \times 10^{-11}$ kg.

where \bar{a}_0 and \bar{x} are the stable equilibrium values and $\delta a_0(t)$ and $\delta x(t)$ are the fluctuations. Here, the equilibrium detuning is defined as

$$\Delta\omega_0^{\text{eff}} = \omega_p - (\omega_0 + G\bar{x}). \quad (4.9)$$

By substituting Eqs. (4.7)–(4.9) into Eqs. (4.2) and (4.3), the linearized equations with small external force $\delta F(t)$ can be obtained:

$$\frac{d}{dt}\delta a_0(t) = \left(-\frac{\kappa}{2} + i\Delta\omega_0^{\text{eff}}\right)\delta a_0(t) - iG\bar{a}_0\delta x(t), \quad (4.10)$$

$$\frac{d^2}{dt^2}\delta x(t) + \Gamma_m \frac{d}{dt}\delta x(t) + \Omega_m^2\delta x(t) = -\frac{\hbar G}{m_{\text{eff}}}\bar{a}_0\{\delta a_0(t) + \delta a_0^*(t)\} + \frac{\delta F(t)}{m_{\text{eff}}}. \quad (4.11)$$

Here, it is assumed that the terms with $\delta a_0(t)\delta x(t)$ or $|\delta a_0(t)|^2$ are neglected and $\bar{a}_0 = \bar{a}_0^*$ is satisfied. These equations can be easily solved in the frequency domain by utilizing Fourier transformation:

$$-i\Omega\delta a_0(\Omega) = \left(-\frac{\kappa}{2} + i\Delta\omega_0^{\text{eff}}\right)\delta a_0(\Omega) - iG\bar{a}_0\delta x(\Omega), \quad (4.12)$$

$$-i\Omega\delta a_0^*(\Omega) = \left(-\frac{\kappa}{2} - i\Delta\omega_0^{\text{eff}}\right)\delta a_0^*(\Omega) + iG\bar{a}_0\delta x(\Omega), \quad (4.13)$$

$$(-\Omega^2 - i\Gamma_m\Omega + \Omega_m^2)\delta x(\Omega) = -\frac{\hbar G}{m_{\text{eff}}}\bar{a}_0\{\delta a_0(\Omega) + \delta a_0^*(\Omega)\} + \frac{\delta F(\Omega)}{m_{\text{eff}}}. \quad (4.14)$$

Here $\delta a_0^*(\Omega) = \{\delta a_0(-\Omega)\}^*$ is used. The amplitude of anti-Stokes and Stokes sidebands at the bandwidth frequency Ω can be given by

$$\delta a_0(\Omega) = \frac{-iG\bar{a}_0}{\frac{1}{2}\kappa - i(\Delta\omega_0^{\text{eff}} + \Omega)}\delta x(\Omega), \quad (4.15)$$

$$\delta a_0^*(\Omega) = \frac{iG\bar{a}_0}{\frac{1}{2}\kappa + i(\Delta\omega_0^{\text{eff}} + \Omega)}\delta x(\Omega). \quad (4.16)$$

The amplitude modulation of the internal fields induces the radiation pressure force as

$$\begin{aligned}
 \delta F_{\text{rp}}(\Omega) &= -\hbar G \bar{a}_0 \{ \delta a_0(\Omega) + \delta a_0^*(\Omega) \} \\
 &= \hbar G^2 \bar{a}_0^2 \left\{ \frac{\Delta\omega_0^{\text{eff}} + \Omega}{\frac{1}{4}\kappa^2 + (\Delta\omega_0^{\text{eff}} + \Omega)^2} + \frac{\Delta\omega_0^{\text{eff}} - \Omega}{\frac{1}{4}\kappa^2 + (\Delta\omega_0^{\text{eff}} - \Omega)^2} \right\} \delta x(\Omega) \\
 &\quad + i\hbar G^2 \bar{a}_0^2 \left\{ \frac{\frac{1}{2}\kappa}{\frac{1}{4}\kappa^2 + (\Delta\omega_0^{\text{eff}} + \Omega)^2} - \frac{\frac{1}{2}\kappa}{\frac{1}{4}\kappa^2 + (\Delta\omega_0^{\text{eff}} - \Omega)^2} \right\} \delta x(\Omega). \quad (4.17)
 \end{aligned}$$

The radiation pressure force in an optomechanical system induces dynamical behavior, which is known as dynamical backaction [132]. As shown in Eq. (4.14), the real and imaginary parts correspond to the mechanical damping rate Γ_m and oscillation frequency Ω_m . Therefore, by substituting Eq. (4.17) into Eq. (4.14), the effective mechanical damping rate Γ_{eff} and effective oscillation frequency Ω_{eff} are obtained as

$$\begin{aligned}
 \Gamma_{\text{eff}} &= \Gamma_m + \Gamma_{\text{opt}} \\
 &= \Gamma_m + \frac{\hbar G^2 \bar{a}_0^2}{m_{\text{eff}} \Omega_m} \left\{ \frac{\frac{1}{2}\kappa}{\frac{1}{4}\kappa^2 + (\Delta\omega_0^{\text{eff}} + \Omega_m)^2} - \frac{\frac{1}{2}\kappa}{\frac{1}{4}\kappa^2 + (\Delta\omega_0^{\text{eff}} - \Omega_m)^2} \right\} \\
 &= \Gamma_m + \bar{a}_0^2 g_{\text{om}}^2 \left\{ \frac{\kappa}{\frac{1}{4}\kappa^2 + (\Delta\omega_0^{\text{eff}} + \Omega_m)^2} - \frac{\kappa}{\frac{1}{4}\kappa^2 + (\Delta\omega_0^{\text{eff}} - \Omega_m)^2} \right\}, \quad (4.18)
 \end{aligned}$$

$$\begin{aligned}
 \Omega_{\text{eff}} &= \Omega_m + \Omega_{\text{opt}} \\
 &= \Omega_m + \frac{\hbar G^2 \bar{a}_0^2}{2m_{\text{eff}} \Omega_m} \left\{ \frac{\Delta\omega_0^{\text{eff}} + \Omega_m}{\frac{1}{4}\kappa^2 + (\Delta\omega_0^{\text{eff}} + \Omega_m)^2} + \frac{\Delta\omega_0^{\text{eff}} - \Omega_m}{\frac{1}{4}\kappa^2 + (\Delta\omega_0^{\text{eff}} - \Omega_m)^2} \right\} \\
 &= \Omega_m + \bar{a}_0^2 g_{\text{om}}^2 \left\{ \frac{\Delta\omega_0^{\text{eff}} + \Omega_m}{\frac{1}{4}\kappa^2 + (\Delta\omega_0^{\text{eff}} + \Omega_m)^2} + \frac{\Delta\omega_0^{\text{eff}} - \Omega_m}{\frac{1}{4}\kappa^2 + (\Delta\omega_0^{\text{eff}} - \Omega_m)^2} \right\}, \quad (4.19)
 \end{aligned}$$

$$g_{\text{om}} = G \cdot x_{\text{ZPF}} = -\frac{\omega_0}{R} \cdot \sqrt{\frac{\hbar}{2m_{\text{eff}} \Omega_m}}, \quad (4.20)$$

where g_{om} is the optomechanical single-photon coupling strength and x_{ZPF} is the mechanical zero-point fluctuation amplitude.

Optomechanical parametric oscillations

Vladimir B. Braginsky predicted that optical-mechanical mode coupling can lead to optomechanical parametric oscillations (OMPOs) due to the radiation pressure [149]. Since the optomechanical amplification and damping are expressed in Eq. (4.18), OMPOs occur when the effective damping rate Γ_{eff} is a negative value. Figure 4.3 shows an example of a calculated effective damping rate whose parameters follow the microresonator in Fig. 4.4(b). Also, the input power and coupling parameter η are 0.2 mW and 0.5, respectively. As shown in Fig. 4.3, the calculated effective damping rates with κ of $0.5\Omega_m$ and Ω_m reach a negative value when the $\Delta\omega_0/\Omega_m$ is

between 0.2 to 1.2. In this blue-detuned regime, OMPO occurs and the measured effective damping rate becomes close to zero hertz.

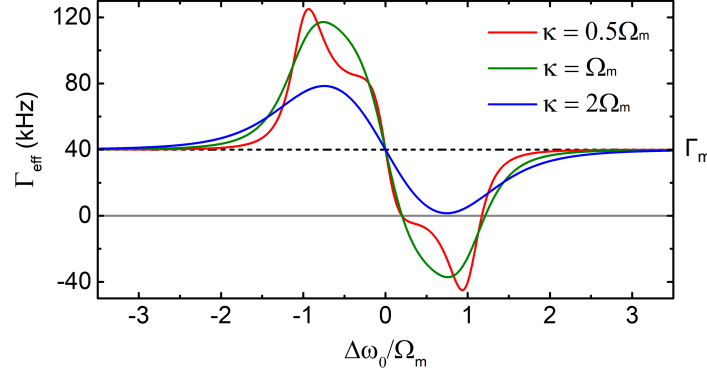


Fig. 4.3: Calculation of an effective damping rate using Eq. (4.18) whose calculation parameters follow the microresonator in Fig. 4.4(b). Also, the input power and coupling parameter η are 0.2 mW and 0.5, respectively. The linewidths of optical mode are set to $0.5\Omega_m$ (red), Ω_m (green), and $2\Omega_m$ (blue). The black dashed line denotes the mechanical damping rate. In the blue-detuned regime with $\Gamma_{\text{eff}} < 0$, OMPOs occur and the measured effective damping rate becomes close to zero hertz

4.1.2 Measurement and simulation of mechanical modes in toroid microresonators

A silica toroid microresonator is a suitable platform for observation of OMPOs thanks to its high-Q and micron-size. To evaluate the properties of mechanical modes and observe OMPOs experimentally, I excited a toroid microresonator with a CW laser through a tapered fiber and measured the output light using a photodetector connected to an electrical spectrum analyzer. Since the output light is modulated with the oscillation, the photodetector signal has modulation peaks in the frequency domain (typically tens of megahertz in toroid microresonators). In addition, since the optomechanical coupling excites the eigenmode in mechanical modes depending on the structure, the excited mechanical mode can be simulated and estimated by using finite element simulation. Here, I used the software "COMSOL Multiphysics" as a finite element simulation solver. As shown in 2.28, the simulated mechanical frequency is in good agreement with measured one.

When pumping with a weak power (below the threshold for OMPOs) and a large detuning ($|\Delta\omega_0| \gg \Omega_m$), a mechanical damping rate can be obtained by measuring the linewidth of the mechanical mode. Figure 4.4 shows measured photodetector signals induced by the optomechanical oscillations in different microresonator structures: (a) before and (b) after additional XeF_2 gas etching to the silicon pillar, as shown in the inset microscope images. Hence, microresonator structures (including the diameter, minor diameter, and thickness of silica disk) are the same except for diameter of the silicon pillar. A thinner pillar leads to a narrower linewidth (higher mechanical Q factor) and a lower mechanical frequency. The mechanical Q factor (Q_m)

is defined as

$$Q_m = \Omega_m / \Gamma_m . \quad (4.21)$$

In addition, a microresonator structures determines an effective mass which can be calculated with a finite element simulation:

$$m_{\text{eff}} = \frac{\rho \iiint x^2 dV}{x_{\text{max}}^2} . \quad (4.22)$$

Here ρ is the material density ($2.2 \times 10^3 \text{ kg/m}^3$ in silica), x is the displacement, and x_{max} is the maximum displacement. The toroid microresonators shown in Fig. 4.4 have the effective masses of $4.7 \times 10^{-11} \text{ kg}$ (before etching) and $2.7 \times 10^{-11} \text{ kg}$ (after etching). Figure 4.5 shows (a) measured photodetector signals that depend on the detuning between pump and resonance frequencies, and (b) the detail of the signals. When the pump frequency is scanned to lower in the blue-detuned regime, mechanical mode is excited first (green) and then OMPO occurs (red).

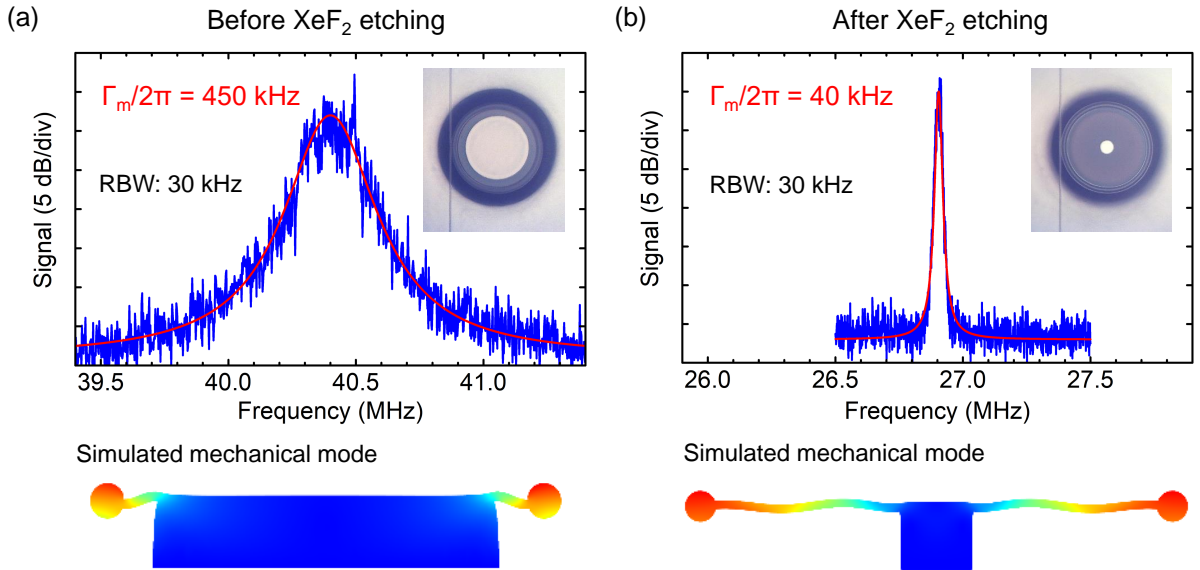


Fig. 4.4: Measured mechanical modes in a toroid microresonator (a) before and (b) after XeF_2 etching. Before (after) the etching, the toroid microresonator has a diameter of $117 \mu\text{m}$, a minor diameter of $7.6 \mu\text{m}$, a disk thickness of $2 \mu\text{m}$, and a pillar diameter of $80.7 \mu\text{m}$ ($17.5 \mu\text{m}$). Since mechanical parameters depend on the microresonator structure, the mechanical oscillation frequency, mechanical damping rate, and effective mass are changed. The measured mechanical frequency $\Omega_m/2\pi$ is 40.4 MHz (26.9 MHz), which is in good agreement with simulation results of 41.9 MHz (26.7 MHz). The measured damping rate $\Gamma_m/2\pi$ and calculated effective mass m_{eff} are 450 kHz (40 kHz) and $4.7 \times 10^{-11} \text{ kg}$ ($2.7 \times 10^{-11} \text{ kg}$), respectively. Red lines represent Lorentzian functions. The bottom figures show simulated mechanical modes.

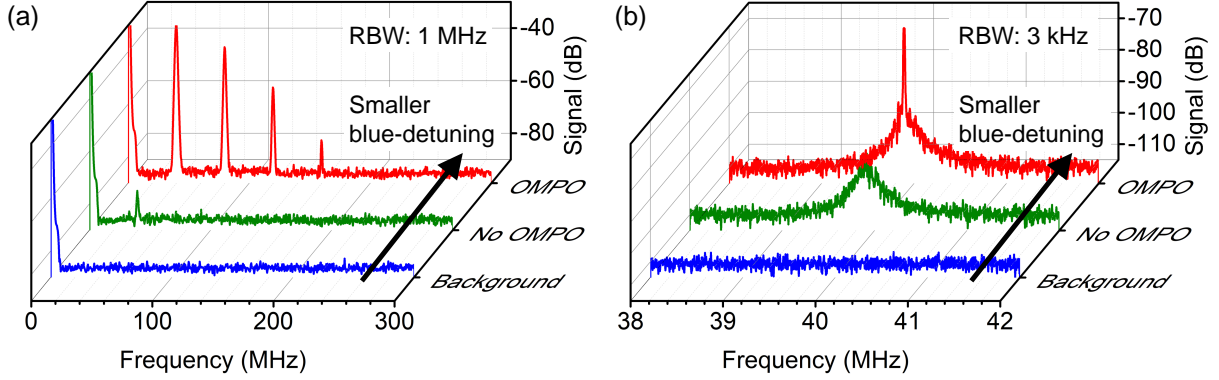


Fig. 4.5: (a) Measured photodetector signals that depend on the detuning between pump and resonance frequencies, and (b) the detail of the signal. When the pump frequency is scanned to lower in the blue-detuned regime, mechanical mode is excited first (green) and then OMPO occurs (red).

4.1.3 Motivation

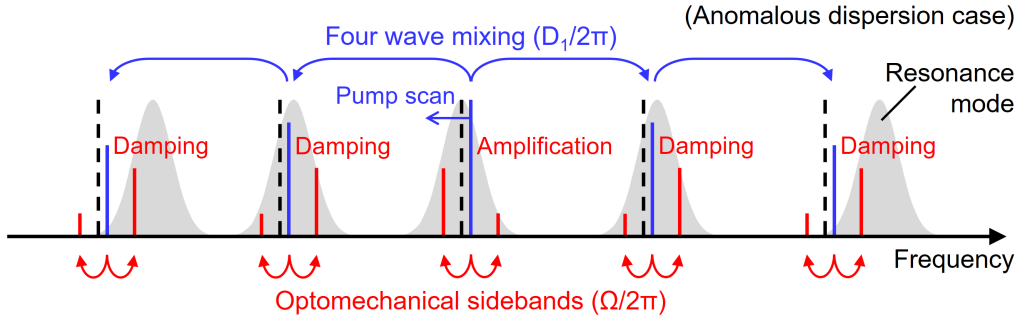


Fig. 4.6: Amplification and damping mechanisms in an optomechanical coupled system. Optomechanical oscillation is suppressed (amplified) when the light is coupled to the resonance with red-detuning (blue-detuning). When a Turing pattern comb is generated, the pump line is always at blue-detuning and the generated comb lines are at red-detuning. Since the pump line and all the generated comb lines contribute to the cavity optomechanical behavior, the system may exhibit amplification and suppression depending on the parameters.

A high-Q toroid microresonator pumped with a CW laser leads to a strong circulating power inside the microresonator. The high optical density causes radiation pressure, which excites the mechanical oscillation modes in the microresonator structure and leads to OMPOs [78, 133]. Figure 4.6 shows the amplification and damping mechanisms caused by symmetric optomechanical sidebands. This illustration includes two new photon generation processes. The first is optomechanical oscillation, which generates Doppler-shifted photons at blue and red sidebands. When pumping with blue-detuning (the pump has a higher frequency than the resonance), the resonance suppresses the blue sideband and enhances the red sideband. In this case, the optomechanical oscillation is enhanced. On the other hand, the optomechanical

oscillation is suppressed when pumping with red-detuning (the pump has a lower frequency than the resonance). The second process is FWM, which generates photons in other resonances with equal mode spacings. Pump scanning from a high to a low frequency is employed for FWM generation because the resonance frequency is shifted by thermal and Kerr effects. Here Turing pattern combs (also known as primary combs) [52, 150, 151] are generated, whose pump line was always on the blue-detuned side [39, 142]. Therefore, in theory, the microresonator structure should oscillate if only the influence of the strong pump light is considered. However, the key is that the generated comb lines also influence the optomechanical amplification and damping. While generating a microcomb (Turing pattern comb), the suppression of OMPO is both expected and observed as shown in the next section. Here the author tries to understand the cavity optomechanical behavior when a microcomb is generated in a toroid microresonator.

4.2 Experimental observation of suppression of optomechanical parametric oscillation

Figure 4.7(a) shows our experimental setup. Amplified CW light, whose polarization was aligned with a polarization controller, was coupled to a silica toroid microresonator using a tapered fiber. The output light was monitored using an optical spectrum analyzer and two photodetectors connected to an oscilloscope and an electrical spectrum analyzer. In addition, a weak probe laser was launched into a microresonator in the counter direction to measure the detuning values between the resonance and generated comb line frequencies while generating a microcomb. Figure 4.7(b) shows a resonance mode with a beat signal between the probe laser and the comb line. The measured detuning was calibrated using a fiber MZI with a FSR of 19.7 MHz.

Table 4.1 summarizes the parameters of the microresonator structure and the mechanical properties. The minor radius is that of the cross section of a toroidal structure. $\Omega_m/2\pi$ is the mechanical oscillation frequency. The effective mass (m_{eff}) was calculated by using a finite element simulation, whose mechanical mode is shown in Fig. 4.7(a) (inset). The calculated mechanical frequency is in good agreement with the measurement ($\Omega_m/2\pi = 40$ MHz). In the experiment, a tapered fiber was brought into contact with the microresonator surface to realize a stable coupling condition that reduced the mechanical Q from 130 to 100 [152] (The calculation of mechanical modes did not take the fiber into account). The optical intrinsic Q (Q_i) of the modes used for the microcomb generation was about 1×10^7 .

Figure 4.7(c) shows the dispersion of the transverse mode used for the microcomb generation, which was obtained from the FSR distances. The cold resonant frequencies are given with

Table. 4.1: Parameters of the toroid microresonator used in this experiment

Radius	Minor radius	Pillar radius	$\Omega_m/2\pi$	Q_m	m_{eff} (calculation)
59 μm	4.5 μm	40 μm	40 MHz	100	3.3×10^{-11} kg

4.2. Experimental observation of suppression of optomechanical parametric oscillation

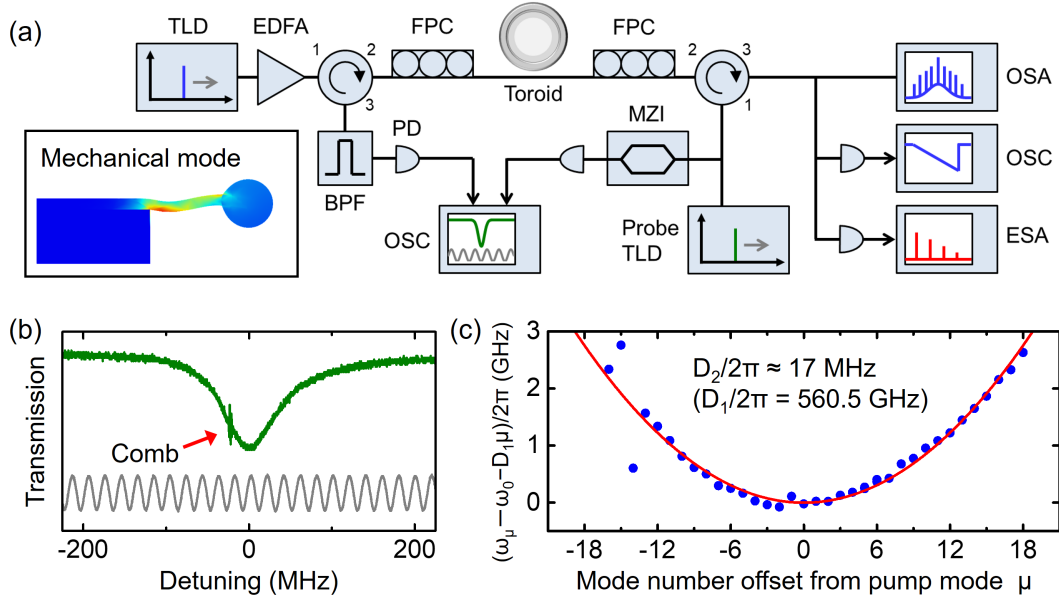


Fig. 4.7: (a) Experimental setup for microcomb generation and measurement of detuning between resonance and comb line frequencies. During microcomb generation, a weak probe laser was scanned through the resonance in the counter direction to the pump laser. The inset shows a mechanical mode excited in this experiment and whose frequency is calculated as 40 MHz by using a finite element simulation. TLD: tunable laser diode, EDFA: erbium-doped fiber amplifier, FPC: fiber polarization controller, OSA: optical spectrum analyzer, PD: photodetector, OSC: oscilloscope, ESA: electrical spectrum analyzer, MZI: fiber Mach-Zehnder interferometer, BPF: tunable bandpass filter. (b) Resonance mode profile with a beat signal between the probe laser and the comb line (green), whose detuning was calibrated using a fiber MZI (gray). (c) Measured dispersion of the transverse mode used for microcomb generation (blue points) with respect to the mode number offset from the pump mode. The red curve is a parabolic fitting using a $D_2/2\pi$ value of 17 MHz. The deviated points are shifted by mode coupling with other transverse modes.

relative mode number μ (the pump mode corresponds to $\mu = 0$) as

$$\omega_\mu = \omega_0 + D_1\mu + \frac{1}{2}D_2\mu^2 + \dots, \quad (4.23)$$

which is explained in §2.1.1. The dispersion of the transverse mode used for the microcomb generation is anomalous; the values are $D_1/2\pi = 560.5$ GHz and $D_2/2\pi \approx 17$ MHz. The higher order terms are negligible.

Figure 4.8(a) shows the transmission power when scanning the pump laser from a short to a long wavelength. The cold resonance wavelength was 1560.85 nm, which corresponds to a 0 ms scan time. The total Q (Q) was about 3.5×10^6 . Figures 4.8(b) and 4.8(c) show typical measured optical spectra and radio frequency (RF) signals in states (i), (ii), and (iii). First, neither a microcomb nor an OMPO was observed in state (i) because the intracavity power was below the threshold. Then RF signals at multiples of 40 MHz appeared in state (ii), which is the result of the

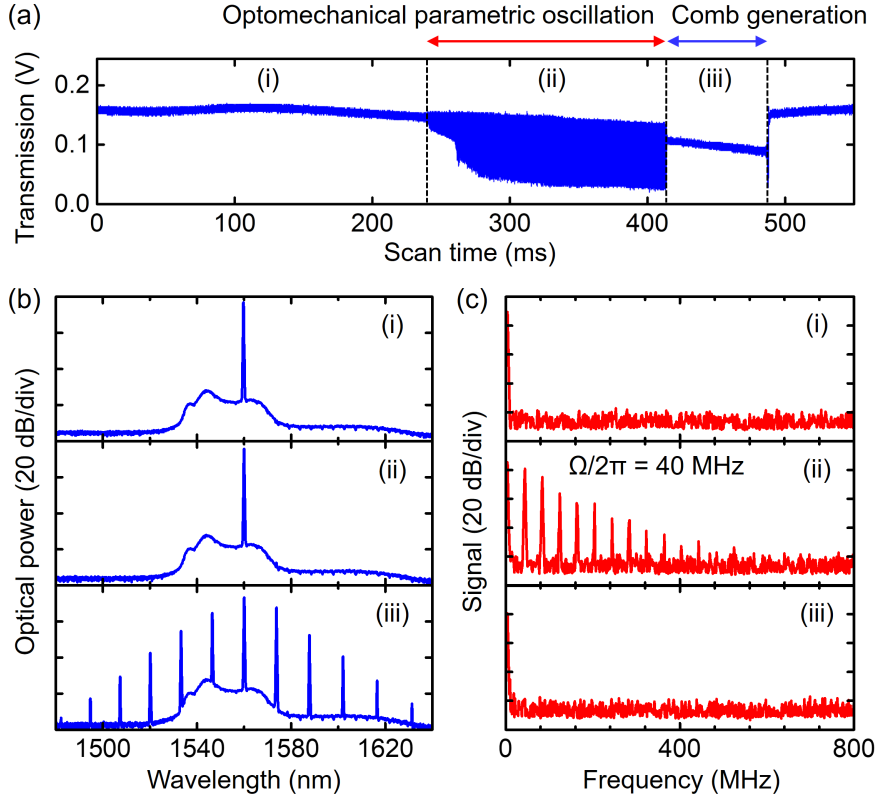


Fig. 4.8: (a) Transmission when scanning pump laser from a short to a long wavelength. The pump power was 280 mW. In state (ii), OMPOs occurred without microcomb generation, which caused the transmission fluctuation. After a Turing pattern comb generation, the fluctuation was suppressed as shown in state (iii). (b) and (c) Typical measured optical spectra and detected RF signals in state (i), (ii) and (iii). The RF signal in state (ii) had harmonics of 40 MHz, which was in agreement with a calculated mechanical frequency.

OMPO excited by the CW pump. The oscillation frequency agrees with the calculated frequency of the mechanical mode shown in the inset of Fig. 4.7(a). Since no microcomb has been generated at this condition, the transmission fluctuation in state (ii) was caused solely by the OMPO. Then a microcomb starts to appear in state (iii) which was a Turing pattern microcomb that had a smooth envelope with a mode spacing of 3-FSR ($= 560.5 \text{ GHz} \times 3$). Surprisingly, the OMPO was suppressed after the comb was generated. Since a Turing pattern comb is generated via a strong blue-detuned pump, the microresonator structure should oscillate only if the influence of the pump light is considered. Our observation of the suppression of the optomechanical oscillation indicates that the generated comb lines influenced the optomechanical behavior in the toroid microresonator, as predicted in Fig. 4.6. In the next section, I compare the mechanical and optomechanical damping rates by taking generated comb lines into account.

4.3 Discussion on experimental observations

4.3.1 Model of multi-optomechanical coupling

The optomechanical behavior of a microresonator is defined by the effective mechanical damping rate (Γ_{eff}) [14, 134]. The effective damping rate obeys the following relationship between the mechanical (Γ_{m}) and optomechanical (Γ_{opt}) damping rates:

$$\Gamma_{\text{eff}} = \Gamma_{\text{m}} + \sum_{\mu} \Gamma_{\text{opt},\mu}. \quad (4.24)$$

The optomechanical damping rate is given by

$$\Gamma_{\text{opt},\mu} = |a_{\mu}|^2 g_{\text{om}}^2 \left\{ \frac{\kappa}{\frac{1}{4}\kappa^2 + (\Delta\omega_{\mu} + \Omega_{\text{m}})^2} - \frac{\kappa}{\frac{1}{4}\kappa^2 + (\Delta\omega_{\mu} - \Omega_{\text{m}})^2} \right\}, \quad (4.25)$$

where $|a_{\mu}|^2$ is the number of photons circulating inside the microresonator, which is coupled to the resonant mode μ ($\hbar\omega_{\mu}|a_{\mu}|^2 \times D_1/2\pi$ corresponds to the circulating power). \hbar is the Planck constant divided by 2π . κ is the optical cavity decay rate ($= \omega_0/Q$) and $\Delta\omega_{\mu}/2\pi$ is the detuning between the coupled light and resonance frequencies at resonance mode μ . g_{om} is the optomechanical single-photon coupling strength:

$$g_{\text{om}} = G \cdot x_{\text{ZPF}} = \frac{\omega_0}{R} \cdot \sqrt{\frac{\hbar}{2m_{\text{eff}}\Omega_{\text{m}}}}. \quad (4.26)$$

G is the resonance angular frequency shift per displacement, x_{ZPF} is the mechanical zero-point fluctuation amplitude, and R is the cavity radius. κ and g_{om} are regarded as independent of the resonance mode μ . Since the optomechanical damping rate can be both positive and negative, the effective damping rate increases or decreases depending on the sign. The change in the effective damping rate leads to the amplification or damping of the mechanical motion. Note that $\Gamma_{\text{eff}} < 0$ induces an OMPO, which causes a large change in the photodetector signal in the RF regime as shown in Fig. 4.8(c).

4.3.2 Excitation of mechanical mode with continuous-wave

I calculated the effective damping rate by using Eq. (4.24) but with a single resonance mode ($\Gamma_{\text{eff}} = \Gamma_{\text{m}} + \Gamma_{\text{opt},0}$) that assumes there is no FWM generation. The number of photons $|a_0|^2$ is obtained from a coupled mode equation, such as,

$$|a_0|^2 = \frac{\kappa_{\text{c}}}{\frac{1}{4}\kappa^2 + \Delta\omega_0^2} |s_{\text{in}}|^2, \quad (4.27)$$

where s_{in} is the input field ($\hbar\omega_0|s_{\text{in}}|^2$ corresponds to the input power), κ_{c} is the optical coupling rate to the waveguide ($= \omega_0/Q_{\text{c}}$), Q_{c} is the coupling Q, which has the relation $Q^{-1} = Q_{\text{i}}^{-1} + Q_{\text{c}}^{-1}$.

The calculation parameters were chosen to follow the experimental condition. The mechanical damping rate $\Gamma_m/2\pi$ was 40 kHz, which obeys $\Gamma_m = \Omega_m/Q_m$. By taking all the parameters into account, the pump detuning range for OMPO ($\Gamma_{\text{eff}} < 0$) was calculated to have a 7 kHz to 355 MHz range. Since this analytical approach can be applied when the system is pumped with a CW light, the transition from state (i) to (ii) in Fig. 4.8(a) should occur when the pump approaches a detuning of 355 MHz. According to this CW pump model, the OMPO should remain even in the detuning range of state (iii), if no FWM process has occurred and only the pump light influenced the system. However, this is not the case with the experiment as shown in Fig. 4.8. Since the photons in the pump mode were converted to other resonance modes via FWM in the experiment, the excitation of the optomechanical mode with multi-optical resonances is needed to be taken into account.

4.3.3 Excitation of mechanical mode with microcomb

It is straightforward to analyze the optomechanical behavior of a toroid microresonator excited with a single frequency by using Eqs. (4.24) and (4.25). On the other hand, it is not easy to couple an LLE directly with Eq. (4.25), because the effective detuning and the intracavity photon number are needed to be obtained while generating a microcomb. It should be noted that $\Delta\omega_\mu$ in Eq. (4.25) is the effective detuning. Here, instead of the full calculation approach, I calculated the effective damping rate by assuming that the shape of the Turing pattern comb does not change with respect to the detuning. The intracavity photon numbers of the comb lines were obtained from the LLE calculation, and the effective pump detuning was measured in the experiment. The other detuning values of the comb sidebands (generated comb lines) are obtained by assuming the comb has a mode spacing of $D_1/2\pi$, which was confirmed with the measurement.

First, to obtain the numbers of photons in each resonance mode, I use an LLE model as given by [135, 138, 139, 153]

$$\frac{\partial a(\phi, t)}{\partial t} = -\frac{\kappa}{2}a + i\Delta\omega_{\text{cold},0}a + i\frac{D_2}{2}\frac{\partial^2 a}{\partial \phi^2} + ig|a|^2a + \sqrt{\kappa_c}s_{\text{in}}, \quad (4.28)$$

where $a(\phi, t)$ is the internal field including the multi resonance mode ($|a|^2$ indicates the intracavity photon numbers in the modes), ϕ is the angular coordinate in a microresonator, t is the slow time, $\Delta\omega_{\text{cold},0}$ is the cold pump detuning, and g is the nonlinear coefficient as $g = (\hbar\omega_0^2 n_2 D_1)/(2\pi n^2 A_{\text{eff}})$. n_2 is the nonlinear refractive index of silica and A_{eff} is the effective mode area. The toroid microresonator has an effective mode area of $12 \mu\text{m}^2$. The output field is given as $\sqrt{\kappa_c}a - s_{\text{in}}$. Figure 4.9(a) shows the calculated output spectrum for a Turing pattern comb, which is in good agreement with the experiment shown in state (iii) of Fig. 4.8(b). The red points in Fig. 4.9(a) show the number of photons inside the microresonator in each resonant mode.

Next, I measured the effective detuning $\Delta\omega_\mu$ of the pump and the generated comb lines in a hot microresonator. So, I performed a detuning measurement while generating a 3-FSR Turing pattern comb by launching a probe laser in the counter direction [142]. The detuning values of the pump laser ($\mu = 0$) and the first sidebands ($\mu = \pm 3$) were measured as shown in Fig. 4.9(b)

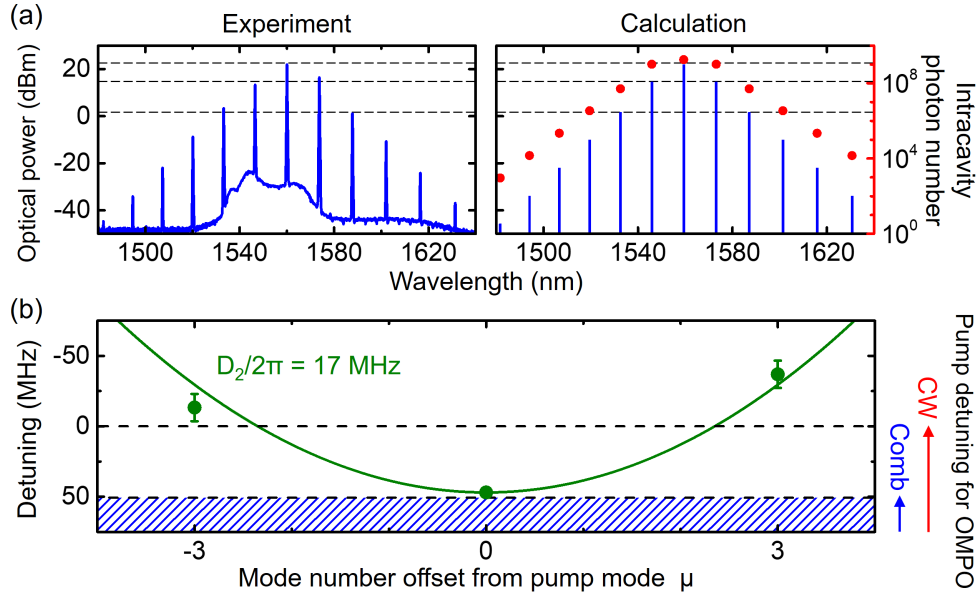


Fig. 4.9: (a) Measured and calculated output optical spectra of Turing pattern combs in state (iii) (blue lines). The black dash lines show the optical powers of calculated comb lines ($\mu = 0, \pm 3, \pm 6$), which are in good agreement with the experiment. The red points show the photon numbers inside a microresonator (log scale). (b) The green points represent measured detuning values from each resonance frequency when generating a 3-FSR Turing pattern comb. The pump detuning was 47 MHz. The pump was blue-detuned and the generated comb lines were red-detuned, which follow the microresonator dispersion (green curve) measured in Fig. 4.7(c). In the condition for generating a comb shown in Fig. 4.8(b), the calculated pump detuning for OMPO ($\Gamma_{\text{eff}} < 0$) was from 51 to 222 MHz in the blue-detuned side.

(green points). Since FWM occurs with frequency spacing at multiple of $D_1/2\pi$, the angular frequencies of comb lines are given by $\omega_p + D_1\mu$ (ω_p is the pump angular frequency). Hence the detuning of the generated comb lines should follow the cavity dispersion as follows

$$\Delta\omega_\mu = (\omega_p + D_1\mu) - (\omega_0 + D_1\mu + \frac{1}{2}D_2\mu^2) \quad (4.29)$$

$$= \Delta\omega_0 - \frac{1}{2}D_2\mu^2. \quad (4.30)$$

Indeed the measured detuning in Fig. 4.9(b) is in good agreement with the cavity dispersion (red line) obtained from the measurement shown in Fig. 4.7(c). Figure 4.9(b) shows that the pump laser was at blue-detuning and the sidebands were at red-detuning. These three lines have a strong influence on the optomechanical damping rate because of the relatively high power and the detuning.

It should be noted that, when the Turing pattern comb appears, all the generated comb lines are always in the red-detuning regime except for the pump light in an anomalous dispersion microresonator ($D_2 > 0$). Hence the generated comb lines are always contributing to the suppression of the OMPO as illustrated in Fig. 4.6. To confirm the validity of our model, I calculated an effective mechanical damping rate using Eq. (4.24). I used the measured pump

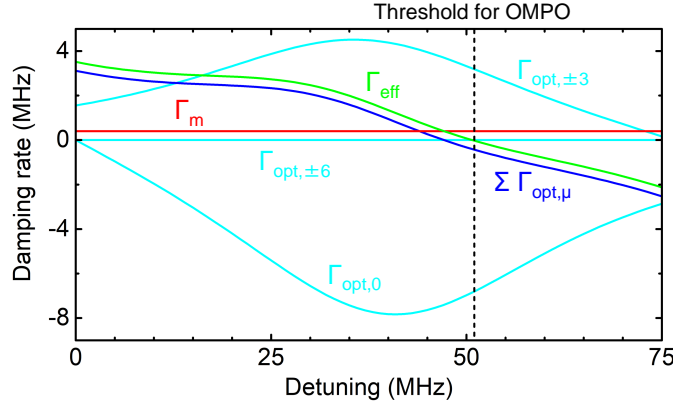


Fig. 4.10: Damping rates of each value in Eq. 4.24 as a function of the pump detuning. The light blue curves represent optomechanical damping rates induced by comb lines with $\mu = 0$ (pump), $\pm 3, \pm 6$. The blue curve represents sum of the optomechanical damping rates. The blue, red, and green curves represent sum of the optomechanical damping rates, the mechanical damping rate, and the effective damping rates, respectively. The larger detuning than threshold for OMPO (black dashed line) corresponds to the blue shaded area in Fig. 4.9 that denotes the OMPO excitation.

detuning ($\Delta\omega_0/2\pi = 47$ MHz) in state (iii) of Fig. 4.8(b). The detuning values for the generated comb lines are obtained with Eq. (4.30). The number of photons inside the microresonator is obtained from Fig. 4.9(a). The calculated pump detuning for OMPO ($\Gamma_{\text{eff}} < 0$) was in the 51 to 222 MHz range shown in Fig. 4.9(b). The measured detuning was smaller than 51 MHz (i.e. outside the OMPO range), which indicates the suppression of the OMPO and explains the experimental behavior well. Figure 4.10 shows damping rates of each value in Eq. (4.24). The larger detuning than threshold for OMPO (black dashed line) corresponds to the blue shaded area in Fig. 4.9 that denotes the OMPO excitation. The calculation result is in good agreement with the experiment observation and our simple model sufficiently explained that the OMPO could be suppressed under the condition in state (iii) of Fig. 4.8.

4.4 Measurement and calculation with a different toroid microresonator

In this section, I performed the same measurement and calculation using a different toroid microresonator to show that our simple model is valid even when a cavity with different parameters is used. Figure 4.11 shows microscope images of toroid microresonators used in §4.2 (left) and this section (right). The mechanical properties of the microresonator are shown in Table 4.2. The total Q was about 2×10^6 and the cavity dispersion $D_2/2\pi$ was 50 MHz in the toroid microresonator used in this section.

Figures 4.12(a)–(c) show the transmission power, optical spectra, and RF beat signals while scanning a pump laser. In state (iv), I observed a 3-FSR Turing pattern comb ($= 970.6$ GHz $\times 3$) without the RF signal induced by OMPO. The green points in Fig. 4.12(d) show the measured

4.4. Measurement and calculation with a different toroid microresonator

Table. 4.2: Parameters of the toroid microresonator that provided the results in Fig. 4.12

Radius	Minor radius	Pillar radius	$\Omega_m/2\pi$	Q_m	m_{eff} (calculation)
34 μm	2.3 μm	1.7 μm	46 MHz	1100	1.2×10^{-11} kg

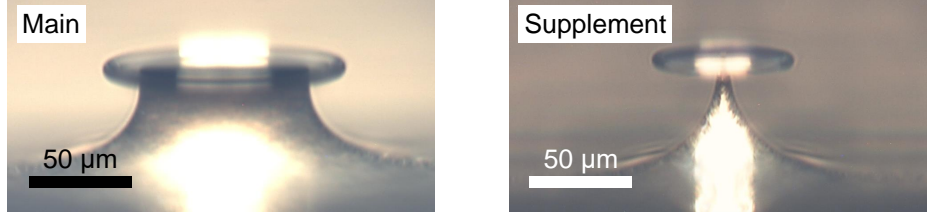


Fig. 4.11: Optical microscope images of toroid microresonators used in §4.2 (left) and this section (right).

detuning values, which followed the microresonator dispersion ($D_2/2\pi = 50$ MHz), when generating the comb shown in state (iv). The calculated pump detuning for $\Gamma_{\text{eff}} > 0$ (suppression of the OMPO) in the blue-detuned side was from 139 to 219 MHz, which I obtained by assuming the optical spectrum power in state (iv). The measured pump detuning ($\Delta\omega_0/2\pi = 191$ MHz) stayed within the calculated detuning range. On the other hand, in our analysis of a CW case, the calculated pump detuning values for $\Gamma_{\text{eff}} > 0$ were $\Delta\omega_0/2\pi > 755$ MHz and $\Delta\omega_0/2\pi < 0.19$ kHz. Hence the different microresonator also suppressed the OMPO assisted by a Turing pattern comb even though the transmittance signal in Fig. 4.12(a) behaved differently from that in Fig. 4.8.

The difference is due to the presence of states (iii) and (v) where the OMPO is not fully suppressed even after the generation of the comb (due to the strong influence of the pump line). This behavior is mainly due to the large cavity dispersion. FWM starts to occur at a pump detuning of 225 MHz, which is determined by cavity dispersion, optical Q, and input power. It should be noted that FWM at 3-FSR starts to occur when the red curve in Fig. 4.12 approaches the zero detuning line at $\mu = \pm 3$. So the system starts to exhibit the suppression of OMPO. However, with these cavity parameters, the damping provided by the two FWM sidebands was insufficient to completely stop the OMPO (state (iii)). Then the OMPO stops when the input laser is further scanned (state (iv)) because the detuning values of two FWM sidebands were close to the mechanical frequency. Finally, the microresonator oscillates again because the influence of the pump becomes much larger than that of the two FWM sidebands when the detuning is further decreased (state (v)).

Although the behavior in Fig. 4.12 is different from Fig. 4.8, it could be explained by using the same model. The critical parameter for this behavior was not a higher mechanical Q but the dispersion and mode number for the first comb sidebands. Here a Turing pattern comb formed again after the generation of sub-comb lines, that was often observed in our experiment. Although this formation has not been well understood, the author thinks it is due to the influence of cavity optomechanics because sub-comb lines generated with optomechanical oscillations and a Turing pattern comb formed without the oscillations.

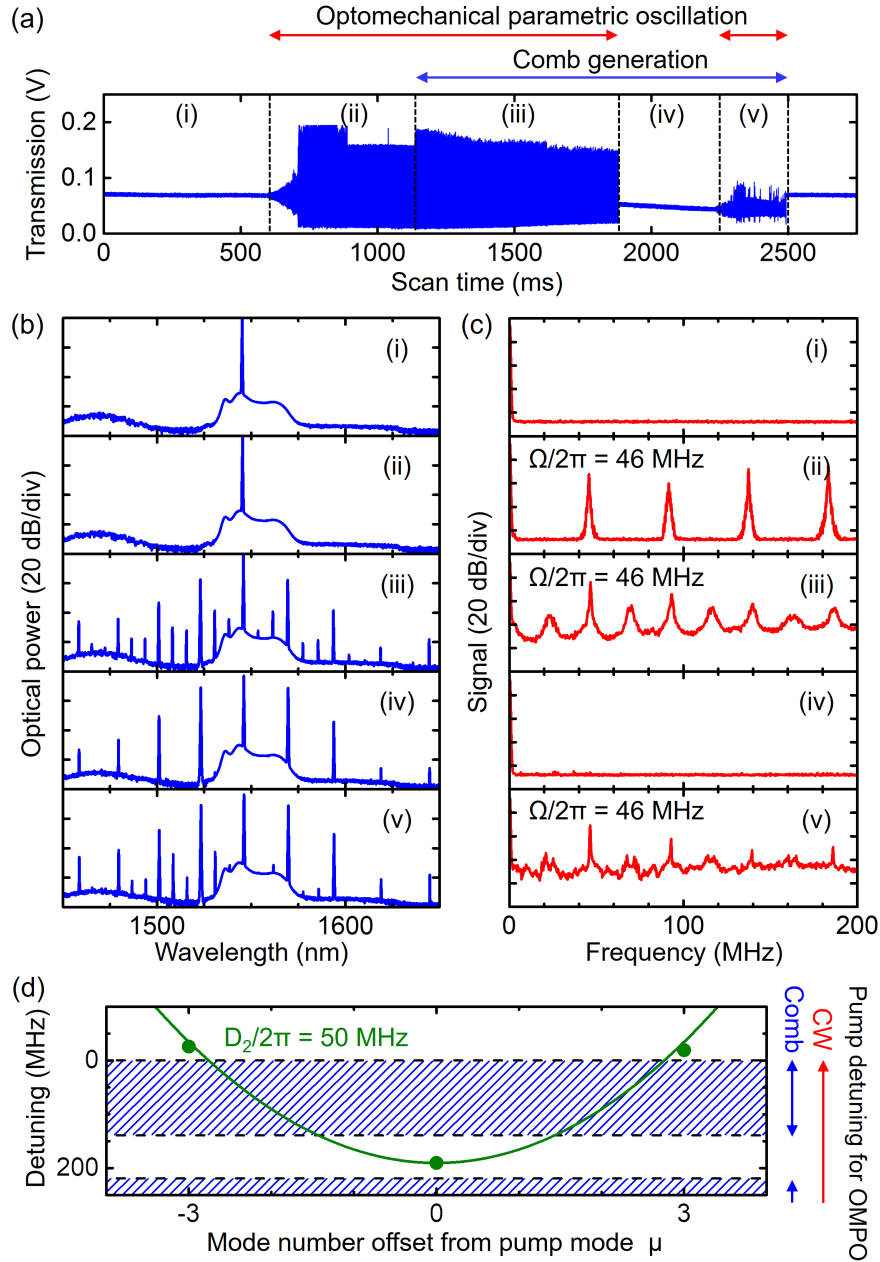


Fig. 4.12: (a) Transmission when scanning the pump laser with a different toroid microresonator of which parameter is given in Table 4.2. The power fluctuation was suppressed in state (iv). The pump power was 320 mW. (b) and (c) Typical measured optical spectra and RF signals in state (i)-(v). Although a 3-FSR Turing pattern comb was generated in state (iv), small sub-comb lines were observed in state (iii) and (v) with RF signals induced by the OMPO. (d) The green points represent measured detuning values from each resonance frequency when generating a 3-FSR Turing pattern comb, which follow the microresonator dispersion (green curve). In the condition for generating the comb shown in state (iv), whose pump detuning was 191 MHz, the calculated pump detuning for $\Gamma_{\text{eff}} > 0$ was from 139 to 219 MHz in the blue-detuned side.

4.5 Temporal behavior of transmission power with high pump power

In the previous research [81], the model to calculate temporal behavior of transmission in optomechanical oscillations was based on a coupled mode equation with a motion equation. This model did not take account of Kerr effects. However, with high pump power, the resonance shift that is caused by the Kerr effect cannot be ignored because the Kerr effect response is faster than the optomechanical oscillation frequency. Here I added the Kerr effect term to the model and compared the calculation with experimental results.

The motion equation for the displacement in the radial direction $x(t)$ is given by Eq. (4.3). The internal field $a_0(t)$ can be expressed with the displacement and Kerr effect as

$$\frac{da_0(t)}{dt} = -\frac{\kappa}{2}a_0(t) + i \left\{ \omega_p - \omega_0 \left(1 - \frac{x(t)}{R} - \frac{\Delta n_{\text{Kerr}}(t)}{n} \right) \right\} a_0(t) + \sqrt{\kappa_c} s_{\text{in}}, \quad (4.31)$$

where $\Delta n_{\text{Kerr}}(t)$ is the refractive index change caused by Kerr effects, which follows Eq. (2.35). Note that this calculation model does not include thermal effects because the response time of thermal effects is much slower than those of optomechanical oscillations and Kerr effects. Figure 4.13 shows the experimental and calculated results. This experiment was performed under the same conditions as those used in Fig. 4.8 except that $Q_c = 2.3 \times 10^6$. In addition, the pump was applied at a power (200 and 240 mW) that is slightly smaller than the threshold power for FWM. The calculated and experimental results are in good agreement, which indicates that the Kerr effect strongly influences the resonance shift during optomechanical oscillation. This model can explain the transmission power shape even when the pump power is high.

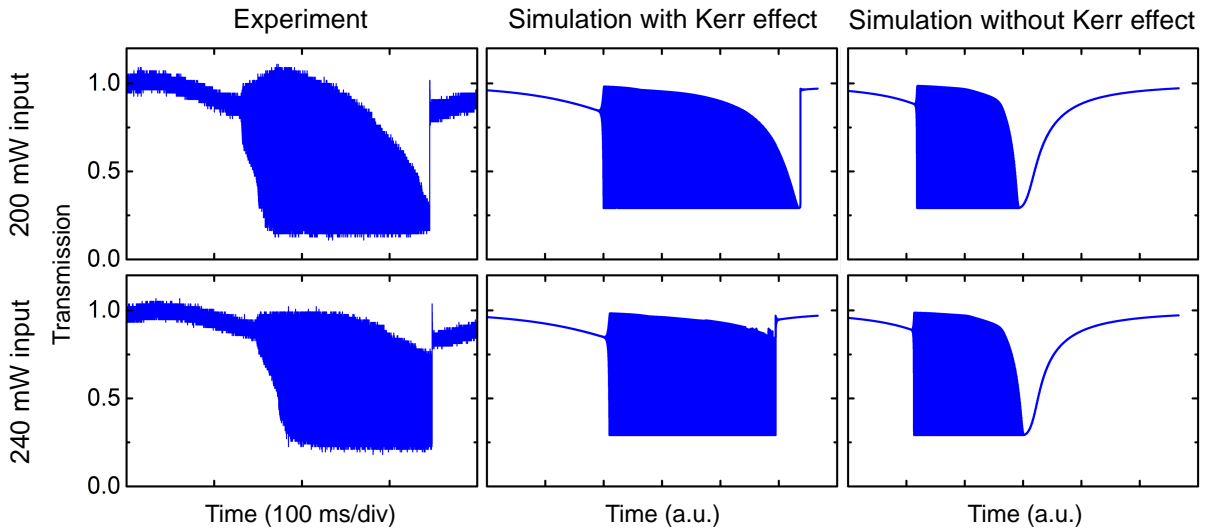


Fig. 4.13: Measured and calculated transmission with pump powers of 200 and 240 mW. The calculated and experimental results agree well because the fast Kerr effect is taken into account.

4.6 Summary

The author demonstrated the suppression of OMPOs with a Turing pattern comb, which was generated by a blue-detuned pump from the resonance frequency. When only the influence of the blue-detuned pump light is considered, optomechanical oscillations are always amplified. On the other hand, the suppression of OMPO with a Turing pattern comb can be explained and achieved by assisting the influence of all the comb lines, which are in the red-detuning regime. In addition, this study provides a guideline of designing microresonator properties by using the LLE and equation for calculating effective damping rate. To control the properties of cavity dispersion and also threshold power for degenerate FWM (related to an optical Q factor) enables OMPO suppression and microcomb generation that has low phase noise in optomechanical coupling systems. In addition, on the basis of this study, it is considered that soliton microcombs will achieve efficient damping because the pump and comb lines are both in the red-detuned regime.

Chapter 5

Broadband gain induced Raman comb formation in a silica microresonator

5.1 Introduction

5.1.1 Raman response function in silica

Stimulated Raman scattering (SRS) is an optical nonlinear process that can generate red-shifted light from pump light via the interaction between light and molecular vibrations. The temporal form of a Raman gain function and the Raman gain spectrum are determined by the vibration modes of the host material. Silica glass has thirteen vibration modes which result in a broad and complex Raman gain spectrum [126, 154]. A Raman gain spectrum corresponds to the imaginary part of the Fourier transform of the temporal form $h_R(\tilde{t})$. The approximate temporal form can be written as [126]

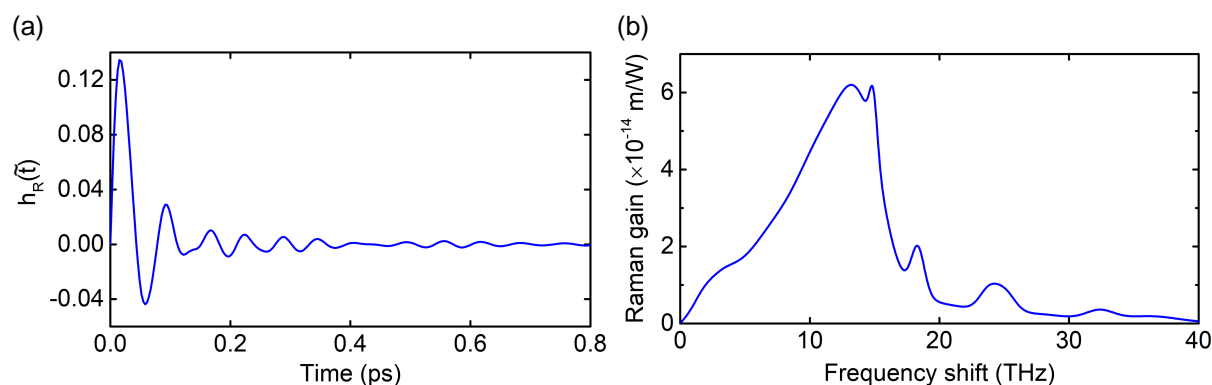


Fig. 5.1: (a) Temporal form of the Raman response function in silica. (b) Raman gain spectrum, which is obtained with the imaginary part of the Fourier transform of $h_R(\tilde{t})$, in silica at 1550 nm. The gain intensity is in inverse proportion to the wavelength.

$$h_R(\tilde{t}) = \left(\tau_1^{-2} + \tau_2^{-2} \right) \tau_1 \exp\left(-\frac{\tilde{t}}{\tau_2}\right) \sin\left(\frac{\tilde{t}}{\tau_1}\right), \quad (5.1)$$

where $\tau_1 = 12.2$ fs and $\tau_2 = 32$ fs. However, in this thesis, I use a more exact description of the Raman response function by following Ref. [154], whose results are shown in Fig. 5.1. Owing to the complex Raman gain spectrum in silica, the generated Raman comb usually exhibit complex spectrum shape and is unstable.

5.1.2 Motivation

Here the author studied the detailed dynamics of Raman comb formation in silica rod microresonators, which have cavity FSRs in microwave rates. The author particularly focused on the frequency shift within the Raman gain having two large peaks at 13.2 THz (Peak 1) and 14.7 THz (Peak 2). Silica microresonators with a small cavity FSR (large diameter) were used for this study because a large number of resonant modes is present within the Raman gain spectrum. In our experiment, the author excited one of the specific peaks and tried to generate a Raman comb with a smooth spectrum envelope by controlling the pump detuning and the coupling strength. In addition, good understanding on the Raman comb formation is even important for comb generation via FWM because these processes compete inside a microresonator [90, 101, 102, 104–106, 155]. The generation scheme with SRS is different from that with FWM.

5.2 Raman comb generation in a silica rod microresonator

Figure 5.2(a) shows our experimental setup. A CW laser light with 100 kHz linewidth was amplified and then coupled to a silica rod microresonator by using a tapered fiber. The coupling strength was adjusted by changing the fiber position. Silica rod microresonators with an intrinsic Q (Q_i) over 100 million were fabricated by using CO_2 laser processes [116, 156]. I used a microresonator having a diameter of 3.6 mm, which corresponds to a cavity FSR of 18.2 GHz, to study Raman comb formation in microwave rate. The pump light was scanned from a short to a long wavelength to generate the Raman comb, because the resonance was shifted via thermal effects [120]. The output light was monitored with an optical spectrum analyzer. In addition, the Raman comb was to measure its beatnote signal by using a 20 GHz photodetector connected to an electrical spectrum analyzer.

Figure 5.3 shows output power of pump (blue) and Raman (green) light from the silica rod microresonator while scanning the pump frequency. As shown with the black dashed line and green shadowed area, the Raman comb started to generate when the pump laser was sufficiently coupled to the resonance. Figure 5.2(b) shows the measured optical spectra while generating a Raman comb with under coupling condition. The pump energy at 1540 nm was transferred to longer wavelength components around 1665 nm via SRS. The red line shows the theoretical Raman gain spectrum when the the pump is located at 1540 nm. With 1540.0 nm pumping, the two peaks, Peak 1 (13.2 THz shift) and 2 (14.7 THz shift), locates at wavelength of 1651.9 and

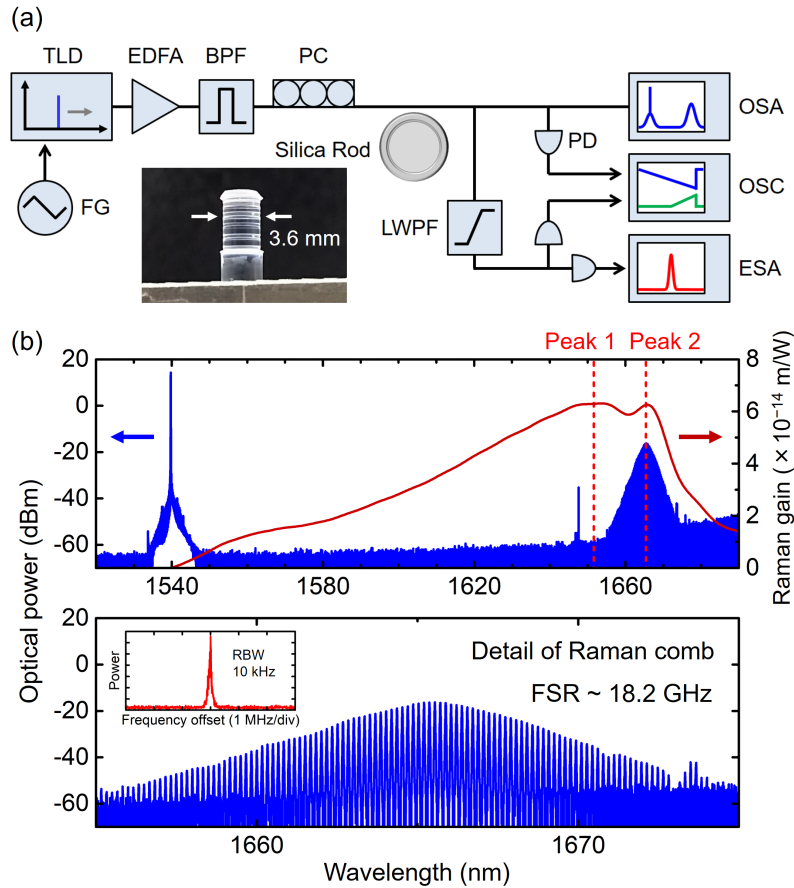


Fig. 5.2: (a) Experimental setup for Raman comb generation. TLD: tunable laser diode, FG: electrical function generator, EDFA: erbium-doped fiber amplifier, BPF: bandpass filter, PC: polarization controller, LWPF: longwave-pass filter, PD: photodetector, OSA: optical spectrum analyzer, OSC: oscilloscope, ESA: electrical spectrum analyzer. The inset shows a silica rod microresonator with a cavity FSR of 18.2 GHz. (b) Optical spectra (blue) and a theoretical Raman gain pumped at 1540 nm (red). Raman gain has two large peaks with frequency shifts of 13.2 THz (Peak 1) and 14.7 THz (Peak 2). The pump frequency does not affect the amount of frequency shift but affects the gain intensity (proportional to the pump frequency). The generated Raman comb had a smooth spectral envelope whose center wavelength corresponded to Peak 2. The inset shows the beatnote signal measured by detecting the generated Raman comb. The 3 dB linewidth is less than hundreds of kHz.

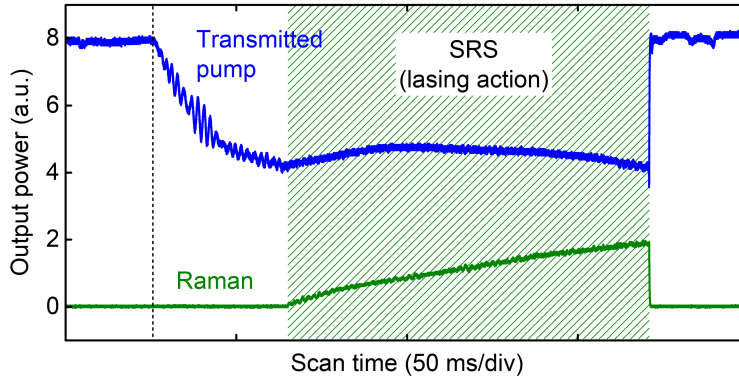


Fig. 5.3: Output power of pump (blue) and Raman (green) light from the silica rod microresonator while scanning the pump frequency. The green shadowed area represents the Raman lasing region.

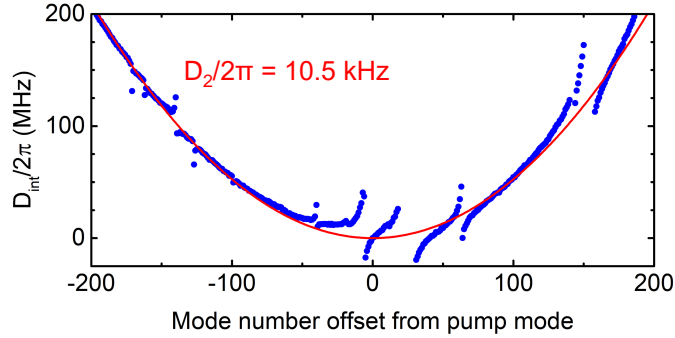


Fig. 5.4: Measured dispersion of the transverse mode (blue points) used for Raman comb generation and a parabolic fitting using a $D_2/2\pi$ value of 10.5 kHz (red curve). Mode couplings between other transverse modes are observed around the pump mode.

1665.7 nm, respectively. Due to the complex shape of the Raman gain spectrum, a Raman comb with an asymmetric spectrum shape is usually excited when parameters such as the excitation power and the coupling condition between the microresonator and fiber are not adjusted. Only when I carefully adjust the parameters, a Raman comb with a smooth envelope as shown in Fig. 5.2(b) was obtained. In this experiment, higher order cascaded SRS was hardly observed.

With a silica microresonator having anomalous dispersion, the competition between SRS and FWM thresholds is given as $P_{in}^{SRS}/P_{in}^{FWM} \approx (2\omega_0 n_2)/(c g_{R(max)}) \approx 2.9$, which implies that the FWM occurs before generating SRS [85, 141]. ω_0 is the pump frequency, n_2 is the nonlinear refractive index of silica, c is the speed of light, and $g_{R(max)}$ is the maximum Raman gain of silica in units of m/W. However, in our experiment, typical degenerate FWM through modulation instability did not occur while changing the detuning. Since FWM generation depends on the cavity dispersion, I measured the dispersion of the transverse mode used for Raman comb generation. The result is shown in Fig. 5.4, where the blue points represents the measurement data and the red curve represents a parabolic fitting using a $D_2/2\pi$ value of 10.5 kHz. It is assumed that the mode couplings with other transverse modes, which are observed around the

pump mode shown in Fig. 5.4, makes effectively normal dispersion around the pump mode and increases the threshold for FWM. The normal dispersion at pump frequency was caused by the mode couplings in this experiment. Also, the normal dispersion condition can also be achieved by applying the lower pump frequency because many types of microresonators become normal dispersion at lower frequency side (e.g. visible wavelength).

In order to examine the coherent property of the output light, I measured the beatnote signals with a fast photodetector. It can be directly measured because the generated Raman comb has mode spacings in microwave rates. The measured beatnote signals exhibit multiple peaks when the output is not a smooth spectrum, because Raman light is generated in various transverse modes. On the other hand, when a Raman comb with a smooth spectrum envelope is obtained, it has only one peak with 3 dB linewidth of less than hundreds kHz as shown in the inset of Fig. 5.2(b). The linewidth is limited by the presence of the dispersion, because each SRS lines locate as the center of each resonance modes. This experimental result provides a potential to obtain smooth and phase-locked Raman combs through optimizing the operation wavelength, cavity dispersion, and stabilization techniques. In particular, according to the previous reports [71, 106], pumping at the weak normal dispersion regime is suitable to generate phase-locked Raman combs.

5.3 Peak transition via controlling detuning and coupling

First, I investigated the transition of the Raman comb position between two peaks, Peak 1 and 2, within Raman gain spectrum. Figure 5.5 shows spectrum formation via SRS while decreasing the detuning between resonance and pump frequencies. The pump light with large detuning generated SRS close at Peak 1 wavelength. The difference between the center wavelength and Peak 1 is due to the broad gain of Peak 1. Decreasing the detuning caused SRS at longer wavelength regime, whose offset from pump matched to Peak 2. By further decreasing the detuning, the energy transfer from Peak 1 to Peak 2 and suppression of the Raman light at Peak 1 were observed. The Raman energy transition was also observed with another silica rod microresonator which has a cavity FSR of 32.4 GHz. Hence, by controlling the detuning, a Raman comb with the offset wavelength at Peak 1 or Peak 2 can be generated. Such behavior was also observed in silica fibers when the input power is changed [83]. Although the detail explanation is given in §5.4, it is briefly explained as follows. Since the gain at Peak 1 is slightly higher than that of Peak 2, Peak 1 reaches SRS threshold at first. As Peak 2 is excited directly from the pump and light generated at Peak 1, it then reaches the lasing threshold as the pump power is further increased.

Longer wavelength modes are excited from modes at shorter wavelength, because each mode exhibits Raman gain having the value from zero frequency shift. That also induces the center wavelength of a Raman comb is shifted by oneself via SRS. Figure 5.6(a) shows the center wavelength (red) and 3 dB bandwidth (blue) of a Raman comb as a function of the pump wavelength. The amount of the center wavelength shift was much larger than that of pump scanning, whose ratio is about 37. Figure 5.6(b) shows Raman comb spectra with different pump wavelengths, that indicates the comb envelope broadens to longer wavelength. The center

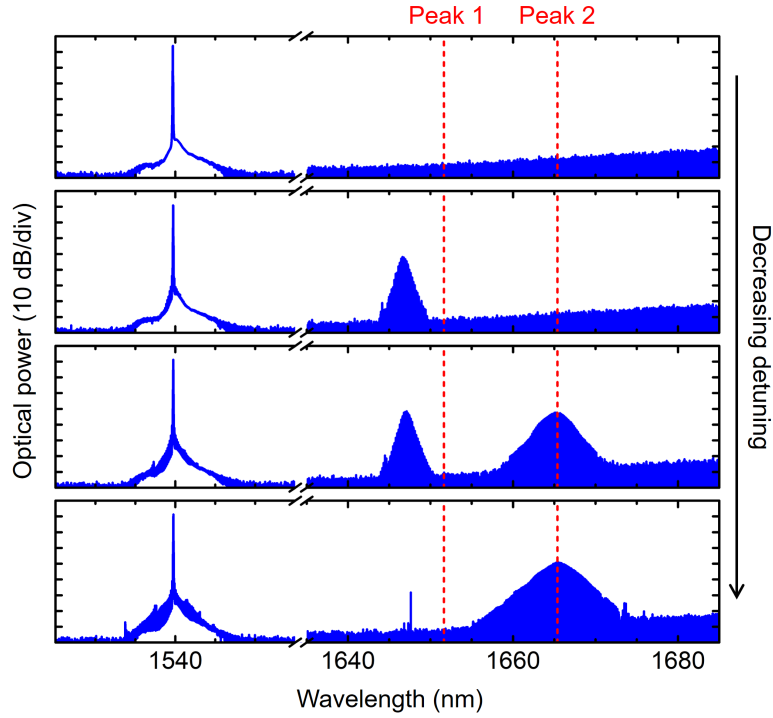


Fig. 5.5: Raman comb formation while decreasing the detuning between pump and resonance frequencies. The Raman offset transited from Peak 1 to Peak 2. The pump wavelength and input power were 1540 nm and 80 mW, respectively.

wavelength shift of a mode-locked soliton pulse (corresponding to pulse delay in time domain) has been observed in optical fibers [157] and microresonators [102]. Since the generated Raman comb in this experiment did not propagate as a soliton pulse, the ratio of the center wavelength shift was small.

Next, I investigated the coupling strength dependency. I controlled the coupling strength by changing the tapered fiber position and measured comb spectra with near zero pump detuning (Fig. 5.7). The coupling strength is defined as $\eta = \kappa_c / \kappa$ ($\eta = 0.5$ denotes critical coupling). κ and κ_c are the cavity decay rate and the coupling rate to the waveguide, respectively. κ has the relation as $Q = \omega_0 / \kappa$ and $\kappa = \kappa_i + \kappa_c$. Q is the cavity Q and κ_i is the intrinsic loss rate. Figure 5.7 shows that a weak coupling induced to generate a Raman comb at Peak 2, while strong coupling results the excitation of Peak 1. The values of coupling strength are obtained from linewidth of the measured cavity resonances.

5.3. Peak transition via controlling detuning and coupling

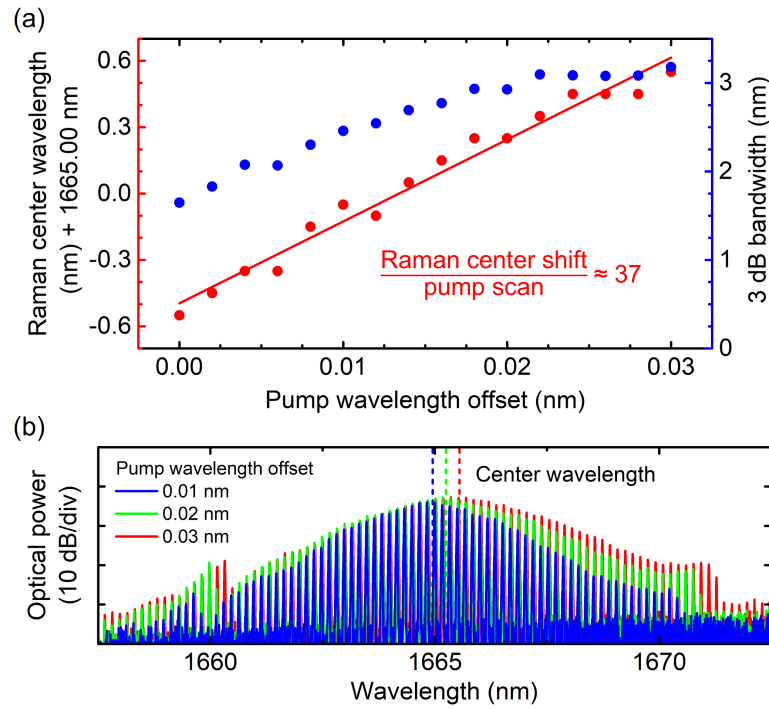


Fig. 5.6: (a) The center wavelength (red) and 3 dB bandwidth (blue) in a Raman comb generated at Peak 2 as a function of the pump wavelength. (b) Raman comb spectra with different pump wavelengths (detuning). The dashed lines represent the center wavelength of each comb envelope.

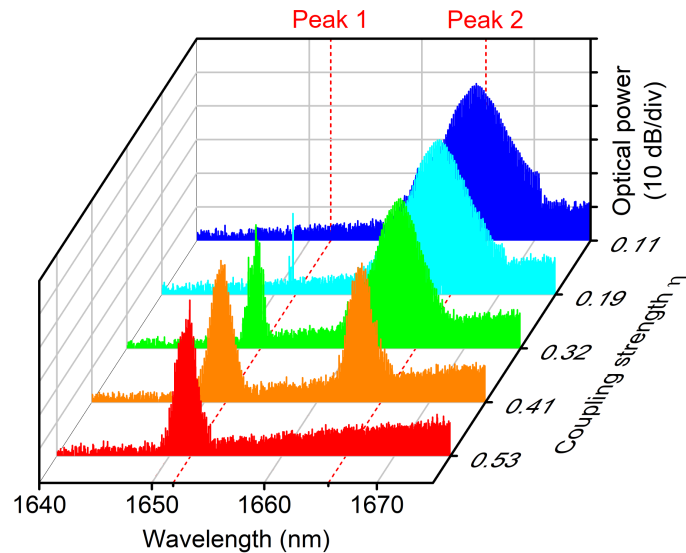


Fig. 5.7: Raman comb spectra depending on the coupling strength (fiber position) with near zero pump detuning. A weaker (stronger) coupling condition induced the generation of a Raman comb at Peak 2 (Peak 1). The pump wavelength and input power were 1540 nm and 160 mW, respectively.

5.4 Coupled mode equations with Raman processes

To study the energy exchange between the pump and other resonant modes covered by Raman gain, I calculated numbers of intracavity photons by using coupled mode equations taking Raman processes into account. This calculation is used to obtain the dynamics of energy exchange via SRS, as functions of coupling strength and detuning between pump and resonant frequencies. The internal field in each mode a_m ($m = 0, 1, 2, \dots$) has the resonance frequency as $\omega_m = \omega_0 - mD_1$, where ω_0 is the pump frequency and D_1 is the cavity FSR in units of rad·Hz. The time evolution of these fields is given by

$$\frac{\partial a_m}{\partial t} = -\frac{1}{2}\kappa a_m + \sum_{m', 0 \leq m' < m} G_{R(m', m)} |a_{m'}|^2 a_m \quad (5.2)$$

$$- \sum_{m', m < m'} G_{R(m, m')} |a_{m'}|^2 a_m \left[+i\Delta\omega_0 a_m + \sqrt{\kappa_c} s_{\text{in}} \right]_{m=0}. \quad (5.3)$$

Here s_{in} is the input field as $|s_{\text{in}}|^2 = P_{\text{in}}/(\hbar\omega_0)$, P_{in} is the input power to the coupling waveguide, \hbar is the Planck constant divided by 2π , and $\Delta\omega_0$ represents the pump detuning from the resonance. The input field is only added to the equation for pump mode ($m = 0$). The number of intracavity photons in each mode corresponds to $|a_m|^2$, which can be converted to power by $\hbar\omega_m |a_m|^2 \times D_1/2\pi$. The nonlinear Raman coefficient is written as

$$G_{R(j, k)} = g_R(\omega_j, \omega_k) \frac{cD_1 \hbar \omega_j}{4\pi n A_{\text{eff}}}, \quad (5.4)$$

where j and k represent the mode numbers ($j, k \in 0, 1, 2, \dots$), n is the effective refractive index of the resonance mode, and A_{eff} is the effective nonlinear mode area. $g_R(\omega_j, \omega_k)$ represents the Raman gain in silica with the frequency shift $\omega_k - \omega_j$ when pumping at the frequency ω_j . With 1550 nm pumping to silica, the Raman gain value is 6.2×10^{-14} m/W at 13.2 THz shift [126, 154]. The gain value is in proportional to the pump frequency. κ , κ_c , κ_i , and A_{eff} are regarded as independent of the mode number m .

Figure 5.8 shows the lasing action at different coupling conditions as function of the detuning that is normalized by κ . The calculation parameters are shown in Table 5.1, which follow our experimental condition. A_{eff} is calculated by using a mode solver based on finite element method. I set the number of modes to 1001, which corresponds to the wavelength range from 1540 to 1698.8 nm. With larger detuning, SRS does not occur because the intracavity power is below the threshold. After exceeding the threshold, red-shifted light starts to appear close at Peak 1 in Raman gain (1651.9 nm). This is because the gain value at Peak 1 is larger than that at Peak 2. When the detuning is even smaller, the SRS wavelength changes to close at the Peak 2 (1665.7 nm) due to the simultaneous excitation by two components; i.e. by pump and Raman

Table 5.1: Parameters used for the calculation

λ_0	P_{in}	$D_1/2\pi$	Q_i	n	A_{eff}
1540 nm	160 mW	18.2 GHz	1×10^8	1.44	$135 \mu\text{m}^2$

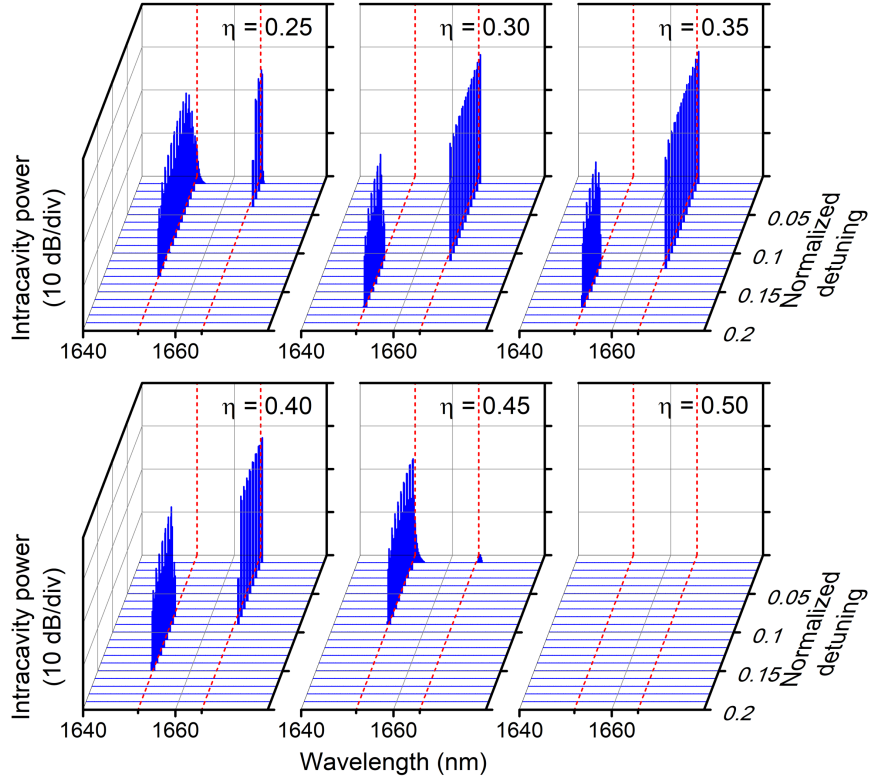


Fig. 5.8: Transition of SRS wavelength, calculated by using Eq. (5.3). The pump wavelength is 1540.0 nm (not shown in this figure). Peaks 1 and 2 of the Raman gain correspond to 1651.9 and 1665.7 nm, respectively (red lines). A clear SRS wavelength transition is observed at a coupling strength (η) of 0.30-0.40. On the other hand, SRS does not occur due to the relatively low effective Q at a critical coupling condition ($\eta = 0.5$) with the parameters shown in Table 5.1.

light at Peak 1. The calculation shows clear transition of the SRS light from one wavelength to another, depending on the detuning.

In addition, the peak transition is dependent on the coupling strength. When the coupling strength is weak, it generates SRS at peak 2. When the coupling strength is even weaker, the system does not exhibit SRS because the intracavity pump power does not reach the threshold. On the other hand, the critical coupling condition does not allow us to achieve SRS due to the relatively low effective Q . According to this calculation, it is founded that the SRS is efficient when $\eta = 0.35$. The calculation results show that the smaller detuning and weaker coupling strength are needed to generate SRS efficiently, and the result in agreement with our experimental observations shown in Figs. 5.5 and 5.7. Although weak FWM comb lines (i.e. close at the pump light) were observed in our experiment as shown in Fig. 5.5, it does not influence the result very much because the unequal spacings of the SRS comb lines do not strongly interact with FWM combs. Therefore our model where no FWM processes are taken into account is sufficient to describe the phenomena. Our numerical analysis focuses on specifying the center of excited modes.

Some differences between the experiment and the numerical analysis are observed. We

observed multi-mode lasing in the experiment, while the system exhibits lasing at a few modes in our numerical analysis even though thirteen vibration frequencies are taken into account. This is because the pump intensity is clamped after the SRS occurs and also all SRS modes share the same pump mode. In the experiment, however, each molecule exhibits different vibration frequencies, which is the origin of inhomogeneous broadening of the Raman gain [154]. Hence I obtained multi-mode Raman lasing in the experiment. Despite this difference, the energy transition behavior from Peak 1 to Peak 2 is explained by using our model.

5.5 Summary

This study provides how to control the operation wavelength and formation of a Raman comb through pump detuning and coupling strength. The author generated Raman combs from a silica rod microresonator with a FSR in microwave rate and controlled the center wavelength via detuning and coupling optimizations. In the experiment, decreasing detuning leads to the Raman energy transition from Peak 1 to Peak 2, which is a similar behavior that has been observed in silica fibers. Also, weak coupling induced to generate a Raman comb at Peak 2, while strong coupling results the only excitation of Peak 1. Those observations are in agreement with simulation, which are calculated by using coupled mode equations taking account of Raman processes. In addition, the center wavelength shift of a Raman comb was observed, with a shift that is 37 times larger than that of pump scanning. The combination of this study and previous researches on phase-locking scheme [71, 94, 106] will enable generation of Raman combs that have a smooth spectral envelope and mutual coherence between the comb lines.

Chapter 6

Theoretical study on dual-comb generation and soliton trapping in a single microresonator with orthogonally polarized dual-pumping

6.1 Introduction

6.1.1 Dual-comb generation scheme from a single resonator

There are certain approaches for generating a dual-comb in a microresonator system. One approach is to use two different microresonators that generate microcombs individually [55, 57, 61, 107]. The disadvantage of this commonly used method is to require precise fabrication processes with which to control the cavity FSRs, which are determined by the microresonator size. Although nano- and microfabrication technologies have the potential to enable us to fabricate microresonators whose cavity FSR is controlled (e.g. silicon nitride ring and silica disk microresonators), polishing and laser processing cannot control the parameters precisely (e.g. polished magnesium fluoride and laser processed silica microresonators). Another approach is to pump one transverse mode from clockwise and counter-clockwise directions [60, 90, 158] or two different transverse modes (also known as mode families) [108–112] in a single microresonator. In this system, both combs share the same resonator (common mechanical vibrations and thermal fluctuations) and also the feedback loops, which leads to mutual coherence between the combs. Such dual-comb generation in a single resonator has also been studied with other platforms such as mode-locked integrated external-cavity surface-emitting lasers (MIXSELS) [159].

Pumping one transverse mode from clockwise and counter-clockwise directions requires only one pump laser, which is modulated with an electro- or acousto-optic modulator. This is because the pump frequencies in the two directions are almost the same. This system can provide simple control of the pump frequencies. On the other hand, the difference between the repetition frequencies is only achieved to a small degree, which depends on cross-phase modulation (XPM) effects. A previous study that used this method reported soliton trapping inside a microresonator

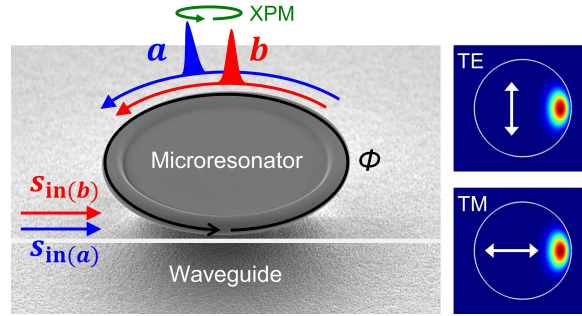


Fig. 6.1: Illustration of a simulation model with orthogonally polarized dual-pumping (left) and examples of mode intensity profiles in the TE and TM modes (right). Propagating solitons interact via XPM, which changes the group velocities.

between a Kerr soliton and a Raman soliton in different transverse modes, which are excited with a pump laser and Raman scattering, respectively [90].

When pumping two different transverse modes as illustrated in Fig. 6.1, complex control of the pump frequencies is typically required because two individual lasers are used to pump the resonance modes, which, in most cases, are located separately in the frequency domain. However, a large difference can be achieved between the repetition frequencies by controlling the pump frequencies and cavity dispersion of the pumped resonance modes. Also, cavity size and dispersion engineering can control the resonance frequencies whose separation is at microwave levels (below tens of gigahertz). The different transverse modes can be pumped by using a single laser with an electro-optic modulation.

6.1.2 Motivation

Here, the author theoretically studies dual-comb generation in a single microresonator by using coupled Lugiato-Lefever equations (LLEs), and the author focuses particularly on soliton trapping. The conditions for dual-comb solitons generation and soliton trapping are investigated with numerical simulation and analysis approaches. Soliton trapping is a phenomenon that can be observed in optical fibers when inputting two optical pulses with slightly different group velocities to compensate for the group velocity mismatch via XPM [126, 160–164]. In our calculation model, a dual-comb is considered to be excited with orthogonally polarized dual-pumping (TE and TM modes). Such a system has advantages for generating a dual-comb with a controlled difference between the repetition frequencies in a single microresonator, which is fabricated by cutting, polishing, and laser processing [116, 165, 166]. This is because orthogonally polarized transverse modes have almost same cavity FSRs owing to the resemble mode profiles. However, dual-comb solitons with orthogonal polarizations have yet to be demonstrated experimentally (non-soliton dual-comb generation has been reported [108–110]). Hence revealing the conditions is helpful for optimizing the experimental parameters for dual-comb systems. In other words, soliton trapping should be avoided for dual-comb applications because the difference between the repetition frequencies is compensated to zero. On the other hand, the observation of soliton trapping inside a microresonator is an attractive topic in fundamental science.

6.2 Simulation model

Microcomb formation has been studied using an LLE [90, 135, 139]. To calculate multiple microcomb formation, two LLEs are coupled and developed by taking XPM and the difference between repetition frequencies into account. The time evolution of the internal fields a and b , which have orthogonal polarizations (TE and TM modes), are represented with coupled LLEs as

$$\frac{\partial a(\phi, t)}{\partial t} = -\frac{\kappa(a)}{2}a + i\Delta\omega_{0(a)}a + i\frac{D_{2(a)}}{2}\frac{\partial^2 a}{\partial \phi^2} + ig_{(a)}(|a|^2 + \sigma|b|^2)a + \sqrt{\kappa_{c(a)}}s_{in(a)} + \frac{\Delta D_1}{2}\frac{\partial a}{\partial \phi} \quad (6.1)$$

$$\frac{\partial b(\phi, t)}{\partial t} = -\frac{\kappa(b)}{2}b + i\Delta\omega_{0(b)}b + i\frac{D_{2(b)}}{2}\frac{\partial^2 b}{\partial \phi^2} + ig_{(b)}(|b|^2 + \sigma|a|^2)b + \sqrt{\kappa_{c(b)}}s_{in(b)} - \frac{\Delta D_1}{2}\frac{\partial b}{\partial \phi} \quad (6.2)$$

where t is the slow time and ϕ is the azimuthal angular coordinate inside the microresonator being related to the fast time. $\kappa_{(*)}$, $\kappa_{i(*)}$, and $\kappa_{c(*)}$ are the cavity decay, intrinsic decay, and coupling rates, respectively. They are related as follows $\kappa_{(*)} = \kappa_{i(*)} + \kappa_{c(*)}$. Here $(*)$ represents (a) or (b) . $\Delta\omega_{0(*)}$ is the detuning between the pump and resonance frequencies as $\Delta\omega_{0(*)} = \omega_{p(*)} - \omega_{0(*)}$, where $\omega_{p(*)}$ and $\omega_{0(*)}$ are the pump and resonance frequencies, respectively. The resonance frequencies in one transverse mode follow a Taylor expanded equation as $\omega_{\mu(*)} = \omega_{0(*)} + D_{1(*)}\mu + (1/2)D_{2(*)}\mu^2 + \dots$, where μ is the mode number offset from the pump mode, $D_{1(*)}$ is the cavity FSR, and $D_{2(*)}$ is the second order dispersion. The higher order terms are neglected. $g_{(*)}$ is the nonlinear coefficient as $g_{(*)} = (\hbar\omega_{0(*)}^2 n_2 D_{1(*)}) / (2\pi n^2 A_{eff(*)})$, where \hbar is the reduced Planck constant, n_2 is the nonlinear refractive index, n is the refractive index, and $A_{eff(*)}$ is the effective mode area. σ is the XPM coefficient ($\sigma = 2/3$ for orthogonal polarizations), $s_{in(*)}$ is the input field as $s_{in(*)} = \sqrt{P_{(*)}/\hbar\omega_{0(*)}}$, $P_{(*)}$ is the input power, and $\Delta D_1 = D_{1(b)} - D_{1(a)}$.

Here, I calculate generalized coupled LLEs:

$$\frac{\partial u(\phi, \tau)}{\partial \tau} = -(1 + i\alpha_{(u)})u + i\beta_{(u)}\frac{\partial^2 u}{\partial \phi^2} + i(|u|^2 + \sigma|v|^2)u + F_{(u)} + \gamma\frac{\partial u}{\partial \phi}, \quad (6.3)$$

$$\frac{\partial v(\phi, \tau)}{\partial \tau} = -(1 + i\alpha_{(v)})v + i\beta_{(v)}\frac{\partial^2 v}{\partial \phi^2} + i(|v|^2 + \sigma|u|^2)v + F_{(v)} - \gamma\frac{\partial v}{\partial \phi}, \quad (6.4)$$

where it is assumed that $\kappa = \kappa_{(a)} = \kappa_{(b)}$ and $g = g_{(a)} = g_{(b)}$. The parameters follow $\tau = \kappa t/2$, $u = a\sqrt{2g/\kappa}$, $v = b\sqrt{2g/\kappa}$, $\alpha_{(**)} = -2\Delta\omega_{0(*)}/\kappa$, $\beta_{(**)} = D_{2(*)}/\kappa$, $\gamma = \Delta D_1/\kappa$, and $F_{(**)} = (2s_{in(*)}/\kappa)\sqrt{2g\kappa_{c(*)}/\kappa}$, where $\{(*), (**)\}$ represents $\{(a), (u)\}$ or $\{(b), (v)\}$. Here, when the parameters are set at $\sigma = 0$ and $\Delta D_1 = 0$, Eqs. (6.1)-(6.4) are regarded as a basic LLE, which does not take account of the interaction between each equation (i.e. without XPM effects between orthogonally polarized internal fields). In addition, I define and use a parameter $\delta = \gamma/\sqrt{2\beta}$, when assuming $\beta = \beta_{(u)} = \beta_{(v)}$. Here this model does not consider the influence of linear mode coupling between the TE and TM modes, which should be considered when different resonance modes are located near in the frequency domain [167].

6.3 Numerical simulation results

Figure 6.2 shows the time evolution of microcomb spectra and waveforms for two orthogonally polarized transverse modes when the α value is changed from negative to positive. The parameters are $\alpha = \alpha_{(u)} = \alpha_{(v)}$, $\beta_{(u)} = \beta_{(v)} = 0.01$, $\gamma = 0.3$, and $F_{(u)} = F_{(v)} = 4$. Since γ is a nonzero value, two solitons in each transverse mode propagate at different group velocities, which is shown at a τ of around 70-100 in Fig. 6.2(b). However, XPM compensates for the group velocity mismatch over τ of 100 shown by the white arrow regions, where the two solitons propagate at the same group velocity and they keep remain at the same position inside a microresonator each other. This phenomenon is known as soliton trapping. At the top of Fig. 6.2(b), an XPM induced trapped soliton is directly generated from the original soliton of an internal field u . On the other hand, at the bottom of Fig. 6.2(b), the trapped soliton is not directly generated from the original soliton of an internal field v (which is represented clearly around τ of 90). In our simulation, a trapped soliton is generated by one of the original solitons in the transverse mode, which also supports the generation of a trapped soliton in the other transverse mode. Although Fig. 6.3 shows the formation of a single trapped soliton, the soliton number is random as in the LLE simulation.

Figure 6.3 shows comb spectra and waveforms at a τ of 120 seen in Fig. 6.2. The XPM compensates mutually for the group velocities that cause the center frequencies of the comb envelopes to shift in opposite directions as shown in Fig. 6.3(a). The shift $\Delta\mu$ follows $\Delta\mu = \Delta\omega_c/D_1 = \pm\Delta D_1/(2D_2)$ for fields a (u) and b (v), respectively. Here $\Delta\omega_c$ is the amount of center frequency shift in units of rad·Hz. This theoretical value is in good agreement with our numerical simulation results. This frequency shift can be explained with change of the instantaneous frequency via XPM between the two solitons. Since the positions (related to the fast time axis) of trapped solitons are slightly different, the instantaneous frequencies of two solitons change to opposite sides which correspond to the frequency shift of spectral envelope.

To reveal the soliton trapping condition, I perform a numerical simulation with various parameters in δ and F where $F = F_{(u)} = F_{(v)}$ is assumed for simplicity. The mapping of the soliton trapping condition is shown in Fig. 6.4(a), where the yellow area denotes the observable soliton trapping conditions. The orthogonally polarized solitons with a large δ (i.e. large difference between repetition frequencies) cannot be trapped even when a large F is applied.

Next, to check the possibility of observing soliton trapping under realistic experimental conditions, I show one example of microresonator parameters for three spatially different transverse modes with two polarizations, whose D_1 and D_2 are calculated by using a finite elemental simulation and a Sellmeier equation. The microresonator structure is defined with the resonator diameter and the curvature radius of the cross section in the resonance part. I considered a silica rod microresonator in critical coupling with a diameter of 3.6 mm, a Q of 1×10^8 , $\sqrt{P_{(*)}/A_{\text{eff}(*)}} \approx 5 \times 10^4 \sqrt{\text{W}/\text{m}}$ (e.g. $P_{(u)} = P_{(v)} \approx 250 \text{ mW}$, $A_{\text{eff}(u)} \approx A_{\text{eff}(v)} \approx 100 \mu\text{m}^2$), and various curvature radiuses. In the six calculated transverse modes, $D_1/2\pi$ and $D_2/2\pi$ were around 18 GHz and 100 kHz, respectively ($D_2 > 0$ denotes anomalous dispersion). The colored symbols in Fig. 6.4(b) show the microresonator parameter δ as a function of the curvature radius, where $F \approx 4$ following the above parameters. The three colored symbols represent the parameters in spatially different transverse modes, whose mode intensity profiles are shown in

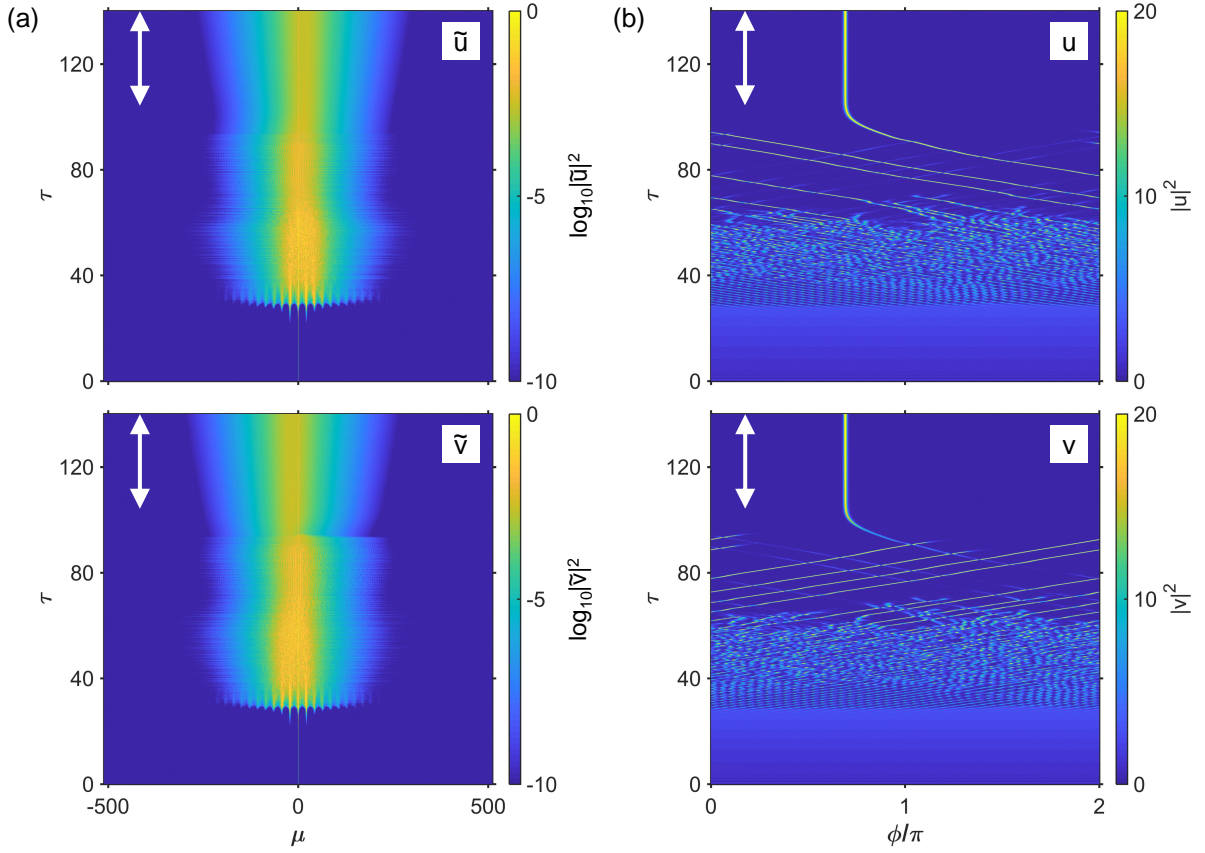


Fig. 6.2: Time evolution of microcomb (a) spectra and (b) waveforms in each transverse mode while changing α from a negative to a positive value. White arrows represent soliton trapping regions where two solitons are coupled via XPM and propagate at the same group velocity.

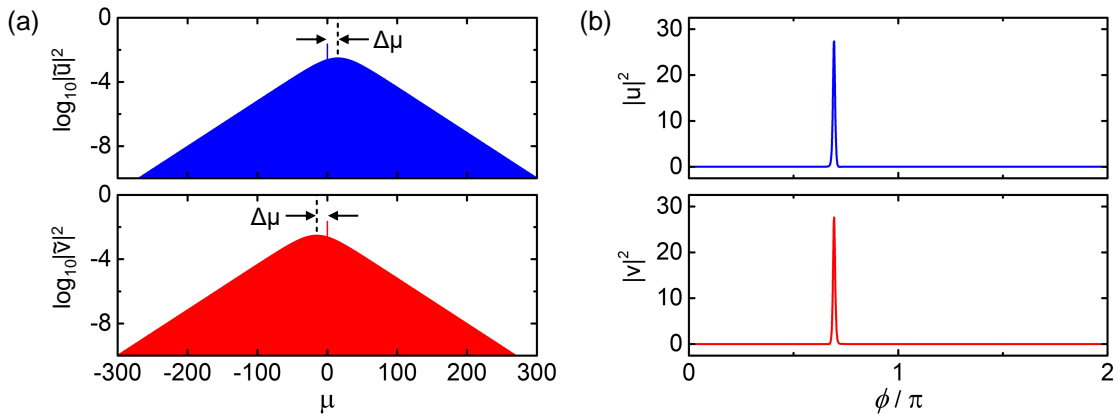


Fig. 6.3: Trapped soliton microcomb (a) spectra and (b) waveforms in each transverse mode at τ of 120 in Fig. 6.2. Soliton trapping is induced by XPM, which shifts the center frequencies of the comb envelopes and keeps the solitons at the same position inside the microresonator.

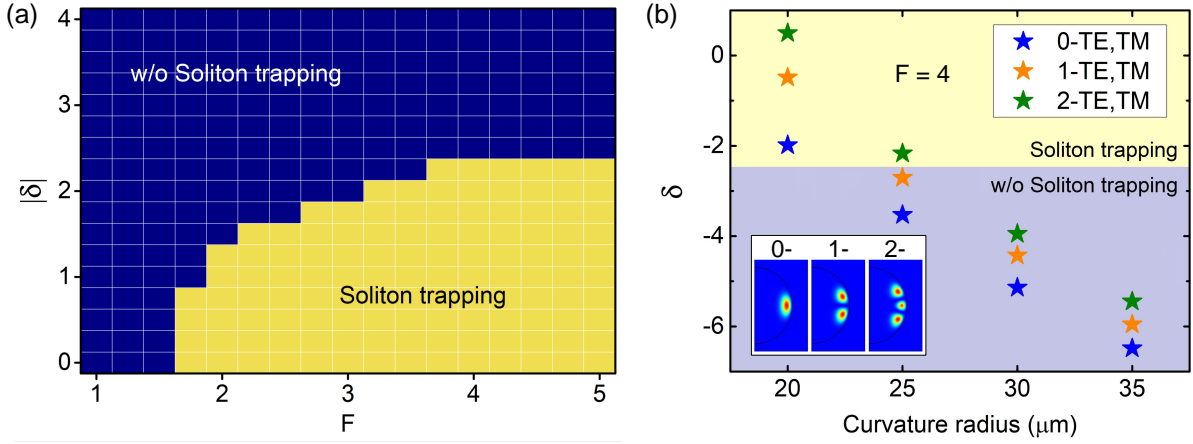


Fig. 6.4: (a) Numerical simulation results for soliton trapping conditions as functions of F and $|\delta|$, where the yellow area denotes conditions where trapping is observable. Here, $F_{(**)} = (2s_{in(*)}/\kappa)\sqrt{2g\kappa_{c(*)}/\kappa}$ and $\delta = \gamma/\sqrt{2\beta} = \Delta D_1/\sqrt{2D_2\kappa}$. (b) Three colored symbols represent the parameter δ , in spatially different transverse modes in silica microresonators, as a function of curvature radius. The background color represents the soliton trapping conditions being calculated with an F of 4, where the yellow area denotes conditions where soliton trapping is observable. The inset shows mode intensity profiles in a silica microresonator with a diameter of 3.6 mm and a curvature radius of 25 μm .

the inset (with a curvature radius of 25 μm). As represented in Fig. 6.4(b), soliton trapping can be observed with a curvature radius of 20 μm and also of 25 μm in some spatially different transverse modes. To observe soliton trapping in orthogonally polarized transverse modes, a small difference should be engineered in the cavity FSRs by fabricating symmetrical structure, where the resonance modes are located, for TE and TM polarizations. A smaller curvature radius is better for realizing a small difference between repetition frequencies. These results reveal the possibility of observing soliton trapping, where the solitons are excited by orthogonally polarized dual-pumping, under realistic experimental conditions. Although only one example is introduced here, the calculation in Fig. 6.4(b) can be applied to all platforms including silicon nitride ring, polished magnesium fluoride, and silica disk microresonators.

While the results in Figs. 6.2-6.4 are calculated with the parameters $\alpha_{(u)} = \alpha_{(v)}$, $\beta_{(u)} = \beta_{(v)}$, and $F_{(u)} = F_{(v)}$, I calculate microcomb formation with different $F_{(**)}$ values to focus on the phenomenon whereby a trapped soliton is generated by a strongly pumped soliton, which also supports the generation of a weakly pumped soliton in the other transverse mode, as seen in Fig. 6.2. Figure 6.5(a) shows the dimensionless intracavity powers $|u|^2$ (blue) and $|v|^2$ (red) while scanning $\alpha = \alpha_{(u)} = \alpha_{(v)}$. Other parameters are $\beta_{(u)} = \beta_{(v)} = 0.01$, $\gamma = 0.3$, $F_{(u)} = 4$, and $F_{(v)} = 3$. Figure 6.5(b) shows spectra (left) and waveforms (right) at α value of -2, 0, 5, 10, 16, and 21, which are represented with dashed black lines in Fig. 6.5(a). While α changes from 5 to 10, the internal field u forms a soliton state. Also, in the internal field v , the weak comb lines are generated via XPM by the soliton microcomb u at α value of 10, whose detailed waveform in the green dashed box is shown in Fig. 6.5(c). When changing α to a larger value that corresponds to increasing the soliton peak power of u , the power of the comb lines in the v increases and finally

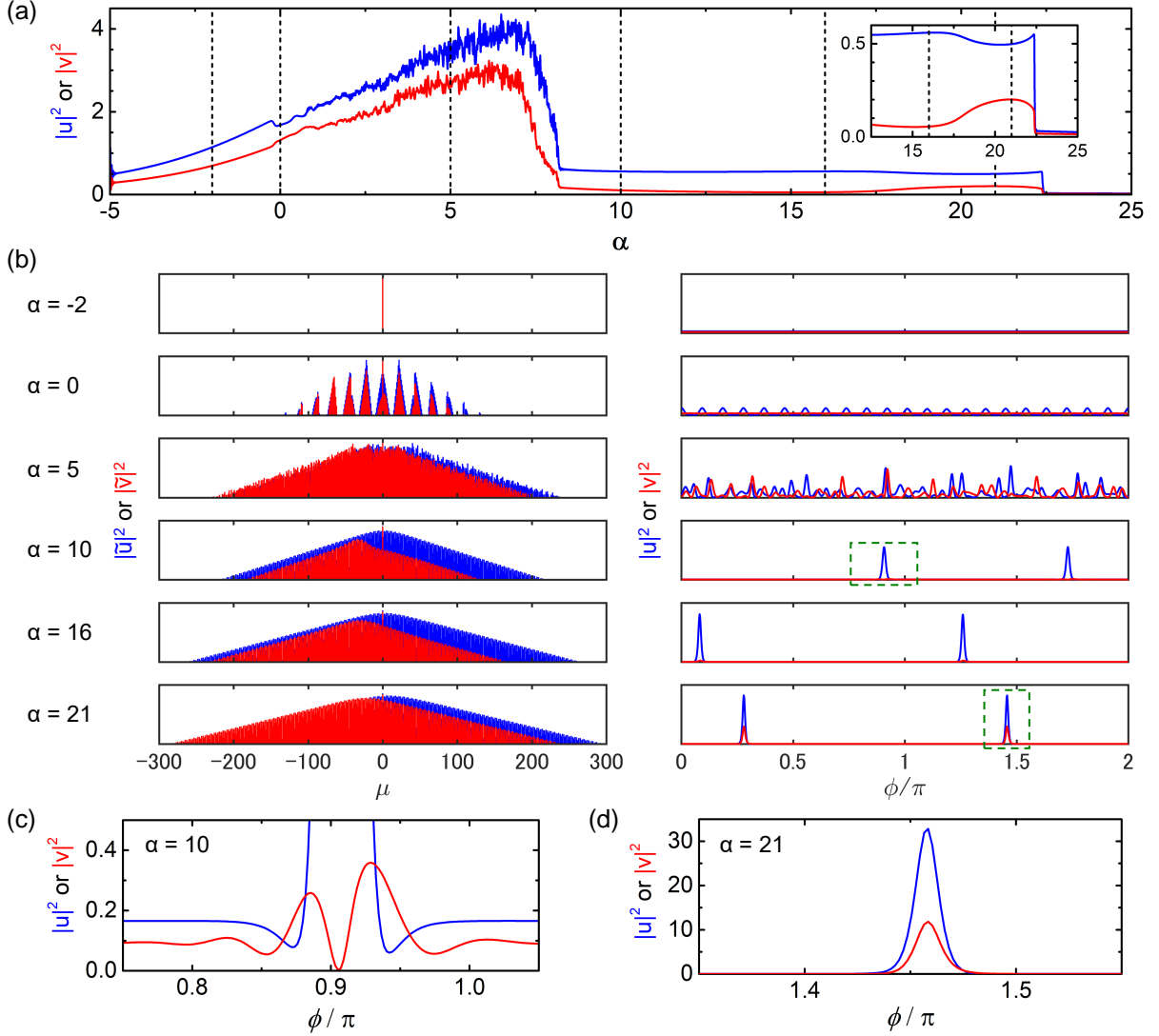


Fig. 6.5: Weakly pumped soliton (red, $F = 3$) generation supported by a strongly pumped soliton (blue, $F = 4$). Here, $\alpha_{(**)} = -2\Delta\omega_{0(*)}/\kappa$ and $F_{(**)} = (2s_{\text{in}(**)})/\kappa \sqrt{2g\kappa_{c(*)}/\kappa}$. (a) Dimensionless intracavity power of internal fields u and v while scanning α . The inset denotes near threshold behavior to form a soliton pulse. (b) Microcomb formation for spectra and waveforms at various α values. (c), (d) Detailed waveforms at α values of 10 and 21 in the green dashed boxes in (b).

a soliton microcomb is formed. The detailed waveforms of soliton microcombs in the green dashed box at α of 21 is shown in Fig. 6.5(d). The generation of the weakly pumped soliton v is supported by the strong soliton u . While α changes from 16 to 21, a weak soliton starts to be generated with near threshold behavior as shown in the inset of Fig. 6.5(a).

6.4 Analysis of trapped soliton solution

In this section, I calculate an analytical solution for trapped solitons using a Lagrangian perturbation approach and reveal the relation between the parameters. As a supplement, the general solution for a single soliton is briefly explained in Appendix A.

6.4.1 Master equations and ansatzes

Our analysis for soliton trapping conditions [126, 161, 162] uses transformed Eqs. (6.3) and (6.4), which utilize the relations $\delta = \gamma/\sqrt{2\beta}$ and $\theta = \phi/\sqrt{2\beta}$ and consider $\alpha = \alpha_{(u)} = \alpha_{(v)}$, $\beta = \beta_{(u)} = \beta_{(v)}$, and $F = F_{(u)} = F_{(v)}$:

$$\frac{\partial u}{\partial \tau} + i\alpha u - i\frac{1}{2}\frac{\partial^2 u}{\partial \theta^2} - i(|u|^2 + \sigma|v|^2)u - \delta\frac{\partial u}{\partial \theta} = F - u, \quad (6.5)$$

$$\frac{\partial v}{\partial \tau} + i\alpha v - i\frac{1}{2}\frac{\partial^2 v}{\partial \theta^2} - i(|v|^2 + \sigma|u|^2)v + \delta\frac{\partial v}{\partial \theta} = F - v. \quad (6.6)$$

I set ansatzes of stationary trapped solitons as

$$u(\theta) = B\text{sech}(\sqrt{1 + \sigma B}\theta) \exp(i\varphi_0) \exp(i\delta\theta), \quad (6.7)$$

$$v(\theta) = B\text{sech}(\sqrt{1 + \sigma B}\theta) \exp(i\varphi_0) \exp(-i\delta\theta), \quad (6.8)$$

where B is related to the pulse peak and width and φ_0 is the relative phase of the carrier from the soliton envelope. The difference between Eqs. (6.7) and (6.8) is the last term where δ represents the pulse advance and delay in the azimuthal angular coordinate.

6.4.2 Trapped soliton solution in coupled Lugiato-Lefever equations

To analyze the trapped soliton solution, Eqs. (6.5) and (6.6) lead to equations for the perturbed Lagrangian, the Lagrangian density \mathcal{L} , and the perturbations \mathcal{R}_u and \mathcal{R}_v as

$$\frac{\partial L_0}{\partial r_j} - \frac{d}{d\tau} \frac{\partial L_0}{\partial (\frac{\partial r_j}{\partial \tau})} = \int \left(\mathcal{R}_u \frac{\partial u^*}{\partial r_j} - \mathcal{R}_u^* \frac{\partial u}{\partial r_j} \right) d\theta + \int \left(\mathcal{R}_v \frac{\partial v^*}{\partial r_j} - \mathcal{R}_v^* \frac{\partial v}{\partial r_j} \right) d\theta, \quad (6.9)$$

$$L_0 = \int \mathcal{L} d\theta = \int \mathcal{L}_u d\theta + \int \mathcal{L}_v d\theta + \int \mathcal{L}_{uv} d\theta, \quad (6.10)$$

$$\mathcal{L}_u = \frac{1}{2} \left(u^* \frac{\partial u}{\partial \tau} - u \frac{\partial u^*}{\partial \tau} \right) + i\alpha |u|^2 + i \frac{1}{2} \left| \frac{\partial u}{\partial \theta} \right|^2 - i \frac{1}{2} |u|^4 - \frac{1}{2} \delta \left(u^* \frac{\partial u}{\partial \theta} - u \frac{\partial u^*}{\partial \theta} \right), \quad (6.11)$$

$$\mathcal{L}_v = \frac{1}{2} \left(v^* \frac{\partial v}{\partial \tau} - v \frac{\partial v^*}{\partial \tau} \right) + i\alpha |v|^2 + i \frac{1}{2} \left| \frac{\partial v}{\partial \theta} \right|^2 - i \frac{1}{2} |v|^4 + \frac{1}{2} \delta \left(v^* \frac{\partial v}{\partial \theta} - v \frac{\partial v^*}{\partial \theta} \right), \quad (6.12)$$

$$\mathcal{L}_{uv} = -i\sigma |u|^2 |v|^2, \quad (6.13)$$

$$\mathcal{R}_u = F - u, \quad (6.14)$$

$$\mathcal{R}_v = F - v. \quad (6.15)$$

Here r_j denotes the time-dependent coordinates. The integrals are calculated as

$$\begin{aligned} \int \mathcal{L}_u d\theta &= \int \mathcal{L}_v d\theta \\ &= i \frac{2B}{\sqrt{1+\sigma}} \frac{\partial \varphi_0}{\partial \tau} + i \frac{2B\alpha}{\sqrt{1+\sigma}} + \left(i \frac{B\delta^2}{\sqrt{1+\sigma}} + i \frac{\sqrt{1+\sigma} B^3}{3} \right) - i \frac{2B^3}{3\sqrt{1+\sigma}} - i \frac{2B\delta^2}{\sqrt{1+\sigma}}, \end{aligned} \quad (6.16)$$

$$\int \mathcal{L}_{uv} d\theta = -i \frac{4\sigma B^3}{3\sqrt{1+\sigma}}. \quad (6.17)$$

Using the equations described above, I calculate the stationary analytical solution with $dB/d\tau = 0$ and $d\varphi_0/d\tau = 0$ for the trapped soliton in a miroresonator.

First, with no perturbation ($\mathcal{R}_u = \mathcal{R}_v = 0$), Eq. (6.9) can be solved by using relations with $r_1 = B$ and $r_2 = \varphi_0$ as

$$\begin{aligned} \frac{\partial L_0}{\partial B} - \frac{d}{d\tau} \frac{\partial L_0}{\partial \left(\frac{\partial B}{\partial \tau} \right)} \\ &= i \frac{4}{\sqrt{1+\sigma}} \frac{\partial \varphi_0}{\partial \tau} + i \frac{4\alpha}{\sqrt{1+\sigma}} + \left(i \frac{2\delta^2}{\sqrt{1+\sigma}} + i 2\sqrt{1+\sigma} B^2 \right) - i \frac{4B^2}{\sqrt{1+\sigma}} - i \frac{4\delta^2}{\sqrt{1+\sigma}} - i \frac{4\sigma B^2}{\sqrt{1+\sigma}} \\ &= i \frac{4}{\sqrt{1+\sigma}} \left\{ \frac{\partial \varphi_0}{\partial \tau} + \alpha - \frac{\delta^2}{2} - \frac{1}{2}(1+\sigma)B^2 \right\}, \end{aligned} \quad (6.18)$$

$$\frac{\partial L_0}{\partial \varphi_0} - \frac{d}{d\tau} \frac{\partial L_0}{\partial \left(\frac{\partial \varphi_0}{\partial \tau} \right)} = -i \frac{4}{\sqrt{1+\sigma}} \frac{dB}{d\tau}, \quad (6.19)$$

As a result, the equation is obtained by Eq. (6.18) with $d\varphi_0/d\tau = 0$ as

$$0 = \frac{1}{2} \delta^2 + \frac{1}{2} (1+\sigma) B^2 - \alpha, \quad (6.20)$$

that represents the relation of the trapped soliton parameters in the stationary state.

Next, with perturbation following Eqs. (6.14) and (6.15), the perturbation term in Eq. (6.9)

is calculated with $r_1 = B$:

$$\begin{aligned} & \mathcal{R}_u \frac{\partial u^*}{\partial B} - \mathcal{R}_u^* \frac{\partial u}{\partial B} \\ &= F \exp(-i\varphi_0) \exp(-i\delta\theta) \operatorname{sech}(\sqrt{1+\sigma}B\theta) \{1 - \sqrt{1+\sigma}B\theta \tanh(\sqrt{1+\sigma}B\theta)\} \\ & \quad - F \exp(i\varphi_0) \exp(i\delta\theta) \operatorname{sech}(\sqrt{1+\sigma}B\theta) \{1 - \sqrt{1+\sigma}B\theta \tanh(\sqrt{1+\sigma}B\theta)\}, \end{aligned} \quad (6.21)$$

$$\begin{aligned} & \mathcal{R}_v \frac{\partial v^*}{\partial B} - \mathcal{R}_v^* \frac{\partial v}{\partial B} \\ &= F \exp(-i\varphi_0) \exp(i\delta\theta) \operatorname{sech}(\sqrt{1+\sigma}B\theta) \{1 - \sqrt{1+\sigma}B\theta \tanh(\sqrt{1+\sigma}B\theta)\} \\ & \quad - F \exp(i\varphi_0) \exp(-i\delta\theta) \operatorname{sech}(\sqrt{1+\sigma}B\theta) \{1 - \sqrt{1+\sigma}B\theta \tanh(\sqrt{1+\sigma}B\theta)\}, \end{aligned} \quad (6.22)$$

$$\int \left(\mathcal{R}_u \frac{\partial u^*}{\partial B} - \mathcal{R}_u^* \frac{\partial u}{\partial B} \right) d\theta = \int \left(\mathcal{R}_v \frac{\partial v^*}{\partial B} - \mathcal{R}_v^* \frac{\partial v}{\partial B} \right) d\theta \approx i \frac{2F\delta^2 C_2}{(1+\sigma)^{\frac{3}{2}} B^3} \sin \varphi_0. \quad (6.23)$$

Also, the perturbation term in Eq. (6.9) is calculated with $r_2 = \varphi_0$:

$$\begin{aligned} & \mathcal{R}_u \frac{\partial u^*}{\partial \varphi_0} - \mathcal{R}_u^* \frac{\partial u}{\partial \varphi_0} \\ &= -iFB \exp(i\varphi_0) \operatorname{sech}(\sqrt{1+\sigma}B\theta) \exp(i\delta\theta) \\ & \quad - iFB \exp(-i\varphi_0) \operatorname{sech}(\sqrt{1+\sigma}B\theta) \exp(-i\delta\theta) + i2B^2 \operatorname{sech}^2(\sqrt{1+\sigma}B\theta), \end{aligned} \quad (6.24)$$

$$\begin{aligned} & \mathcal{R}_v \frac{\partial v^*}{\partial \varphi_0} - \mathcal{R}_v^* \frac{\partial v}{\partial \varphi_0} \\ &= -iFB \exp(i\varphi_0) \operatorname{sech}(\sqrt{1+\sigma}B\theta) \exp(-i\delta\theta) \\ & \quad - iFB \exp(-i\varphi_0) \operatorname{sech}(\sqrt{1+\sigma}B\theta) \exp(i\delta\theta) + i2B^2 \operatorname{sech}^2(\sqrt{1+\sigma}B\theta), \end{aligned} \quad (6.25)$$

$$\begin{aligned} & \int \left(\mathcal{R}_u \frac{\partial u^*}{\partial \varphi_0} - \mathcal{R}_u^* \frac{\partial u}{\partial \varphi_0} \right) d\theta = \int \left(\mathcal{R}_v \frac{\partial v^*}{\partial \varphi_0} - \mathcal{R}_v^* \frac{\partial v}{\partial \varphi_0} \right) d\theta \\ & \approx -i \frac{2F}{\sqrt{1+\sigma}} \left\{ \pi - \frac{\delta^2 C_1}{2(1+\sigma B^2)} \right\} \cos \varphi_0 + i \frac{4B}{\sqrt{1+\sigma}}. \end{aligned} \quad (6.26)$$

Here $C_1 = \int x^2 \operatorname{sech} x \, dx$, $C_2 = \int \{x^2 \operatorname{sech} x - x^3 \operatorname{sech} x \tanh x\} dx$, and $\sqrt{1+\sigma}B \gg \delta$ for an approximate calculation. Eq. (6.9) calculates the relations with $r_1 = B$ using Eqs. (6.18) and (6.23) and with $r_2 = \varphi_0$ using Eqs. (6.19) and (6.26):

$$i \frac{4}{\sqrt{1+\sigma}} \left\{ \frac{\partial \varphi_0}{\partial \tau} + \alpha - \frac{\delta^2}{2} - \frac{1}{2}(1+\sigma)B^2 \right\} = i \frac{4F\delta^2 C_2}{(1+\sigma)^{\frac{3}{2}} B^3} \sin \varphi_0, \quad (6.27)$$

$$-i \frac{4}{\sqrt{1+\sigma}} \frac{dB}{d\tau} = -i \frac{4F}{\sqrt{1+\sigma}} \left\{ \pi - \frac{\delta^2 C_1}{2(1+\sigma B^2)} \right\} \cos \varphi_0 + i \frac{8B}{\sqrt{1+\sigma}}. \quad (6.28)$$

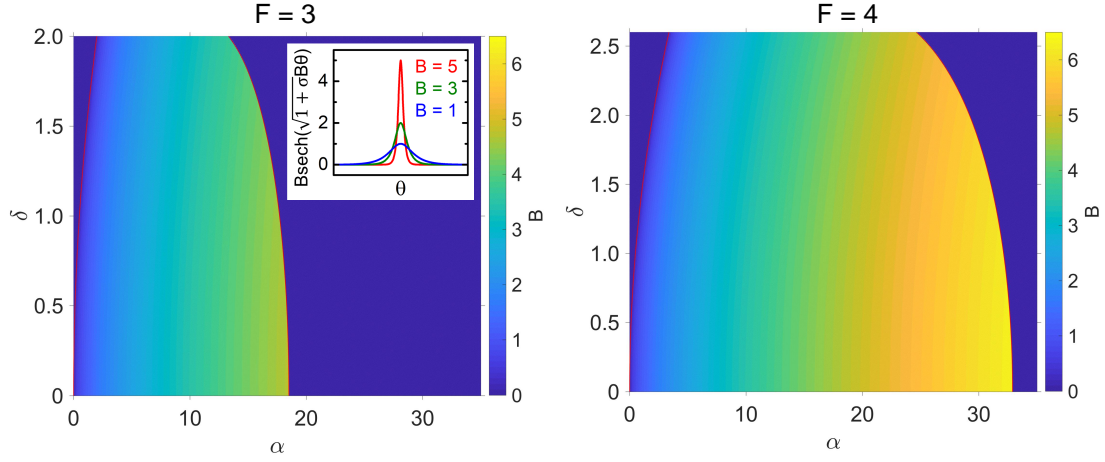


Fig. 6.6: Analytical solutions for trapped solitons where F of 3 and 4 as functions of α , δ , and B , which are related to the pump detuning, the difference between repetition frequencies, and the peak power of the trapped soliton, respectively. The inset represents the amplitude of a stationary trapped soliton. Here, $\alpha_{(**)} = -2\Delta\omega_{0(**)}/\kappa$, $F_{(**)} = (2s_{\text{in}(**)}/\kappa)\sqrt{2g\kappa_{c(**)}/\kappa}$, and $\delta = \gamma/\sqrt{2\beta} = \Delta D_1/\sqrt{2D_2\kappa}$.

Consequently, the differential equations for the parameters B and φ_0 are obtained as

$$\frac{dB}{d\tau} = -2B + F \left\{ \pi - \frac{\delta^2 C_1}{2(1+\sigma)B^2} \right\} \cos \varphi_0, \quad (6.29)$$

$$\frac{d\varphi_0}{d\tau} = \frac{1}{2}\delta^2 + \frac{1}{2}(1+\sigma)B^2 - \alpha + \frac{F\delta^2 C_2}{(1+\sigma)B^3} \sin \varphi_0. \quad (6.30)$$

The stationary trapped soliton parameters can be calculated with $dB/d\tau = 0$ and $d\varphi_0/d\tau = 0$. Also, the maximum α and B values for stationary trapped solitons are obtained at $\cos \varphi_0 = 1$ because the below equation is satisfied using $\sqrt{1+\sigma}B \gg \delta$:

$$\pi - \frac{C_1}{2} \left(\frac{\delta}{\sqrt{1+\sigma}B} \right)^2 > 0. \quad (6.31)$$

Therefore the maximum α and B in the stationary state have relations as

$$B_{\text{max}}^3 - \frac{1}{2}\pi F B_{\text{max}}^2 + \frac{F\delta^2 C_1}{4(1+\sigma)} = 0, \quad (6.32)$$

$$\alpha_{\text{max}} = \frac{1}{2}\delta^2 + \frac{1}{2}(1+\sigma)B_{\text{max}}^2. \quad (6.33)$$

Figure 6.6 shows analytical results for a trapped soliton solution with F of 3 and 4. With a large δ , trapped solitons cannot be obtained with a small positive α on the red-detuned side. The α range for soliton trapping becomes narrower as δ increases. This analytical result helps in terms of demonstrating and controlling trapped soliton generation. For example, trapped solitons with a high peak power can be generated by suitably scanning and stopping the pump frequencies, which are related to α . Moreover, B increases as α increases, and the relation can be used to stabilize of microcomb generation as with a single soliton [168].

6.5 Summary

The author numerically and theoretically studied dual-comb generation and soliton trapping in a single microresonator, whose two transverse modes were excited with orthogonally polarized dual-pumping (TE and TM modes). The simulation model employed coupled LLEs, which take account of XPM and difference between the repetition frequencies. The numerical simulation calculated the dual-comb formation in a microresonator, whose microcombs propagated as soliton pulses and caused soliton trapping depending on the parameters. This is a first theoretical study on soliton trapping between dual-comb in a single microresonator.

Our model simulates a case where a trapped soliton is generated by one of the original solitons, which also supports the generation of a soliton in the other transverse mode. The trapped solitons are advanced and delayed in the time domain, whose comb envelopes are shifted to higher and lower frequency sides. In addition, an analytical solution for trapped solitons in coupled LLEs is obtained by using a Lagrangian perturbation approach that reveals the soliton trapping conditions.

Such a system, where orthogonally polarized transverse modes in a single microresonator are excited, has advantages as regards generating a dual-comb with a controlled difference between the repetition frequencies in a single microresonator, particularly one fabricated by polishing or laser processing. Revealing the conditions of dual-comb soliton generation and soliton trapping is helpful for optimizing experimental conditions and cavity dispersion to induce or avoid these phenomena.

Chapter 7

Summary and outlook

This chapter summarizes the work written in this thesis and provides an outlook for future research related to microresonator frequency combs.

7.1 Summary of this thesis

This thesis reported the background, theory, and experiment of microresonators and microcombs in Chapter 1, 2, and 3 and microcombs with cavity optomechanics in Chapter 4, with SRS in Chapter 5, and with XPM in Chapter 6. These studies contribute to the understanding of the effects of optical nonlinearities in a microresonator on microcombs. Also, these results may help to guide future research and novel ideas.

Chapter 1 introduced the background to microresonators and microcombs to clarify the motivation of this thesis. It included the types of microresonators, conventional mode-locked lasers, basic microcomb generation schemes, milestones in microcomb researches, microcomb applications, related researches to this thesis, and the motivation of this thesis.

Chapter 2 explained microresonator characteristics in theory, simulations, and experiments. The author fabricated silica toroid, silica rod, and polished MgF_2 microresonators, whose Q factors were achieved to tens of millions, hundreds of millions, and over one billion, respectively. The optical coupling was performed using a tapered fiber, whose transmission was around 98% and maximum coupling efficiency to a microresonator was over 95%. To evaluate cavity dispersions, the author developed a measurement system with a fiber MZI and a calculation system using a finite element simulation.

Chapter 3 introduced microcomb characteristics including the theory based on an LLE and the experimental results. On the basis of an LLE, the numerical simulation and analysis were performed. The microcomb formation from a CW state to a soliton state were shown by calculating an LLE. The author explained that the positions of first sidebands via degenerate FWM are determined by the intracavity power, threshold for FWM, cavity dispersion, and pump detuning. In addition, the author analytically explained that red-detuned pumping and anomalous dispersion are required for a soliton state. In our experiments, a high-Q microresonator was pumped with a CW laser by scanning the pump frequency. The author observed Turing pattern and chaos combs with blue-detuned pumping and soliton steps with red-detuned pumping.

Chapter 4 described a study of cavity optomechanical behavior on microcomb generation, experimentally and numerically. In many previous studies of cavity optomechanics using a toroid microresonator, the oscillation modes were excited with a low pump power that was much smaller than the threshold power for FWM. Although the cavity optomechanical behavior in comb generation has been reported, it has not been well understood. Here the author demonstrated the suppression of OMPOs with a Turing pattern comb, which was generated by a blue-detuned pump from the resonance frequency. When only the influence of the blue-detuned pump light is considered, optomechanical oscillations are always amplified. On the other hand, the suppression of OMPO with a Turing pattern comb can be explained and achieved by assisting the influence of all the comb lines, which are in the red-detuning regime. In addition, this study provides a guideline of designing microresonator properties by using the LLE and equation for calculating effective damping rate. To control the properties of cavity dispersion and also threshold power for degenerate FWM (related to an optical Q factor) enables OMPO suppression and microcomb generation that has low phase noise in optomechanical coupling systems.

Chapter 5 describes a study of Raman comb formation in silica rod microresonators, experimentally and numerically. Recently, multi-mode Raman lasing in a high-Q optical microresonator has been reported. Raman combs have an advantage that they can be generated regardless of the cavity dispersion. However, the formation dynamics of a Raman comb has not been well exploited. Here this study provides how to control the operation wavelength and formation of a Raman comb through pump detuning and coupling strength. The author generated Raman combs from a silica rod microresonator with a FSR in microwave rate and controlled the center wavelength via detuning and coupling optimizations. In the experiment, decreasing detuning leads to the Raman energy transition from Peak 1 to Peak 2, which is a similar behavior that has been observed in silica fibers. Also, weak coupling induced to generate a Raman comb at Peak 2, while strong coupling results the only excitation of Peak 1. Those observations are in agreement with simulation, which are calculated by using coupled mode equations taking account of Raman processes. In addition, the center wavelength shift of a Raman comb was observed, with a shift that is 37 times larger than that of pump scanning. The combination of this study and previous researches on phase-locking scheme will enable generation of Raman combs that have a smooth spectral envelope and mutual coherence between the comb lines.

Chapter 6 reported numerical simulation and analysis for dual-comb generation and soliton trapping in a single microresonator. Recently, mode-locked soliton microcomb was reported, and opening the way for many practical applications including dual-comb spectroscopy and LiDAR. For dual-comb applications, it is a very attractive approach to generate dual-comb soliton with orthogonal polarizations (TE and TM modes) in a single microresonator. However, an experimental demonstration and also a theoretical study have yet to be performed. Here the author numerically and theoretically studied dual-comb generation and soliton trapping in a single microresonator, whose two transverse modes were excited with orthogonally polarized dual-pumping (TE and TM modes). The simulation model employed coupled LLEs, which take account of XPM and difference between the repetition frequencies. The numerical simulation calculated the dual-comb formation in a microresonator, whose microcombs propagated as soliton pulses and caused soliton trapping depending on the parameters. This is a first theoretical study on soliton trapping between dual-comb in a single microresonator. Our model simulates

a case where a trapped soliton is generated by one of the original solitons, which also supports the generation of a soliton in the other transverse mode. The trapped solitons are advanced and delayed in the time domain, whose comb envelopes are shifted to higher and lower frequency sides. In addition, an analytical solution for trapped solitons in coupled LLEs is obtained by using a Lagrangian perturbation approach that reveals the soliton trapping conditions. Such a system, where orthogonally polarized transverse modes in a single microresonator are excited, has advantages as regards generating a dual-comb with a controlled difference between the repetition frequencies in a single microresonator, particularly one fabricated by polishing or laser processing. Revealing the conditions of dual-comb soliton generation and soliton trapping is helpful for optimizing experimental conditions and cavity dispersion to induce or avoid these phenomena.

7.2 Outlook

Microresonator frequency combs have been actively studied since the first important study was reported in 2007 [5]. The formation dynamics and method to generate mode-locked soliton pulses have been well understood [39]. Also, influences of various optical effects and microresonator parameters have been studied, including self-frequency shift and spectral broadening with Raman scattering [99, 102], broadband comb generation with higher order dispersion [46], dark soliton microcomb generation in a normal dispersion microresonator with mode coupling between different transverse modes [145], and dual-comb generation with dual-pumping and XPM [111, 169]. Recently, many demonstrations of microcomb applications have been reported, such as optical communications [50], dual-comb spectroscopy and LiDAR [55, 60, 61], astrocombs [63, 64], optical frequency synthesizers [66], and microwave oscillators [69] (which are introduced in §1.3.3). However, for practical applications, useful platforms and systems will be required. Hence, a lot of problems still remain, such as integration of microresonators and coupling waveguides (particularly for whispering-gallery mode microresonators), soliton microcomb with low pump power that is less than 10 mW (without optical amplifiers), high conversion efficiency from a CW pump to a microcomb, various wavelength operation such as in visible and mid-infrared wavelengths, and robustness against thermal and other noise. Overcoming these problems will allow for practical applications which cannot be realized using conventional mode-locked lasers.

Appendix A

Analysis of soliton solution in a single Lugiato-Lefever equation

In this appendix, soliton solution in a single LLE is briefly introduced to help understanding §6.4. The master equation and ansatz are obtained by setting σ and δ at zero in Eqs. (6.5)-(6.8). An approximate solution for a dissipative soliton in an LLE can be obtained using a Lagrangian perturbation approach by regarding input and loss terms as a perturbation [146, 170, 171]. When Eq. (6.5) is used for the analysis in a single LLE, the Lagrangian density \mathcal{L} and perturbation \mathcal{R} have a relation as

$$\frac{\partial \mathcal{L}}{\partial u^*} - \frac{\partial}{\partial \tau} \frac{\partial \mathcal{L}}{\partial (\frac{\partial u^*}{\partial \tau})} - \frac{\partial}{\partial \theta} \frac{\partial \mathcal{L}}{\partial (\frac{\partial u^*}{\partial \theta})} = \mathcal{R}, \quad (\text{A.1})$$

which is led based on the principle of least action that the energy integral of physics path from one to another state takes minimum. Here the Lagrangian density \mathcal{L} and perturbation \mathcal{R} are

$$\mathcal{L} = \frac{1}{2} \left(u^* \frac{\partial u}{\partial \tau} - u \frac{\partial u^*}{\partial \tau} \right) + i\alpha |u|^2 + i \frac{1}{2} \left| \frac{\partial u}{\partial \theta} \right|^2 - i \frac{1}{2} |u|^4, \quad (\text{A.2})$$

$$\mathcal{R} = F - u. \quad (\text{A.3})$$

Eqs. (6.7), (A.2), and (A.3) are solved by following

$$\frac{\partial L_0}{\partial r_j} - \frac{d}{d\tau} \frac{\partial L_0}{\partial (\frac{\partial r_j}{\partial \tau})} = \int \left(\mathcal{R} \frac{\partial u^*}{\partial r_j} - \mathcal{R}^* \frac{\partial u}{\partial r_j} \right) d\theta, \quad (\text{A.4})$$

$$\begin{aligned} L_0 = \int \mathcal{L} d\theta &= \int \left\{ \frac{1}{2} \left(u^* \frac{\partial u}{\partial \tau} - u \frac{\partial u^*}{\partial \tau} \right) + i\alpha |u|^2 + i \frac{1}{2} \left| \frac{\partial u}{\partial \theta} \right|^2 - i \frac{1}{2} |u|^4 \right\} d\theta \\ &= i2B \frac{\partial \varphi_0}{\partial \tau} + i2B\alpha + i \frac{1}{3} B^3 - i \frac{2}{3} B^3 \\ &= i2B \frac{\partial \varphi_0}{\partial \tau} + i2B\alpha - i \frac{1}{3} B^3, \end{aligned} \quad (\text{A.5})$$

Appendix A. Analysis of soliton solution in a single Lugiato-Lefever equation

where r_j denotes the time-dependent coordinates. By using the ansatz in Eq. (6.7), Eq. (A.4) with $r_1 = B$ and $r_2 = \varphi_0$ is solved as

$$\frac{dB}{d\tau} = -2B + \pi F \cos \varphi_0, \quad (\text{A.6})$$

$$\frac{d\varphi_0}{d\tau} = \frac{1}{2}B^2 - \alpha. \quad (\text{A.7})$$

These lead to the stationary soliton parameters ($dB/d\tau = 0$, $d\varphi_0/d\tau = 0$): $\cos \varphi_0 = 2B/(\pi F)$, $B = \sqrt{2\alpha}$, and $\alpha_{\max} = \pi^2 F^2/8$ (maximum α for the stationary soliton).

Appendix B

Delayed self-heterodyne measurement

I evaluated linewidths of pump and reference lasers using delayed self-heterodyne measurement with an experimental setup, as shown in Fig. B.1. The laser light was divided into two pathways. One pathway had a delay line of a 2 km single-mode fiber to be incoherent between the divided two light. The minimum measurable linewidth $\Delta\nu$ in this system is determined by the length of the delay line as

$$\Delta\nu = \frac{c}{nL_{\text{fiber}}}, \quad (\text{B.1})$$

where c is the speed of light, n is the refractive index of the delay line material, and L_{fiber} is the length of the delay line. For example, this system with a 2 km delay line can measure a linewidth down to around 100 kHz. On the other hand, the other pathway has a phase modulator which creates frequency-shifted sidebands from the carrier. One sideband is filtered out using a bandpass filter. The combined light is launched to a photodetector that makes the delayed self-heterodyne signal. Figure B.1(b) shows the self-heterodyne signals with (blue) and without (green) the delay line. Without the delay line, since the divided light in two pathways was coherent, the heterodyne signal had a near zero linewidth. On the other hand, with the delay line, the self-heterodyne signal had a linewidth of 220 kHz ($> \Delta\nu$). Figure B.1(c) shows delayed self-heterodyne signals with two different external-cavity diode lasers (Santec TSL-510 and TSL-710), whose linewidths were 356 and 220 kHz, respectively.

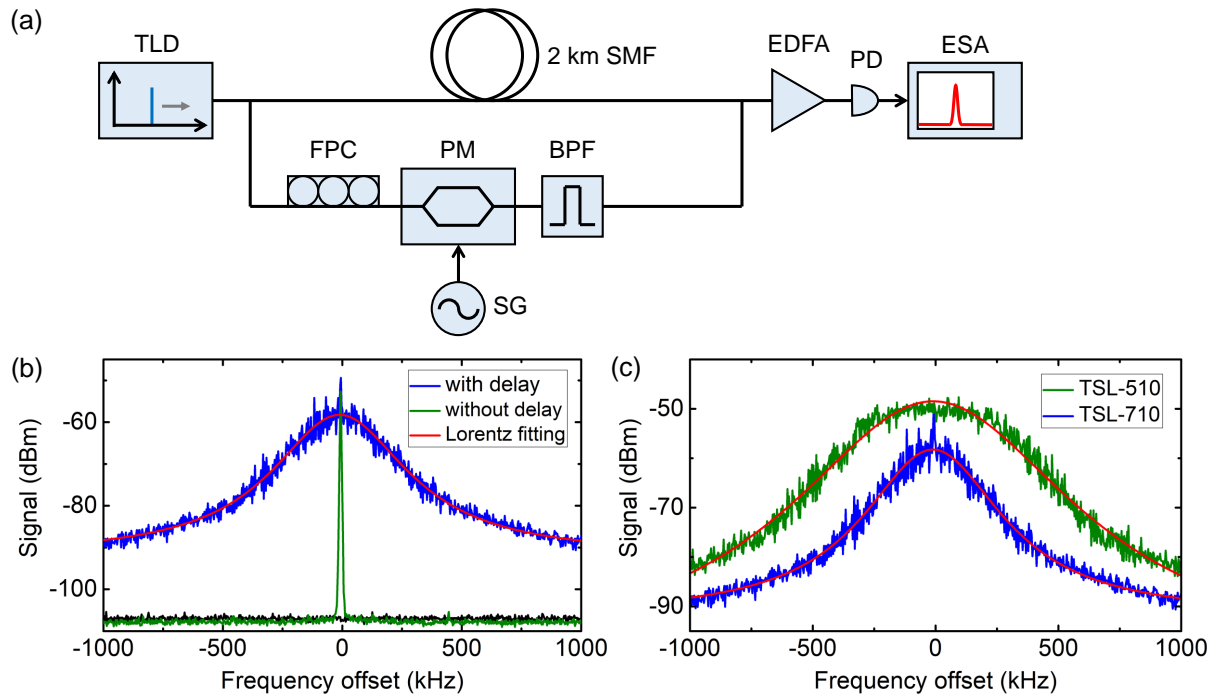


Fig. B.1: (a) Experimental setup of delayed self-heterodyne measurement for laser linewidths. One pathway is to a delay line (2 km single-mode fiber) and the other is to a phase modulator which creates frequency-shifted sidebands from the carrier. One sideband is filtered out using a bandpass filter. The combined light is launched to a photodetector that makes the delayed self-heterodyne signal. TLD: tunable laser diode, SMF: single-mode fiber, FPC: fiber polarization controller, PM: phase modulator, SG: electrical signal generator, BPF: bandpass filter, EDFA: erbium-doped fiber amplifier, PD: photodetector, ESA: electrical spectrum analyzer. (b) Self-heterodyne signals with (blue) and without (green) the delay line. Without the delay line, since the divided light in two pathways is coherent, the heterodyne signal has near zero linewidth. (c) Delayed self-heterodyne signals of two external-cavity diode lasers (Santec TSL-510 and TSL-710), whose linewidths are 356 and 220 kHz, respectively.

Appendix C

Dual-pump to a single transverse mode

The microcomb generation usually adopts single frequency pumping. In this case, the comb formation starts with degenerate FWM that determines the comb properties such as the mode spacings and the coherence. On the other hand, dual-pumping techniques can manipulate the properties by using two individual pump lasers [172], two tunable bandpass filters in a loop cavity [173], or a modulated single pump laser [174, 175].

Here, I demonstrated dual-pump microcomb generation, whose mode spacing was controlled by selecting the two pump modes. The two individual pump lasers were combined and launched to a toroid microresonator which has a 555 GHz cavity FSR. The total pump power was around 300 mW. Figure C.1 shows the microcomb spectra, which have mode spacings corresponding to between 1- to 6-FSR of the toroid microresonator. The two pumped resonances, which are shown with red arrows, belong to same transverse mode. As shown in Fig. C.1, the control of mode spacing was clearly demonstrated. In addition, we performed the same experiment with 160 mW pump power which is near threshold for FWM. Although (degenerate) FWM could not be observed with single frequency pumping, (non-degenerate) FWM occurred with dual-pumping (80 mW in each pump laser). This is because threshold power for non-degenerate FWM is lower than that for degenerate FWM [172].

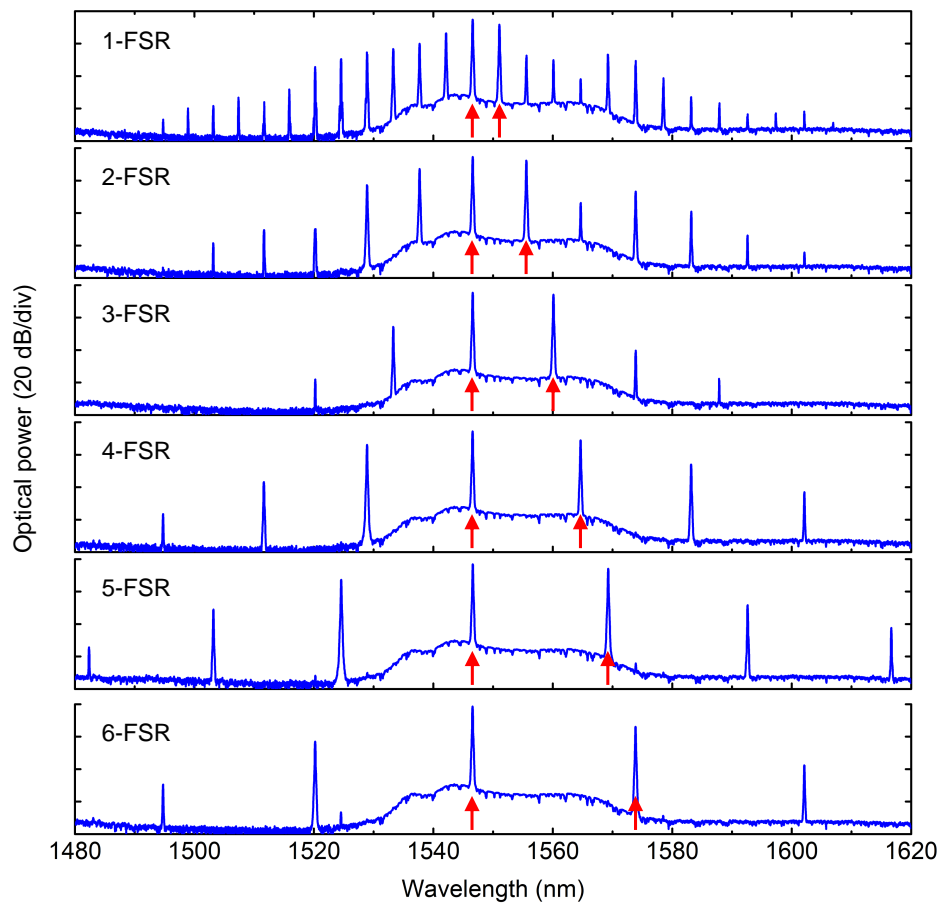


Fig. C.1: Dual-pumped microcomb spectra in a toroid microresonator which has a cavity FSR of 555 GHz. The mode spacing of the generated microcomb was controlled by selecting the pump modes, which are represented with red arrows. The total pump power was 300 mW.

Appendix D

Coupling strength control with octagonal toroid microresonators

Light is usually coupled to a whispering-gallery mode microresonator using a tapered fiber. However, it is difficult to stabilize the optical coupling against mechanical vibration because it requires sub- μm control of the gap distance between the fiber and resonator. Here, the author experimentally demonstrates mechanically robust coupling that allows the tapered fiber to touch the sidewall of the resonator. By using an octagonal toroid microresonator, the resonator-waveguide system from over coupling is prevented and critical coupling is achieved even when the fiber is in contact with the surface of the resonator. It is shown by numerical analysis that such a deformed microresonator is required if to control the coupling is needed, since a circular resonator usually over-couples when the fiber contacts the surface. The fabricated octagonal silica toroid microresonator exhibits a quality factor of 2.2×10^4 when the tapered fiber touches a resonator with a diameter of $80 \mu\text{m}$.

D.1 Introduction

The optical coupling condition has three regimes, namely, under coupling ($K < 1$), critical coupling ($K = 1$) and over coupling ($K > 1$), where K is given as $K = \kappa_c/\kappa_i = Q_i/Q_c$. The power transmission from a microresonator through a coupler is given as

$$(\text{Transmission}) = \frac{(K - 1)^2}{(K + 1)^2}, \quad (\text{D.1})$$

as explained in §2.1.1. A critical coupling condition is the most effective regime in which to perform various demonstrations [117, 118]. However, it should be noted that stable coupling is usually not easy to achieve.

In previous studies, deformed microresonators such as an elliptic silica toroid, a polygonal silicon microdisk and a hexagonal crystalline rod have been investigated, for instance, to enhance coupling with free space [176] or to obtain optimal coupling with a waveguide [177–179]. Since a deformed microresonator exhibits different mode structures, it would be a good idea to use

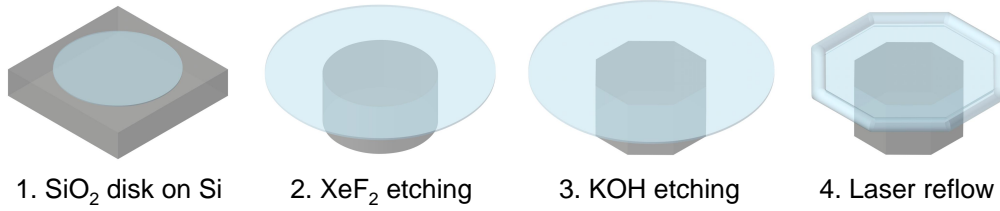


Fig. D.1: Schematic illustration of the process for fabricating an octagonal toroid microresonator.

the modulation of the resonator shape to control the optical coupling. The purpose is to experimentally demonstrate mechanically stable optical coupling by changing the resonator shape from circular to octagonal. I attempt to obtain critical coupling, even when the tapered fiber is in contact with the resonator, which is a challenging task. This enables us to achieve higher Q_c (it means higher Q if Q_i is much higher than Q_c) by using octagonal resonator than circular resonator whose size is same.

D.2 Fabrication of octagonal silica toroid microresonators

I use a silica toroid microresonator fabricated on a silicon chip. The conventional process for fabricating a circular toroid microresonator has three steps. First, a circular silica disk is fabricated on a thermo-oxidized silicon wafer by photolithography and the HF etching of silica. Then a silica disk on silicon post is formed by the selective isotropic etching of silicon with XeF₂ gas. Finally, laser reflow process is employed with a CO₂ laser beam, where the structure is heated and its rim melted. This process gives the edge of the silica disk a toroidal shape. The disk edge has a very smooth surface and reduces the scattering loss. As a result, an ultrahigh- Q is obtained. It should be noted that the resonator shape is dependent on the shape of the silicon post, because the post works as a heat sink during the laser reflow process. Here, I employ silicon anisotropic etching in potassium hydroxide (KOH) solution to fabricate an octagonal resonator. In brief, fabricating an octagonal silicon post by anisotropic etching enables us to realize an octagonal toroid resonator.

Isotropic etchants such as XeF₂ gas etch $\langle 100 \rangle$, $\langle 110 \rangle$ and $\langle 111 \rangle$ crystal faces at the same rate, so an undercut silicon post has a circular shape. On the other hand, anisotropic etching with KOH etches $\langle 100 \rangle$ and $\langle 110 \rangle$ crystal faces faster. As a result, the silicon post will form an octagonal cross section [179, 180]. By combining both isotropic and anisotropic etching, I obtained an optimized equilateral octagonal shape. Figure D.1 shows the fabrication process. The difference from an octagon with a circular toroidal resonator is the use of KOH etching. First a 100 μm silica disk is fabricated on a silicon wafer. Then, the silicon is etched by XeF₂ gas to obtain an 80 μm diameter post. Then KOH at a temperature of 45°C is used for the anisotropic etching. The sample is etched for 40 min to realize an optimized octagonal shape. Finally, a CO₂ laser reflow process is employed. Figure D.2 shows a SEM image of a fabricated octagonal toroid microresonator with a resonator diameter of 80 μm and a toroidal waveguide diameter of 3.5 μm . The image shows that the curvatures of the sidewall and the corner are about 240 μm and 20 μm , respectively.

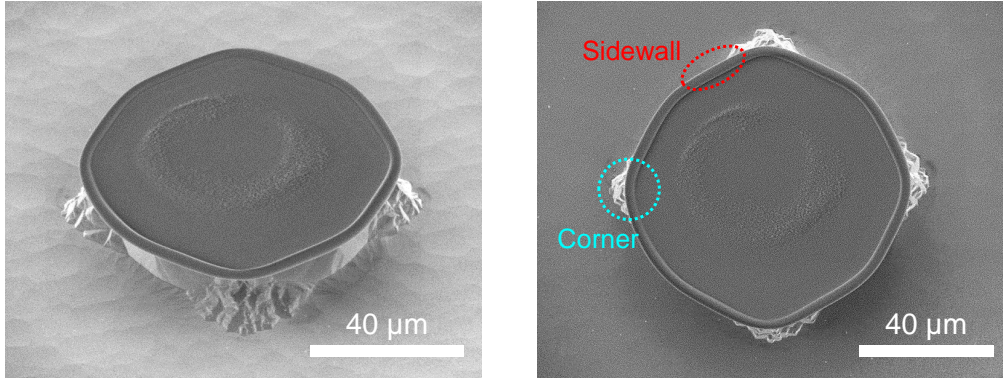


Fig. D.2: SEM images of a fabricated octagonal silica toroid microresonator.

D.3 Optical measurement of octagonal toroid microresonators

In our previous work [180], an octagonal toroid resonator will exhibit a theoretical Q of 8.8×10^6 is numerically shown. A close view of the resonator mode reveals that the light propagates close to the surface at the corner but slightly inward at the sidewall. This feature allows us to change the coupling coefficient of the resonator mode with a tapered fiber by either contacting it at the corner or at the sidewall of the resonator. Here the author shows experimentally that the coupling coefficient is different and much higher Q_c can be obtained even when the fiber is in contact with the resonator.

I measured the transmission spectrum of the octagonal resonator using a conventional tapered fiber setup. The diameter of the tapered fiber was about 1-2 μm . The resonator was set on the 3-axis motorized stage (10 nm resolution) to control the gap between the fiber. The distance is monitored with a microscope from the top and side of the device. The position of the rim of the toroid microresonator is about 15 μm high from the surface of the silicon wafer, so the tapered fiber can be adjusted without touching it with the wafer. I placed the fiber at the sidewall (sidewall coupling) and at the corner (corner coupling) of the octagonal resonator and changed the gap distance between the fiber and the resonator.

Figure D.3(a) is the dip depth of the resonance spectrum of the resonator for different gap distances. Since the transmittance of a side-coupled resonator at a resonant wavelength is given by Eq. (D.1), the depth is largest when the resonator is in a critical coupling condition. Figure D.3(a) shows that a gap distance of 200 to 300 nm obtains critical coupling when the waveguide couples with the resonator at the corner. It over-couples with the resonator when the fiber is in contact with the resonator surface. On the other hand, it is close to or at the critical coupling condition when the fiber couples with the sidewall of the resonator. This is because the coupling coefficient is dependent to the overlap of the mode field distributions of the resonator and the fiber. Since the curvatures of the sidewall are larger than that of the corner, the light propagates closer to the surface at the corner than at the sidewall. These results are in good agreement with the previous simulation. The transmittance spectrum is shown in Fig. D.3(b), and the Q values of fundamental mode were 2.2×10^4 for sidewall coupling and 6.3×10^3 for corner coupling (both in contact). Although the reason on the lower Q is not clear, the author

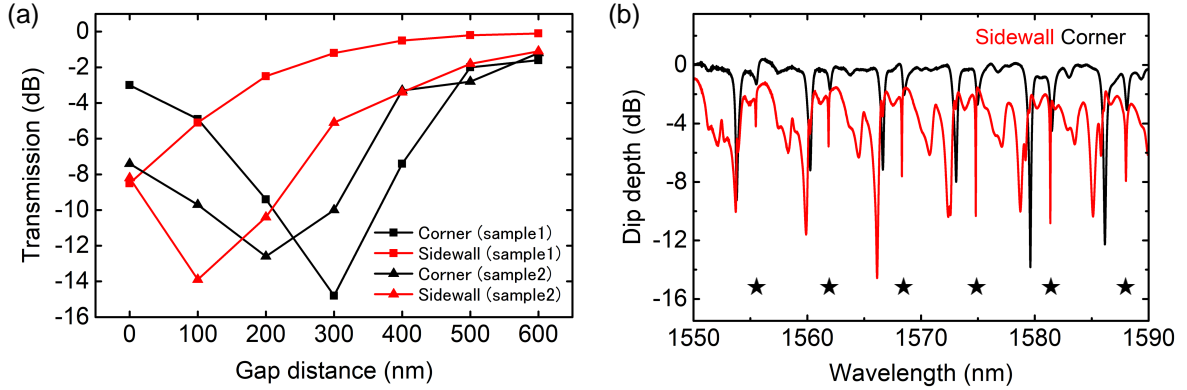


Fig. D.3: (a) Transmission at the resonance with different gap distances. Black and red symbols indicate when the fiber touched the corner and the sidewall of an octagonal resonator, respectively. The transmission is dependent to the coupling efficiency and it is at the lowest at a critical coupling condition. (b) Measured transmission spectrum when a tapered fiber is in contact (gap distance is 0 nm) at the sidewall (red) and the corner (black) of the resonator. The low background transmittance for the sidewall coupling is due to the excitation of the low-Q higher-order transverse mode.

believes it is due to the combination of several effects, such as the residual surface roughness and asymmetric deformation due to the process imperfectness. Throughout this study, I focus on the resonances in the fundamental mode, which are indicated with asterisks. That can be recognized because they appear at first when approaching a fiber closer to the resonator starting from a large gap distance. The fundamental mode, which is often of interest, usually exhibit the smallest Q_c among various modes, since it propagates closest to the resonator surface; hence the Q_c need to be controlled.

As I discuss in the next section, over coupling is obtained when the fiber contacts a circular resonator. The use of a deformed resonator is a way to obtain high Q_c even when a fiber is in contact with the resonator to enable mechanical robustness.

D.4 Calculation of coupling coefficient at zero gap with different microresonator structures

To show the need for a deformed resonator structure to obtain high Q_c with fiber contact, I performed a theoretical study of the coupling coefficients. Since the fabricated octagonal resonator has a curvatures of 240 μm at the sidewall and 20 μm at the corner (Fig. D.2), I used mode profiles of circular toroid microresonators with curvatures of 240 and 20 μm to obtain the coupling strength γ_c of an octagonal resonator. I confirmed the validity of this approximation by comparing the obtained coupling constant with results obtained using a finite-difference time-domain method which is described in Ref. [179]. When a fiber couples with the resonator

D.4. Calculation of coupling coefficient at zero gap with different microresonator structures

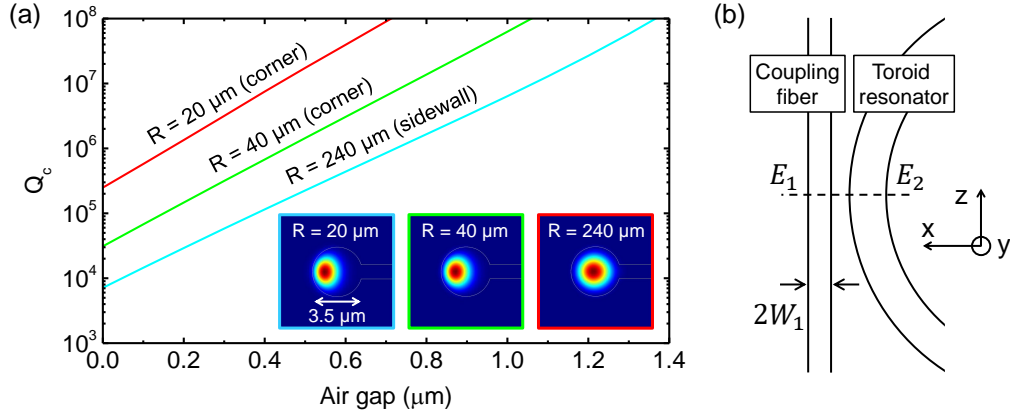


Fig. D.4: (a) Q_c with respect to the gap distance between the fiber and resonator. The insets show the cross sectional mode distributions of the whispering-gallery modes of a toroid resonator with a minor diameter of $3.5 \mu\text{m}$. These reveal the difference of mode distributions. (b) The structure used for the calculation.

rim, as shown in the inset of Fig. D.4(b), γ_c is given by the following equations [181, 182],

$$\gamma'_c = \frac{k_0(n_1^2 - n_2^2) \int_{-W_1}^{+W_1} E_1^* E_2 dx}{2n'_1 \int_{-\infty}^{+\infty} |E_2|^2 dx}, \quad (\text{D.2})$$

$$\gamma_c = \int_{-\infty}^{+\infty} \gamma'_c \exp\{-i(n'_1 - n'_2)k_0 z\} dz, \quad (\text{D.3})$$

where γ'_c is the coupling strength between two waveguides with different refractive indices. E_1 and E_2 are the electrical fields in the fiber and in the toroid resonator, respectively. n_1 , n_2 , n'_1 , and n'_2 are the refractive indices of the waveguide, vacuum, and the effective indices of the waveguide, vacuum, respectively. W_1 is the radius of the coupling fiber. k_0 is the wave number in vacuum. The light in the fiber propagates in the z direction as shown by the coordinate in Fig. D.4(b).

I calculate the electric field distributions of a toroid resonator and a coupling waveguide by using the finite element method (COMSOL Multiphysics) and the beam propagation method (BeamPROP), respectively. The whispering-gallery mode in a toroid resonator is shown in the inset of Fig. D.4(a). Figure D.4(b) shows the calculated Q_c as a function of the air gap distances for different resonator radiuses, which are obtained from the γ_c value derived by Eqs. (D.2) and (D.3). The minor diameter of the toroid (the waveguide width of the toroid microresonator) is $3.5 \mu\text{m}$ and the tapered fiber diameter $2W_1$ is $1.8 \mu\text{m}$. The stronger coupling (i.e. lower Q_c) is clearly obtained when the gap is small. In addition, Q_c is lower for smaller radius, because the electrical field distribution becomes closer to the surface.

This is of particular interest when the air gap distance is 0 nm. To compare a circular and an octagonal resonator, I calculated the coupling efficiency of a circular resonator with a diameter of $80 \mu\text{m}$, which is in the same size of the fabricated octagonal resonator. The result in Fig. D.4(a) shows that a circular resonator whose Q_i is larger than 10^6 always over-couples and it is not possible to obtain critical coupling when the fiber touches the resonator surface. On the other

hand, since an octagonal resonator has two different coupling points (sidewall and corner), it enables us to obtain Q_c with a value larger than 10^5 . The use of a thicker fiber enables the mode of the fiber to be confined more strongly in the core and allows a smaller coupling strength. However, if the waveguide is too thick, such as $2W_1 > 1.15 \mu\text{m}$, it becomes multi-mode and is no longer suitable for various applications. Hence it is difficult to obtain critical coupling with a circular resonator at contact. Another method that may achieve critical coupling at a zero gap is for the tapered fiber to make contact slightly offset from the center of the toroid resonator rim. However, in this case, a higher order mode will exhibit strong coupling, which makes observation of the fundamental mode extremely difficult and it even exhibits coupling between different modes. Again, this is not suitable for applications. Hence, the use of a deformed resonator that allows the fiber to touch the sidewall is a powerful way to achieve high Q_c that will allow us to have high mechanical stability.

D.5 Summary

The author fabricated a smooth octagonal silica toroid microresonator by combining KOH etching with a conventional toroid fabrication process. A Q of 2.2×10^4 was measured when the tapered fiber touched the toroid resonator. The characteristics of an octagonal toroid enable us to obtain a higher Q_c at the sidewall, and a lower Q_c at the corner. Even when the fiber is in contact with the resonator, a whispering-galley mode resonator system with mechanical robustness and high Q_c can be realized.

Appendix E

Constants, symbols, and relations

Table. E.1: The most important constants, symbols, and relations.

Symbol	Unit	Meaning
c	m/s	speed of light, $c = 2.99792458 \times 10^8$ m/s
\hbar	J·s/rad	Planck constant divided by 2π , $\hbar = 1.0545718 \times 10^{-34}$ J·s/rad
n	-	refractive index, $n = 1.44$ in silica
n_2	m ² /W	nonlinear refractive index, $n_2 = 2.2 \times 10^{-22}$ m ² /W in silica
m	-	mode number, $m \in \mathbb{N}$
μ	-	mode number offset from pump mode, $\mu \in \mathbb{Z}$
ω_0	rad·Hz	optical resonance frequency (of pump mode)
ω_p	rad·Hz	optical pump frequency
$\Delta\omega_0$	rad·Hz	pump detuning, $\Delta\omega_0 = \omega_p - \omega_0$
κ_i	s ⁻¹	intrinsic decay rate
κ_c	s ⁻¹	coupling rate to the external waveguide
κ	s ⁻¹	total cavity decay rate, $\kappa = \kappa_i + \kappa_c$
η	-	coupling parameter, $\eta = \kappa_c/\kappa$
K	-	coupling parameter, $K = \kappa_c/\kappa_i$
Q_i	-	intrinsic optical quality factor, $Q_i = \omega_0/\kappa_i$
Q_c	-	coupling optical quality factor, $Q_c = \omega_0/\kappa_c$
Q	-	total optical quality factor, $Q = \omega_0/\kappa$
t_r	s	roundtrip time
L	m	roundtrip length of the cavity, $L = t_r c/n$
R	m	cavity radius, $2\pi R \approx L$
D_1	rad·Hz	cavity free spectral range, $D_1/2\pi = d_1 = t_r^{-1}$
D_2	rad·Hz	second order dispersion, $D_2 > 0$ denotes anomalous dispersion, $D_2/2\pi = d_2$
D_3	rad·Hz	third order dispersion, $D_3/2\pi = d_3$
D_{int}	rad·Hz	total dispersion, $D_{\text{int}} = \omega_\mu - \omega_0 - D_1\mu = \frac{1}{2}D_2\mu^2 + \frac{1}{6}D_3\mu^3 \dots$
A_{eff}	m ²	effective mode area
g	rad·Hz	optical nonlinear coefficient, $g = (\hbar\omega_0^2 n_2 D_1)/(2\pi n A_{\text{eff}})$

Table. E.2: The most important constants, symbols, and relations.

Symbol	Unit	Meaning
P_{in}	W	input pump power to the waveguide
a_0	-	intracavity field (of pump mode), $ a_0 ^2$ corresponds to the intracavity photon number
s_{in}	-	input field to the waveguide, $\hbar\omega_0 s_{\text{in}} ^2 = P_{\text{in}}$
t	s	slow time
ϕ	rad	angular coordinate in the microresonator
a, b	-	internal field in the microresonator as functions of t and ϕ
Ω_{m}	rad·Hz	mechanical oscillation frequency
Γ_{m}	s^{-1}	mechanical damping rate
Γ_{opt}	s^{-1}	optomechanical damping rate
Γ_{eff}	s^{-1}	effective mechanical damping rate, $\Gamma_{\text{eff}} = \Gamma_{\text{m}} + \Gamma_{\text{opt}}$
Q_{m}	-	mechanical quality factor, $Q_{\text{m}} = \Omega_{\text{m}}/\Gamma_{\text{m}}$
m_{eff}	kg	effective mass
G	rad·Hz/m	resonance frequency shift per displacement, $G = \partial\omega_0/\partial x$
x_{ZPF}	m	mechanical zero-point fluctuation, $x_{\text{ZPF}} = \sqrt{\hbar/(2m_{\text{eff}}\Omega_{\text{m}})}$
g_{om}	rad·Hz	optomechanical single-photon coupling strength
f_{R}	-	Raman contribution coefficient, $f_{\text{R}} = 0.18$ in silica
g_{R}	m/W	Raman gain, $g_{\text{R}(\text{max})} = 6.2 \times 10^{-14}$ m/W at 13.2 THz shift in silica
G_{R}	rad·Hz	nonlinear Raman coefficient, $G_{\text{R}} = g_{\text{R}}(cD_1\hbar\omega_m)/(4\pi nA_{\text{eff}})$
σ	-	XPM coefficient, $\sigma = 2/3$ for orthogonal polarizations
ΔD_1	rad·Hz	difference of the cavity FSRs, $\Delta D_1 = D_{1(b)} - D_{1(a)}$
τ	-	generalized slow time, $\tau = \kappa t/2$
θ	rad	generalized angular coordinate in the microresonator
u, v	-	generalized internal field in the microresonator as functions of τ and θ
α	-	generalized detuning, $\alpha = -2\Delta\omega_0/\kappa$
β	-	generalized dispersion, $\beta = D_2/\kappa$
γ	-	generalized difference of the cavity FSRs, $\gamma = \Delta D_1/\kappa$
F	-	generalized parameter related to the optical coupling and nonlinearity, $F = (2s_{\text{in}}/\kappa)\sqrt{2g\kappa_c/\kappa}$
δ	-	pulse advance and delay in the azimuthal angular coordinate
B	-	soliton parameter related to the pulse peak and width
φ_0	rad	relative phase of the carrier from the soliton envelope
\mathcal{L}	-	Lagrangian density
L_0	-	Lagrangian, $L_0 = \int \mathcal{L} d\theta$
\mathcal{R}	-	perturbation

Appendix F

Abbreviations

Table. F.1: The list of important abbreviations

Abbreviation	Original expression
ASE	amplified spontaneous emission
BPF	bandpass filter
CW	continuous-wave
EDFA	erbium-doped fiber amplifier
ESA	electrical spectrum analyzer
FG	electrical function generator
FPC	fiber polarization controller
FSR	free spectral range
FWM	four-wave mixing
LLE	Lugiato-Lefever equation
MZI	fiber Mach-Zehnder interferometer
OMPO	optomechanical parametric oscillation
OSA	optical spectrum analyzer
OSC	oscilloscope
PD	photodetector
PM	phase modulator
PWM	power meter
RF	radio frequency
SBS	stimulated Brillouin scattering
SEM	scanning electron microscope
SG	electrical signal generator
SHG	second-harmonic generation
SPM	self-phase modulation
SRS	stimulated Raman scattering
THG	third-harmonic generation
TLD	tunable laser diode
XPM	cross-phase modulation

Bibliography

- [1] A. L. Schawlow and C. H. Townes, “Infrared and optical masers,” *Phys. Rev.* **112**, 1940–1949 (1958).
- [2] T. H. Maiman, “Stimulated optical radiation in ruby,” *Nature* **187**, 493–494 (1960).
- [3] K. J. Vahala, “Optical microcavities,” *Nature* **424**, 839–846 (2003).
- [4] A. B. Matsko, *Practical applications of microresonators in optics and photonics* (CRC Press, 2009).
- [5] P. Del’Haye, A. Schliesser, O. Arcizet, T. Wilken, R. Holzwarth, and T. Kippenberg, “Optical frequency comb generation from a monolithic microresonator,” *Nature* **450**, 1214–1217 (2007).
- [6] T. J. Kippenberg, R. Holzwarth, and S. A. Diddams, “Microresonator-based optical frequency combs,” *Science* **332**, 555–559 (2011).
- [7] A. M. Weiner, “Cavity solitons come of age,” *Nat. Photonics* **11**, 533–535 (2017).
- [8] F. Vollmer and S. Arnold, “Whispering-gallery-mode biosensing: label-free detection down to single molecules,” *Nat. Methods* **5**, 591–596 (2008).
- [9] F. Vollmer and L. Yang, “Label-free detection with high-Q microcavities: a review of biosensing mechanisms for integrated devices,” *Nanophotonics* **1**, 267–291 (2012).
- [10] M. R. Foreman, J. D. Swaim, and F. Vollmer, “Whispering gallery mode sensors,” *Adv. Opt. Photon.* **7**, 168–240 (2015).
- [11] A. E. Willner, S. Khaleghi, M. R. Chitgarha, and O. F. Yilmaz, “All-optical signal processing,” *J. Light. Technol.* **32**, 660–680 (2014).
- [12] H. Kimble, “The quantum internet,” *Nature* **453**, 1023–1030 (2008).
- [13] T. J. Kippenberg and K. J. Vahala, “Cavity optomechanics: back-action at the mesoscale,” *Science* **321**, 1172–1176 (2008).
- [14] M. Aspelmeyer, T. J. Kippenberg, and F. Marquardt, “Cavity optomechanics,” *Rev. Mod. Phys.* **86**, 1391–1452 (2014).

- [15] V. S. Ilchenko and A. B. Matsko, “Optical resonators with whispering-gallery modes-part ii: applications,” *IEEE J. Sel. Top. Quantum Electron.* **12**, 15–32 (2006).
- [16] M. L. Gorodetsky, A. A. Savchenkov, and V. S. Ilchenko, “Ultimate Q of optical microsphere resonators,” *Opt. Lett.* **21**, 453–455 (1996).
- [17] D. K. Armani, T. J. Kippenberg, S. M. Spillane, and K. J. Vahala, “Ultra-high-Q toroid microcavity on a chip,” *Nature* **421**, 925–928 (2003).
- [18] H. Lee, T. Chen, J. Li, K. Y. Yang, S. Jeon, O. Painter, and K. J. Vahala, “Chemically etched ultrahigh-Q wedge-resonator on a silicon chip,” *Nat. Photonics* **6**, 369–373 (2012).
- [19] I. S. Grudin, A. B. Matsko, A. A. Savchenkov, D. Strekalov, V. S. Ilchenko, and L. Maleki, “Ultra high Q crystalline microcavities,” *Opt. Comm.* **265**, 33–38 (2006).
- [20] C. Lecaplain, C. Javerzac-Galy, M. Gorodetsky, and T. Kippenberg, “Mid-infrared ultrahigh-Q resonators based on fluoride crystalline materials,” *Nat. Commun.* **7**, 13383 (2016).
- [21] V. S. Ilchenko, A. A. Savchenkov, A. B. Matsko, and L. Maleki, “Generation of Kerr frequency combs in a sapphire whispering gallery mode microresonator,” *Opt. Eng.* **53**, 122607 (2014).
- [22] C.-Y. Chao, W. Fung, and L. J. Guo, “Polymer microring resonators for biochemical sensing applications,” *IEEE J. Sel. Top. Quantum Electron.* **12**, 134–142 (2006).
- [23] F. Vanier, M. Rochette, N. Godbout, and Y.-A. Peter, “Raman lasing in As_2S_3 high-Q whispering gallery mode resonators,” *Opt. Lett.* **38**, 4966–4969 (2013).
- [24] J. Lin, Y. Xu, Z. Fang, M. Wang, J. Song, N. Wang, L. Qiao, W. Fang, and Y. Cheng, “Fabrication of high-Q lithium niobate microresonators using femtosecond laser micromachining,” *Sci. Rep.* **5**, 8072 (2015).
- [25] Y. Xuan, Y. Liu, L. T. Varghese, A. J. Metcalf, X. Xue, P.-H. Wang, K. Han, J. A. Jaramillo-Villegas, A. A. Noman, C. Wang, S. Kim, M. Teng, Y. J. Lee, B. Niu, L. Fan, J. Wang, D. E. Leaird, A. M. Weiner, and M. Qi, “High-Q silicon nitride microresonators exhibiting low-power frequency comb initiation,” *Optica* **3**, 1171–1180 (2016).
- [26] A. Griffith, J. Cardenas, C. B. Poitras, and M. Lipson, “High quality factor and high confinement silicon resonators using etchless process,” *Opt. Express* **20**, 21341–21345 (2012).
- [27] M. Ferrera, L. Razzari, D. Duchesne, R. Morandotti, Z. Yang, M. Liscidini, J. Sipe, S. Chu, B. Little, and D. Moss, “Low-power continuous-wave nonlinear optics in doped silica glass integrated waveguide structures,” *Nat. Photonics* **2**, 737–740 (2008).
- [28] H. Jung, C. Xiong, K. Y. Fong, X. Zhang, and H. X. Tang, “Optical frequency comb generation from aluminum nitride microring resonator,” *Opt. Lett.* **38**, 2810–2813 (2013).

-
- [29] L. Ottaviano, M. Pu, E. Semenova, and K. Yvind, “Low-loss high-confinement waveguides and microring resonators in AlGaAs-on-insulator,” *Opt. Lett.* **41**, 3996–3999 (2016).
- [30] B. Hausmann, I. Bulu, V. Venkataraman, P. Deotare, and M. Lončar, “Diamond nonlinear photonics,” *Nat. Photonics* **8**, 369–374 (2014).
- [31] E. Obrzud, S. Lecomte, and T. Herr, “Temporal solitons in microresonators driven by optical pulses,” *Nat. Photonics* **11**, 600–607 (2017).
- [32] D. J. Jones, S. A. Diddams, J. K. Ranka, A. Stentz, R. S. Windeler, J. L. Hall, and S. T. Cundiff, “Carrier-envelope phase control of femtosecond mode-locked lasers and direct optical frequency synthesis,” *Science* **288**, 635–639 (2000).
- [33] T. Udem, R. Holzwarth, and T. W. Hänsch, “Optical frequency metrology,” *Nature* **416**, 233–237 (2002).
- [34] S. T. Cundiff and J. Ye, “Colloquium: femtosecond optical frequency combs,” *Rev. Mod. Phys.* **75**, 325–342 (2003).
- [35] T. W. Hänsch, “Nobel lecture: passion for precision,” *Rev. Mod. Phys.* **78**, 1297–1309 (2006).
- [36] H. Schnatz, B. Lipphardt, J. Helmcke, F. Riehle, and G. Zinner, “First phase-coherent frequency measurement of visible radiation,” *Phys. Rev. Lett.* **76**, 18–21 (1996).
- [37] J. K. Ranka, R. S. Windeler, and A. J. Stentz, “Visible continuum generation in air–silica microstructure optical fibers with anomalous dispersion at 800 nm,” *Opt. Lett.* **25**, 25–27 (2000).
- [38] F. Leo, S. Coen, P. Kockaert, S.-P. Gorza, P. Emplit, and M. Haelterman, “Temporal cavity solitons in one-dimensional Kerr media as bits in an all-optical buffer,” *Nat. Photonics* **4**, 471–476 (2010).
- [39] T. Herr, V. Brasch, J. D. Jost, C. Y. Wang, N. M. Kondratiev, M. L. Gorodetsky, and T. J. Kippenberg, “Temporal solitons in optical microresonators,” *Nat. Photonics* **8**, 145–152 (2014).
- [40] T. Herr, “Solitons and dynamics of frequency comb formation in optical microresonators”, PhD. Thesis (Swiss Federal Institute of Technology in Lausanne, 2013).
- [41] T. J. Kippenberg, A. L. Gaeta, M. Lipson, and M. L. Gorodetsky, “Dissipative Kerr solitons in optical microresonators,” *Science* **361**, eaan8083 (2018).
- [42] X. Yi, Q.-F. Yang, K. Y. Yang, M.-G. Suh, and K. Vahala, “Soliton frequency comb at microwave rates in a high-Q silica microresonator,” *Optica* **2**, 1078–1085 (2015).

- [43] S. Zhang, J. Silver, L. D. Bino, F. Copie, M. Woodley, G. Ghalanos, A. Svela, N. Moroney, and P. Del’Haye, “ μ W-level microresonator solitons with extended stability range using an auxiliary laser,” arXiv preprint arXiv:1809.10030 (2018).
- [44] P.-H. Wang, J. A. Jaramillo-Villegas, Y. Xuan, X. Xue, C. Bao, D. E. Leaird, M. Qi, and A. M. Weiner, “Intracavity characterization of micro-comb generation in the single-soliton regime,” *Opt. Express* **24**, 10890–10897 (2016).
- [45] C. Joshi, J. K. Jang, K. Luke, X. Ji, S. A. Miller, A. Klenner, Y. Okawachi, M. Lipson, and A. L. Gaeta, “Thermally controlled comb generation and soliton modelocking in microresonators,” *Opt. Lett.* **41**, 2565–2568 (2016).
- [46] V. Brasch, M. Geiselmann, T. Herr, G. Lihachev, M. H. P. Pfeiffer, M. L. Gorodetsky, and T. J. Kippenberg, “Photonic chip-based optical frequency comb using soliton Cherenkov radiation,” *Science* **351**, 357–360 (2016).
- [47] Z. Gong, A. Bruch, M. Shen, X. Guo, H. Jung, L. Fan, X. Liu, L. Zhang, J. Wang, J. Li, J. Yan, and H. X. Tang, “High-fidelity cavity soliton generation in crystalline AlN micro-ring resonators,” *Opt. Lett.* **43**, 4366–4369 (2018).
- [48] M. H. P. Pfeiffer, C. Herkommer, J. Liu, H. Guo, M. Karpov, E. Lucas, M. Zervas, and T. J. Kippenberg, “Octave-spanning dissipative Kerr soliton frequency combs in Si₃N₄ microresonators,” *Optica* **4**, 684–691 (2017).
- [49] P. Del’Haye, A. Coillet, T. Fortier, K. Beha, D. C. Cole, K. Y. Yang, H. Lee, K. J. Vahala, S. B. Papp, and S. A. Diddams, “Phase-coherent microwave-to-optical link with a self-referenced microcomb,” *Nat. Photonics* **10**, 516–520 (2016).
- [50] P. Marin-Palomo, J. N. Kemal, M. Karpov, A. Kordts, J. Pfeifle, M. H. P. Pfeiffer, P. Trocha, S. Wolf, V. Brasch, M. H. Anderson, R. Rosenberger, K. Vijayan, W. Freude, T. J. Kippenberg, and C. Koos, “Microresonator-based solitons for massively parallel coherent optical communications,” *Nature* **546**, 274–279 (2017).
- [51] A. Fülöp, M. Mazur, A. Lorences-Riesgo, O. B. Helgason, P.-H. Wang, Y. Xuan, D. E. Leaird, M. Qi, P. A. Andrekson, A. M. Weiner, and V. Torres-Company, “High-order coherent communications using mode-locked dark-pulse Kerr combs from microresonators,” *Nat. Commun.* **9**, 1598 (2018).
- [52] J. Pfeifle, A. Coillet, R. Henriët, K. Saleh, P. Schindler, C. Weimann, W. Freude, I. V. Balakireva, L. Larger, C. Koos, and Y. K. Chembo, “Optimally coherent Kerr combs generated with crystalline whispering gallery mode resonators for ultrahigh capacity fiber communications,” *Phys. Rev. Lett.* **114**, 093902 (2015).
- [53] I. Coddington, N. Newbury, and W. Swann, “Dual-comb spectroscopy,” *Optica* **3**, 414–426 (2016).
- [54] T. Ideguchi, “Dual-comb spectroscopy,” *Opt. Photon. News* **28**, 32–39 (2017).

- [55] M.-G. Suh, Q.-F. Yang, K. Y. Yang, X. Yi, and K. J. Vahala, “Microresonator soliton dual-comb spectroscopy,” *Science* **354**, 600–603 (2016).
- [56] A. Dutt, C. Joshi, X. Ji, J. Cardenas, Y. Okawachi, K. Luke, A. L. Gaeta, and M. Lipson, “On-chip dual-comb source for spectroscopy,” *Sci. Adv.* **4**, e1701858 (2018).
- [57] M. Yu, Y. Okawachi, A. G. Griffith, N. Picqu 迺, M. Lipson, and A. L. Gaeta, “Silicon-chip-based mid-infrared dual-comb spectroscopy,” *Nat. Commun.* **9**, 1869 (2018).
- [58] C. Bao, M.-G. Suh, and K. Vahala, “Microresonator soliton dual-comb imaging,” arXiv preprint arXiv:1809.09766 (2018).
- [59] I. Coddington, W. C. Swann, L. Nenadovic, and N. R. Newbury, “Rapid and precise absolute distance measurements at long range,” *Nat. Photonics* **3**, 351–356 (2009).
- [60] M.-G. Suh and K. J. Vahala, “Soliton microcomb range measurement,” *Science* **359**, 884–887 (2018).
- [61] P. Trocha, M. Karpov, D. Ganin, M. H. P. Pfeiffer, A. Kordts, S. Wolf, J. Krockenberger, P. Marin-Palomo, C. Weimann, S. Randel, W. Freude, T. J. Kippenberg, and C. Koos, “Ultrafast optical ranging using microresonator soliton frequency combs,” *Science* **359**, 887–891 (2018).
- [62] R. A. McCracken, J. M. Charsley, and D. T. Reid, “A decade of astrocombs: recent advances in frequency combs for astronomy,” *Opt. Express* **25**, 15058–15078 (2017).
- [63] M.-G. Suh, X. Yi, Y.-H. Lai, S. Leifer, I. S. Grudinin, G. Vasisht, E. C. Martin, M. P. Fitzgerald, G. Doppmann, J. Wang, D. Mawet, S. B. Papp, S. A. Diddams, C. Beichman, and K. Vahala, “Searching for exoplanets using a microresonator astrocomb,” *Nat. Photonics* **13**, 25–30 (2019).
- [64] E. Obrzud, M. Rainer, A. Harutyunyan, M. H. Anderson, J. Liu, M. Geiselmann, B. Chazelas, S. Kundermann, S. Lecomte, M. Cecconi, A. Ghedina, E. Molinari, F. Pepe, F. Wildi, F. Bouchy, T. J. Kippenberg, and T. Herr, “A microphotonic astrocomb,” *Nat. Photonics* **13**, 31–35 (2019).
- [65] J. D. Jost, J. L. Hall, and J. Ye, “Continuously tunable, precise, single frequency optical signal generator,” *Opt. Express* **10**, 515–520 (2002).
- [66] D. T. Spencer, T. Drake, T. C. Briles, J. Stone, L. C. Sinclair, C. Fredrick, Q. Li, D. Westly, B. R. Ilic, A. Bluestone, N. Volet, T. Komljenovic, L. Chang, S. H. Lee, D. Y. Oh, M.-G. Suh, K. Y. Yang, M. H. P. Pfeiffer, T. J. Kippenberg, E. Norberg, L. Theogarajan, K. Vahala, N. R. Newbury, K. Srinivasan, J. E. Bowers, S. A. Diddams, and S. B. Papp, “An optical-frequency synthesizer using integrated photonics,” *Nature* **557**, 81–85 (2018).
- [67] X. Xue and A. M. Weiner, “Microwave photonics connected with microresonator frequency combs,” *Frontiers of Optoelectronics* **9**, 238–248 (2016).

Bibliography

- [68] T. M. Fortier, M. S. Kirchner, F. Quinlan, J. Taylor, J. C. Bergquist, T. Rosenband, N. Lemke, A. Ludlow, Y. Jiang, C. W. Oates, and S. A. Diddams, “Generation of ultrastable microwaves via optical frequency division,” *Nat. Photonics* **5**, 425–429 (2011).
- [69] W. Liang, D. Eliyahu, V. S. Ilchenko, A. A. Savchenkov, A. B. Matsko, D. Seidel, and L. Maleki, “High spectral purity Kerr frequency comb radio frequency photonic oscillator,” *Nat. Commun.* **6**, 7957 (2015).
- [70] W. Weng, E. Lucas, G. Lihachev, V. E. Lobanov, H. Guo, M. L. Gorodetsky, and T. J. Kippenberg, “Spectral purification of microwave signals with disciplined dissipative Kerr solitons,” *Phys. Rev. Lett.* **122**, 013902 (2019).
- [71] W. Liang, V. S. Ilchenko, A. A. Savchenkov, A. B. Matsko, D. Seidel, and L. Maleki, “Passively mode-locked Raman laser,” *Phys. Rev. Lett.* **105**, 143903 (2010).
- [72] J. Li, H. Lee, and K. J. Vahala, “Microwave synthesizer using an on-chip Brillouin oscillator,” *Nat. Commun.* **4**, 2097 (2013).
- [73] B. Stern, X. Ji, Y. Okawachi, A. L. Gaeta, and M. Lipson, “Battery-operated integrated frequency comb generator,” *Nature* **562**, 401–405 (2018).
- [74] A. S. Raja, A. S. Voloshin, H. Guo, S. E. Agafonova, J. Liu, A. S. Gorodnitskiy, M. Karpov, N. G. Pavlov, E. Lucas, R. R. Galiev, A. E. Shitikov, J. D. Jost, M. L. Gorodetsky, and T. J. Kippenberg, “Electrically pumped photonic integrated soliton microcomb,” arXiv preprint arXiv:1810.03909 (2018).
- [75] L. Maleki, “The optoelectronic oscillator,” *Nat. Photonics* **5**, 728–730 (2011).
- [76] G. Lin, A. Coillet, and Y. K. Chembo, “Nonlinear photonics with high-Q whispering-gallery-mode resonators,” *Adv. Opt. Photon.* **9**, 828–890 (2017).
- [77] C. H. Metzger and K. Karrai, “Cavity cooling of a microlever,” *Nature* **432**, 1002–1005 (2004).
- [78] H. Rokhsari, T. J. Kippenberg, T. Carmon, and K. J. Vahala, “Radiation-pressure-driven micro-mechanical oscillator,” *Opt. Express* **13**, 5293–5301 (2005).
- [79] J. Hofer, A. Schliesser, and T. J. Kippenberg, “Cavity optomechanics with ultrahigh-Q crystalline microresonators,” *Phys. Rev. A* **82**, 031804 (2010).
- [80] T. Carmon and K. J. Vahala, “Modal spectroscopy of optoexcited vibrations of a micron-scale on-chip resonator at greater than 1 GHz frequency,” *Phys. Rev. Lett.* **98**, 123901 (2007).
- [81] T. Carmon, H. Rokhsari, L. Yang, T. J. Kippenberg, and K. J. Vahala, “Temporal behavior of radiation-pressure-induced vibrations of an optical microcavity phonon mode,” *Phys. Rev. Lett.* **94**, 223902 (2005).

-
- [82] R. H. Stolen, C. Lin, and R. K. Jain, "A time-dispersion-tuned fiber Raman oscillator," *Appl. Phys. Lett.* **30**, 340–342 (1977).
- [83] R. H. Stolen, C. Lee, and R. K. Jain, "Development of the stimulated Raman spectrum in single-mode silica fibers," *J. Opt. Soc. Am. B* **1**, 652–657 (1984).
- [84] O. Boyraz and B. Jalali, "Demonstration of a silicon Raman laser," *Opt. Express* **12**, 5269–5273 (2004).
- [85] S. M. Spillane, T. J. Kippenberg, and K. J. Vahala, "Ultralow-threshold Raman laser using a spherical dielectric microcavity," *Nature* **415**, 621–623 (2002).
- [86] T. J. Kippenberg, S. M. Spillane, B. Min, and K. J. Vahala, "Theoretical and experimental study of stimulated and cascaded Raman scattering in ultrahigh-Q optical microcavities," *IEEE J. Sel. Topics Quantum Electron.* **10**, 1219–1228 (2004).
- [87] Ş. K. Özdemir, J. Zhu, X. Yang, B. Peng, H. Yilmaz, L. He, F. Monifi, S. H. Huang, G. L. Long, and L. Yang, "Highly sensitive detection of nanoparticles with a self-referenced and self-heterodyned whispering-gallery Raman microlaser," *Proc. Natl. Acad. Sci. USA* **111**, E3836–E3844 (2014).
- [88] Y. Ooka, Y. Yang, J. Ward, and S. N. Chormaic, "Raman lasing in a hollow, bottle-like microresonator," *Appl. Phys Express* **8**, 092001 (2015).
- [89] T. Kato, A. Hori, R. Suzuki, S. Fujii, T. Kobatake, and T. Tanabe, "Transverse mode interaction via stimulated Raman scattering comb in a silica microcavity," *Opt. Express* **25**, 857–866 (2017).
- [90] Q.-F. Yang, X. Yi, K. Y. Yang, and K. Vahala, "Stokes solitons in optical microcavities," *Nat. Phys.* **13**, 53–57 (2017).
- [91] H. Rong, S. Xu, Y.-H. Kuo, V. Sih, O. Cohen, O. Raday, and M. Paniccia, "Low-threshold continuous-wave Raman silicon laser," *Nat. Photonics* **1**, 232–237 (2007).
- [92] H. Rong, S. Xu, O. Cohen, O. Raday, M. Lee, V. Sih, and M. Paniccia, "A cascaded silicon Raman laser," *Nat. Photonics* **2**, 170–174 (2008).
- [93] I. S. Grudinin and L. Maleki, "Ultralow-threshold Raman lasing with CaF₂ resonators," *Opt. Lett.* **32**, 166–168 (2007).
- [94] G. Lin and Y. K. Chembo, "Phase-locking transition in Raman combs generated with whispering gallery mode resonators," *Opt. Lett.* **41**, 3718–3721 (2016).
- [95] F. Vanier, Y.-A. Peter, and M. Rochette, "Cascaded Raman lasing in packaged high quality As₂S₃ microspheres," *Opt. Express* **22**, 28731–28739 (2014).

Bibliography

- [96] B.-B. Li, Y.-F. Xiao, M.-Y. Yan, W. R. Clements, and Q. Gong, “Low-threshold Raman laser from an on-chip, high-Q, polymer-coated microcavity,” *Opt. Lett.* **38**, 1802–1804 (2013).
- [97] P. Latawiec, V. Venkataraman, M. J. Burek, B. J. M. Hausmann, I. Bulu, and M. Lončar, “On-chip diamond Raman laser,” *Optica* **2**, 924–928 (2015).
- [98] X. Liu, C. Sun, B. Xiong, L. Wang, J. Wang, Y. Han, Z. Hao, H. Li, Y. Luo, J. Yan, T. Wei, Y. Zhang, and J. Wang, “Integrated continuous-wave aluminum nitride Raman laser,” *Optica* **4**, 893–896 (2017).
- [99] A. G. Griffith, M. Yu, Y. Okawachi, J. Cardenas, A. Mohanty, A. L. Gaeta, and M. Lipson, “Coherent mid-infrared frequency combs in silicon-microresonators in the presence of Raman effects,” *Opt. Express* **24**, 13044–13050 (2016).
- [100] X. Liu, C. Sun, B. Xiong, L. Wang, J. Wang, Y. Han, Z. Hao, H. Li, Y. Luo, J. Yan, T. Wei, Y. Zhang, and J. Wang, “Integrated high-Q crystalline AlN microresonators for broadband Kerr and Raman frequency combs,” *ACS Photonics* **5**, 1943–1950 (2018).
- [101] C. Milián, A. V. Gorbach, M. Taki, A. V. Yulin, and D. V. Skryabin, “Solitons and frequency combs in silica microring resonators: interplay of the Raman and higher-order dispersion effects,” *Phys. Rev. A* **92**, 033851 (2015).
- [102] M. Karpov, H. Guo, A. Kordts, V. Brasch, M. H. P. Pfeiffer, M. Zervas, M. Geiselmann, and T. J. Kippenberg, “Raman self-frequency shift of dissipative Kerr solitons in an optical microresonator,” *Phys. Rev. Lett.* **116**, 103902 (2016).
- [103] A. V. Cherenkov, N. M. Kondratiev, V. E. Lobanov, A. E. Shitikov, D. V. Skryabin, and M. L. Gorodetsky, “Raman-Kerr frequency combs in microresonators with normal dispersion,” *Opt. Express* **25**, 31148–31158 (2017).
- [104] Y. Okawachi, M. Yu, V. Venkataraman, P. M. Latawiec, A. G. Griffith, M. Lipson, M. Lončar, and A. L. Gaeta, “Competition between Raman and Kerr effects in microresonator comb generation,” *Opt. Lett.* **42**, 2786–2789 (2017).
- [105] S. Fujii, T. Kato, R. Suzuki, A. Hori, and T. Tanabe, “Transition between Kerr comb and stimulated Raman comb in a silica whispering gallery mode microcavity,” *J. Opt. Soc. Am. B* **35**, 100–106 (2018).
- [106] Y. K. Chembo, I. S. Grudinin, and N. Yu, “Spatiotemporal dynamics of Kerr-Raman optical frequency combs,” *Phys. Rev. A* **92**, 043818 (2015).
- [107] N. G. Pavlov, G. Lihachev, S. Koptyaev, E. Lucas, M. Karpov, N. M. Kondratiev, I. A. Bilenko, T. J. Kippenberg, and M. L. Gorodetsky, “Soliton dual frequency combs in crystalline microresonators,” *Opt. Lett.* **42**, 514–517 (2017).

-
- [108] C. Bao, P. Liao, A. Kordts, L. Zhang, A. Matsko, M. Karpov, M. H. Pfeiffer, G. Xie, Y. Cao, Y. Yan, A. Almain, Z. Zhao, A. Mohajerin-Ariaei, A. Fallahpour, F. Alishahi, M. Tur, L. Maleki, T. J. Kippenberg, and A. E. Willner, “Orthogonally polarized Kerr frequency combs,” arXiv preprint arXiv:1705.05045 (2017).
- [109] X. Zhao, J. M. Silver, L. D. Bino, and P. Del’Haye, “Dual comb generation in a single microresonator,” Conference on Lasers and Electro-Optics p. STh3L.4 (2017).
- [110] W. Wang, W. Zhang, Z. Lu, S. T. Chu, B. E. Little, Q. Yang, L. Wang, and W. Zhao, “Self-locked orthogonal polarized dual comb in a microresonator,” *Photon. Res.* **6**, 363–367 (2018).
- [111] E. Lucas, G. Lihachev, R. Bouchand, N. G. Pavlov, A. S. Raja, M. Karpov, M. L. Gorodetsky, and T. J. Kippenberg, “Spatial multiplexing of soliton microcombs,” *Nat. Photonics* **12**, 699–705 (2018).
- [112] T. Hansson, M. Bernard, and S. Wabnitz, “Modulational instability of nonlinear polarization mode coupling in microresonators,” *J. Opt. Soc. Am. B* **35**, 835–841 (2018).
- [113] M. J. Weber, *Handbook of optical materials*, vol. 19 (CRC Press, 2002).
- [114] A. A. Savchenkov, A. B. Matsko, V. S. Ilchenko, N. Yu, and L. Maleki, “Whispering-gallery-mode resonators as frequency references. ii. stabilization,” *J. Opt. Soc. Am. B* **24**, 2988–2997 (2007).
- [115] J. S. Levy, A. Gondarenko, M. A. Foster, A. C. Turner-Foster, A. L. Gaeta, and M. Lipson, “CMOS-compatible multiple-wavelength oscillator for on-chip optical interconnects,” *Nat. Photonics* **4**, 37–40 (2009).
- [116] P. Del’Haye, S. A. Diddams, and S. B. Papp, “Laser-machined ultra-high-Q microrod resonators for nonlinear optics,” *Appl. Phys. Lett.* **102**, 221119 (2013).
- [117] J. C. Knight, G. Cheung, F. Jacques, and T. A. Birks, “Phase-matched excitation of whispering-gallery-mode resonances by a fiber taper,” *Opt. Lett.* **22**, 1129–1131 (1997).
- [118] M. Cai, O. Painter, and K. J. Vahala, “Observation of critical coupling in a fiber taper to a silica-microsphere whispering-gallery mode system,” *Phys. Rev. Lett.* **85**, 74–77 (2000).
- [119] S. M. Spillane, T. J. Kippenberg, O. J. Painter, and K. J. Vahala, “Ideality in a fiber-taper-coupled microresonator system for application to cavity quantum electrodynamics,” *Phys. Rev. Lett.* **91**, 043902 (2003).
- [120] T. Carmon, L. Yang, and K. J. Vahala, “Dynamical thermal behavior and thermal self-stability of microcavities,” *Opt. Express* **12**, 4742–4750 (2004).
- [121] K. Y. Yang, K. Beha, D. C. Cole, X. Yi, P. Del’Haye, H. Lee, J. Li, D. Y. Oh, S. A. Diddams, S. B. Papp, and K. J. Vahala, “Broadband dispersion-engineered microresonator on a chip,” *Nat. Photonics* **10**, 316–320 (2016).

Bibliography

- [122] K. Luke, Y. Okawachi, M. R. E. Lamont, A. L. Gaeta, and M. Lipson, “Broadband mid-infrared frequency comb generation in a Si_3N_4 microresonator,” *Opt. Lett.* **40**, 4823–4826 (2015).
- [123] P. Del’Haye, O. Arcizet, M. L. Gorodetsky, R. Holzwarth, and T. J. Kippenberg, “Frequency comb assisted diode laser spectroscopy for measurement of microcavity dispersion,” *Nat. Photonics* **3**, 529–533 (2009).
- [124] S.-W. Huang, H. Zhou, J. Yang, J. F. McMillan, A. Matsko, M. Yu, D.-L. Kwong, L. Maleki, and C. W. Wong, “Mode-locked ultrashort pulse generation from on-chip normal dispersion microresonators,” *Phys. Rev. Lett.* **114**, 053901 (2015).
- [125] X. Yi, “Physics and applications of microresonator solitons and electro-optic frequency combs”, PhD. Thesis (California Institute of Technology, 2017).
- [126] G. P. Agrawal, *Nonlinear Fiber Optics* (Academic Press, 2013).
- [127] T. Carmon and K. J. Vahala, “Visible continuous emission from a silica microphotonic device by third-harmonic generation,” *Nat. Phys.* **3**, 430–435 (2007).
- [128] D. Farnesi, A. Barucci, G. C. Righini, S. Berneschi, S. Soria, and G. Nunzi Conti, “Optical frequency conversion in silica-whispering-gallery-mode microspherical resonators,” *Phys. Rev. Lett.* **112**, 093901 (2014).
- [129] T. J. Kippenberg, S. M. Spillane, and K. J. Vahala, “Kerr-nonlinearity optical parametric oscillation in an ultrahigh-Q toroid microcavity,” *Phys. Rev. Lett.* **93**, 083904 (2004).
- [130] A. A. Savchenkov, A. B. Matsko, D. Strekalov, M. Mohageg, V. S. Ilchenko, and L. Maleki, “Low threshold optical oscillations in a whispering gallery mode CaF_2 resonator,” *Phys. Rev. Lett.* **93**, 243905 (2004).
- [131] I. S. Grudinin, A. B. Matsko, and L. Maleki, “Brillouin lasing with a CaF_2 whispering gallery mode resonator,” *Phys. Rev. Lett.* **102**, 043902 (2009).
- [132] V. Braginski and A. Manukin, “Ponderomotive effects of electromagnetic radiation,” *Sov. Phys. JETP* **25**, 653–655 (1967).
- [133] T. J. Kippenberg, H. Rokhsari, T. Carmon, A. Scherer, and K. J. Vahala, “Analysis of radiation-pressure induced mechanical oscillation of an optical microcavity,” *Phys. Rev. Lett.* **95**, 033901 (2005).
- [134] A. Schliesser, P. Del’Haye, N. Nooshi, K. J. Vahala, and T. J. Kippenberg, “Radiation pressure cooling of a micromechanical oscillator using dynamical backaction,” *Phys. Rev. Lett.* **97**, 243905 (2006).
- [135] Y. K. Chembo, “Kerr optical frequency combs: theory, applications and perspectives,” *Nanophotonics* **5**, 214–230 (2016).

-
- [136] Y. K. Chembo and N. Yu, “Modal expansion approach to optical-frequency-comb generation with monolithic whispering-gallery-mode resonators,” *Phys. Rev. A* **82**, 033801 (2010).
- [137] A. B. Matsko, A. A. Savchenkov, W. Liang, V. S. Ilchenko, D. Seidel, and L. Maleki, “Mode-locked Kerr frequency combs,” *Opt. Lett.* **36**, 2845–2847 (2011).
- [138] Y. K. Chembo and C. R. Menyuk, “Spatiotemporal Lugiato-Lefever formalism for Kerr-comb generation in whispering-gallery-mode resonators,” *Phys. Rev. A* **87**, 053852 (2013).
- [139] S. Coen, H. G. Randle, T. Sylvestre, and M. Erkintalo, “Modeling of octave-spanning Kerr frequency combs using a generalized mean-field Lugiato-Lefever model,” *Opt. Lett.* **38**, 37–39 (2013).
- [140] F. Ferdous, H. Miao, D. E. Leaird, K. Srinivasan, J. Wang, L. Chen, L. T. Varghese, and A. M. Weiner, “Spectral line-by-line pulse shaping of on-chip microresonator frequency combs,” *Nat. Photonics* **5**, 770–776 (2011).
- [141] T. Herr, K. Hartinger, J. Riemensberger, C. Y. Wang, E. Gavartin, R. Holzwarth, M. L. Gorodetsky, and T. J. Kippenberg, “Universal formation dynamics and noise of Kerr-frequency combs in microresonators,” *Nat. Photonics* **6**, 480–487 (2012).
- [142] P. Del’Haye, A. Coillet, W. Loh, K. Beha, S. B. Papp, and S. A. Diddams, “Phase steps and resonator detuning measurements in microresonator frequency combs,” *Nat. Commun.* **6**, 5668 (2015).
- [143] Y. Liu, Y. Xuan, X. Xue, P.-H. Wang, S. Chen, A. J. Metcalf, J. Wang, D. E. Leaird, M. Qi, and A. M. Weiner, “Investigation of mode coupling in normal-dispersion silicon nitride microresonators for Kerr frequency comb generation,” *Optica* **1**, 137–144 (2014).
- [144] X. Xue, Y. Xuan, P.-H. Wang, Y. Liu, D. E. Leaird, M. Qi, and A. M. Weiner, “Normal-dispersion microcombs enabled by controllable mode interactions,” *Laser Photonics Rev.* **9**, L23–L28 (2015).
- [145] X. Xue, Y. Xuan, Y. Liu, P.-H. Wang, S. Chen, J. Wang, D. E. Leaird, M. Qi, and A. M. Weiner, “Mode-locked dark pulse Kerr combs in normal-dispersion microresonators,” *Nat. Photonics* **9**, 594–600 (2015).
- [146] P. Grelu, *Nonlinear optical cavity dynamics: from microresonators to fiber lasers* (John Wiley & Sons, 2015).
- [147] T. Herr, V. Brasch, J. D. Jost, I. Mirgorodskiy, G. Lihachev, M. L. Gorodetsky, and T. J. Kippenberg, “Mode spectrum and temporal soliton formation in optical microresonators,” *Phys. Rev. Lett.* **113**, 123901 (2014).

Bibliography

- [148] A. Schließer, “Cavity optomechanics and optical frequency comb generation with silica whispering-gallery-mode microresonators”, PhD. Thesis (Ludwig Maximilian University of Munich, 2009).
- [149] V. B. Braginsky, S. E. Strigin, and S. P. Vyatchanin, “Parametric oscillatory instability in Fabry-Perot interferometer,” *Phys. Lett. A* **287**, 331–338 (2001).
- [150] A. Coillet, I. Balakireva, R. Henriet, K. Saleh, L. Larger, J. M. Dudley, C. R. Menyuk, and Y. K. Chembo, “Azimuthal turing patterns, bright and dark cavity solitons in Kerr combs generated with whispering-gallery-mode resonators,” *IEEE Photon. J.* **5**, 6100409–6100409 (2013).
- [151] A. Coillet and Y. Chembo, “On the robustness of phase locking in Kerr optical frequency combs,” *Opt. Lett.* **39**, 1529–1532 (2014).
- [152] Z. Shen, Z.-H. Zhou, C.-L. Zou, F.-W. Sun, G.-P. Guo, C.-H. Dong, and G.-C. Guo, “Observation of high-Q optomechanical modes in the mounted silica microspheres,” *Photon. Res.* **3**, 243–247 (2015).
- [153] T. Kobatake, T. Kato, H. Itobe, Y. Nakagawa, and T. Tanabe, “Thermal effects on Kerr comb generation in a CaF₂ whispering-gallery mode microcavity,” *IEEE Photon. J.* **8**, 1–9 (2016).
- [154] D. Hollenbeck and C. D. Cantrell, “Multiple-vibrational-mode model for fiber-optic Raman gain spectrum and response function,” *J. Opt. Soc. Am. B* **19**, 2886–2892 (2002).
- [155] B. Min, L. Yang, and K. Vahala, “Controlled transition between parametric and Raman oscillations in ultrahigh-Q silica toroidal microcavities,” *Appl. Phys. Lett.* **87**, 181109 (2005).
- [156] S. B. Papp, P. Del’Haye, and S. A. Diddams, “Mechanical control of a microrod-resonator optical frequency comb,” *Phys. Rev. X* **3**, 031003 (2013).
- [157] D. V. Skryabin and A. V. Gorbach, “Colloquium: looking at a soliton through the prism of optical supercontinuum,” *Rev. Mod. Phys.* **82**, 1287–1299 (2010).
- [158] S. Fujii, A. Hori, T. Kato, R. Suzuki, Y. Okabe, W. Yoshiki, A.-C. Jinnai, and T. Tanabe, “Effect on Kerr comb generation in a clockwise and counter-clockwise mode coupled microcavity,” *Opt. Express* **25**, 28969–28982 (2017).
- [159] S. M. Link, D. J. H. C. Maas, D. Waldburger, and U. Keller, “Dual-comb spectroscopy of water vapor with a free-running semiconductor disk laser,” *Science* **356**, 1164–1168 (2017).
- [160] M. N. Islam, C. D. Poole, and J. P. Gordon, “Soliton trapping in birefringent optical fibers,” *Opt. Lett.* **14**, 1011–1013 (1989).

-
- [161] Y. S. Kivshar, “Soliton stability in birefringent optical fibers: analytical approach,” *J. Opt. Soc. Am. B* **7**, 2204–2209 (1990).
- [162] T. Ueda and W. L. Kath, “Dynamics of coupled solitons in nonlinear optical fibers,” *Phys. Rev. A* **42**, 563–571 (1990).
- [163] S. T. Cundiff, B. C. Collings, N. N. Akhmediev, J. M. Soto-Crespo, K. Bergman, and W. H. Knox, “Observation of polarization-locked vector solitons in an optical fiber,” *Phys. Rev. Lett.* **82**, 3988–3991 (1999).
- [164] N. Nishizawa and T. Goto, “Characteristics of pulse trapping by use of ultrashort soliton pulses in optical fibers across the zero-dispersion wavelength,” *Opt. Express* **10**, 1151–1159 (2002).
- [165] I. S. Grudinin and N. Yu, “Dispersion engineering of crystalline resonators via microstructuring,” *Optica* **2**, 221–224 (2015).
- [166] Y. Nakagawa, Y. Mizumoto, T. Kato, T. Kobatake, H. Itobe, Y. Kakinuma, and T. Tanabe, “Dispersion tailoring of a crystalline whispering gallery mode microcavity for a wide-spanning optical Kerr frequency comb,” *J. Opt. Soc. Am. B* **33**, 1913–1920 (2016).
- [167] S. Fujii, Y. Okabe, R. Suzuki, T. Kato, A. Hori, Y. Honda, and T. Tanabe, “Analysis of mode coupling assisted Kerr comb generation in normal dispersion system,” *IEEE Photon. J.* **10**, 4501511 (2018).
- [168] X. Yi, Q.-F. Yang, K. Youl Yang, and K. Vahala, “Active capture and stabilization of temporal solitons in microresonators,” *Opt. Lett.* **41**, 2037–2040 (2016).
- [169] Q.-F. Yang, X. Yi, K. Y. Yang, and K. Vahala, “Counter-propagating solitons in microresonators,” *Nat. Photonics* **11**, 560–564 (2017).
- [170] A. B. Matsko and L. Maleki, “On timing jitter of mode locked Kerr frequency combs,” *Opt. Express* **21**, 28862–28876 (2013).
- [171] X. Yi, Q.-F. Yang, K. Y. Yang, and K. Vahala, “Theory and measurement of the soliton self-frequency shift and efficiency in optical microcavities,” *Opt. Lett.* **41**, 3419–3422 (2016).
- [172] D. V. Strekalov and N. Yu, “Generation of optical combs in a whispering gallery mode resonator from a bichromatic pump,” *Phys. Rev. A* **79**, 041805 (2009).
- [173] W. Wang, S. T. Chu, B. E. Little, A. Pasquazi, Y. Wang, L. Wang, W. Zhang, L. Wang, X. Hu, G. Wang, H. Hu, Y. Su, F. Li, Y. Liu, and W. Zhao, “Dual-pump Kerr micro-cavity optical frequency comb with varying FSR spacing,” *Sci. Rep.* **6**, 28501 (2016).
- [174] S. B. Papp, P. Del’Haye, and S. A. Diddams, “Parametric seeding of a microresonator optical frequency comb,” *Opt. Express* **21**, 17615–17624 (2013).

Bibliography

- [175] C. Bao, P. Liao, A. Kordts, L. Zhang, M. Karpov, M. H. P. Pfeiffer, Y. Cao, Y. Yan, A. Almaiman, G. Xie, A. Mohajerin-Ariaei, L. Li, M. Ziyadi, S. R. Wilkinson, M. Tur, T. J. Kippenberg, and A. E. Willner, “Dual-pump generation of high-coherence primary Kerr combs with multiple sub-lines,” *Opt. Lett.* **42**, 595–598 (2017).
- [176] X.-F. Jiang, Y.-F. Xiao, C.-L. Zou, L. He, C.-H. Dong, B.-B. Li, Y. Li, F.-W. Sun, L. Yang, and Q. Gong, “Highly unidirectional emission and ultralow-threshold lasing from on-chip ultrahigh-Q microcavities,” *Adv. Mater.* **24**, OP260–OP264 (2012).
- [177] C. Li, L. Zhou, S. Zheng, and A. W. Poon, “Silicon polygonal microdisk resonators,” *IEEE J. Sel. Top. Quantum Electron.* **12**, 1438–1449 (2006).
- [178] H. Kudo, R. Suzuki, and T. Tanabe, “Whispering gallery modes in hexagonal microcavities,” *Phys. Rev. A* **88**, 023807 (2013).
- [179] T. Kato, W. Yoshiki, R. Suzuki, and T. Tanabe, “Octagonal silica toroidal microcavity for controlled optical coupling,” *Appl. Phys. Lett.* **101**, 121101 (2012).
- [180] I. Zobel and M. Kramkowska, “Development of etch hillocks on different Si(hkl) planes in silicon anisotropic etching,” *Surf. Sci.* **602**, 1712–1721 (2008).
- [181] B. E. Little, S. T. Chu, H. A. Haus, J. Foresi, and J. . Laine, “Microring resonator channel dropping filters,” *J. Light. Technol.* **15**, 998–1005 (1997).
- [182] Y. Liu, T. Chang, and A. E. Craig, “Coupled mode theory for modeling microring resonators,” *Opt. Eng.* **44**, 084601 (2005).

Acknowledgements

本研究は、慶應義塾大学大学院理工学研究科総合デザイン工学専攻田邊研究室において、田邊孝純教授のご指導の下で行われました。本論文の完成にあたって、多くの方々のご支援を受けましたので、特にお世話になった方々に感謝の意を述べさせていただきます。また、日本学術振興会の助成により、本研究が実りあるものになったことに感謝いたします。

初めに、本論文の主査である田邊孝純教授には、学部4年生から後期博士課程3年生までの長い期間、丁寧に指導して頂き大変感謝しております。田邊教授には、研究に対する取り組み方を一から教わり、理論から実験までいつも有益な助言を頂きました。また、その幅広い知識やプレゼンテーション能力、多くの人を巻き込む行動力にはいつも驚かされるばかりであり、理想となる研究者、社会人が近くにいたことが、自身にとって大きなプラスになったと考えております。加えて、国際学会への参加や海外留学などを後押しして頂き、Purdue UniversityやWashington University in St. Louisでの短期留学など多くの経験を積むことが出来ました。最後に、研究面の助言だけでなく、研究以外の相談に対しても親身になって対応して頂き、心から感謝御礼申し上げます。

本論文の審査にあたり、副査を引き受けて頂いた、慶應義塾大学理工学部の神成文彦教授、木下岳司准教授、佐々田博之教授、アメリカ合衆国のPurdue University, School of Electrical and Computer EngineeringのProf. Andrew M. Weinerにも感謝いたします。神成教授には、大変お忙しい中、本論文の構成から研究内容の細かい部分まで、丁寧にご指摘とご指導を頂きました。また学部生の頃から研究報告会などで、厳しさと優しさを持って、研究に関する議論を行って頂きました。木下准教授には、本論文の核となる部分で、鋭いご指摘とご指導を頂きました。また学部生の頃から、学生に寄り添った優しいご指導をして頂き、感謝しております。佐々田教授には、本論文の構成や物理学の基本である単位に関して、ご指摘とご指導を頂きました。また筆者がマイクロコムの研究を始めて、右も左もわからないような頃から、基本的な知識や装置に関することまで、丁寧にご指導いただきました。I would like to show my appreciation to Prof. Weiner for being my thesis committee and having given me some guidance on microcombs when I stayed in Purdue University.

研究室の第1期生であり、先輩である、小川陽平氏、加藤拓巳氏、工藤寛史氏、吉岐航氏とは、研究室の立ち上げという難しい時期を同時に過ごし、多くの経験を共有しました。特に、後期博士課程を修了した加藤氏と吉岐氏からは、長い期間、研究について様々な有益な助言を頂きました。加藤氏は、筆者が学部4年生の時から同じ研究テーマについて取り組み、研究で困難にぶつかったときは、一緒になってそれを乗り越える手助けをして頂きました。また、同氏は周囲のメンバーのモチベーションを上げ、特に筆者の研究チームをリーダーとして牽引して頂きました。吉岐氏の研究に対する姿勢は誰もが尊敬

Acknowledgements

するところであり、その研究室への多大な貢献が無ければ、本研究は遂行できなかつたと言っても過言ではありません。また、研究面だけでなく、普段からよく声をかけて頂いて大変嬉しく思っておりました。

研究室の第2期生であり、同期である、石川花帆氏、齊藤龍介氏、鐵本智大氏、西村治朗氏、伏見亮大氏は、それぞれに尊敬できる点が多くあり、時に迷惑をかけてしまうこともありましたが、彼らが同期で良かったと心から思っております。特に、後期博士課程を修了した鐵本氏とは、長い時間を研究室で共に過ごしました。同氏は、研究に対する真摯な姿勢、周囲の人に対して惜しみなく行動できること、海外で研究者として働きに出る実行力など、多くの見習うべき点を持ち合わせていました。

研究室の第3期生以降の後輩やポスドク、留学生、秘書の方々など、多くの良き研究室メンバーにも恵まれました。それぞれに多くの感謝している点がありますが、ここでは、本論文に関連する原著論文の連名に入っている、小島知也氏、藤井瞬氏、堀敦裕氏、久保田啓寛氏について書かせて頂きます。第3期生の小島氏には、シミュレーション計算について取り組んで頂き、その研究に対する勘の良さにはいつも驚かされました。同氏が初めて学ぶプログラミング言語にも関わらず、複雑なコードを数日で書き上げたことは、今でも深く印象に残っています。後期博士課程に在籍する、第5期生の藤井氏には、三期下の後輩でありながら対等、もしくはそれ以上の知識を持って研究の議論をして頂きました。また、同氏の研究に限らない幅広い知識や行動力によって、筆者の研究室生活が充実したものになった事に大変感謝しています。同じく第5期生の堀氏には、シミュレーション計算について取り組んで頂き、計算コードの高速化や自動化など、筆者がそれまで気付かなかつた多くの学びや成果を与えて頂きました。第6期生の久保田氏とは、微小光共振器の作製など多くの実験に共に取り組み、同氏に対する実験の信頼度は後輩の中でも特に高く、非常に頼りになる存在でした。

慶應義塾大学理工学部電子工学科の池原雅章教授には、修士課程修了後の進路に関して大変お世話になり、この場を借りて深く感謝とお詫びを申し上げます。また、グローバル環境システムリーダープログラム(GESL)在籍時には、慶應義塾大学理工学部機械工学科の植田利久教授と泰岡顕治教授、その他のスタッフの方々に、様々なサポートをして頂き感謝しております。

最後に、後期博士課程への進学に対して深い理解を示し、経済的にも精神的にも支えて頂いた両親と弟に感謝申し上げます。本論文を書き終えた後が筆者の新たなスタートであり、多くの方々に支えられていることを忘れずに、責任感を持って自身の意思で人生を歩んでいきたいと思っております。

List of publications and presentations

Publications (related to this thesis)

- [1] R. Suzuki, S. Fujii, A. Hori, and T. Tanabe, “Theoretical study on dual-comb generation and soliton trapping in a single microresonator with orthogonally polarized dual pumping,” *IEEE Photon. J.* **11**, 6100511 (2019) [<https://doi.org/10.1109/JPHOT.2018.2888637>].
- [2] R. Suzuki, A. Kubota, A. Hori, S. Fujii, and T. Tanabe, “Broadband gain induced Raman comb formation in a silica microresonator,” *J. Opt. Soc. Am. B* **35**, 933–938 (2018) [<https://doi.org/10.1364/JOSAB.35.000933>].
- [3] R. Suzuki, T. Kato, T. Kobatake, and T. Tanabe, “Suppression of optomechanical parametric oscillation in a toroid microcavity assisted by a Kerr comb,” *Opt. Express* **25**, 28806–28816 (2017) [<https://doi.org/10.1364/OE.25.028806>].

Other publications

- [1] S. Fujii, Y. Okabe, R. Suzuki, T. Kato, A. Hori, Y. Honda, and T. Tanabe, “Analysis of mode coupling assisted Kerr comb generation in normal dispersion system,” *IEEE Photon. J.* **10**, 4501511 (2018).
- [2] 田邊孝純, 鈴木良, 鐵本智大, 柿沼康弘, 「高 Q 値微小光共振器の作製と応用」, *応用物理* **87**, 181–186 (2018).
- [3] 藤井瞬, 鈴木良, 堀敦裕, 久保田啓寛, 田邊孝純, 「微小共振器におけるカーコムの数値シミュレーション法」, *レーザー研究* **46**, 97–102 (2018).
- [4] 田邊孝純, 鈴木良, 藤井瞬, 久保田啓寛, 堀敦裕, 「微小光共振器によるマイクロコム発生」, *レーザー研究* **46**, 86–91 (2018).
- [5] S. Fujii, T. Kato, R. Suzuki, A. Hori, and T. Tanabe, “Transition between Kerr comb and stimulated Raman comb in a silica whispering gallery mode microcavity,” *J. Opt. Soc. Amer. B* **35**, 100–106 (2018).
- [6] S. Fujii, A. Hori, T. Kato, R. Suzuki, Y. Okabe, W. Yoshiki, A. C.-Jinnai, and T. Tanabe, “Effect on Kerr comb generation in a clockwise and counter-clockwise mode coupled microcavity,” *Opt. Express* **25**, 28969–28982 (2017).

- [7] S. Fujii, T. Kato, R. Suzuki, and T. Tanabe, “Third-harmonic blue light generation from Kerr clustered combs and dispersive waves,” *Opt. Lett.* **42**, 2010–2013 (2017).
- [8] T. Kato, A. Hori, R. Suzuki, S. Fujii, T. Kobatake, and T. Tanabe, “Transverse mode interaction via stimulated Raman scattering comb in a silica microcavity,” *Opt. Express* **25**, 857–866 (2017).
- [9] T. Kato, A. C.-Jinnai, T. Nagano, T. Kobatake, R. Suzuki, W. Yoshiki, and T. Tanabe, “Hysteresis behavior of Kerr frequency comb generation in a high-quality-factor whispering gallery mode microcavity,” *Jpn. J. Appl. Phys.* **55**, 072201 (2016).
- [10] R. Suzuki, T. Kato, T. Tetsumoto, and T. Tanabe, “Octagonal toroid microcavity for mechanically robust optical coupling,” *AIP Advances* **5**, 057127 (2015) [<https://doi.org/10.1063/1.4921201>].
- [11] H. Kudo, R. Suzuki, and T. Tanabe, “Whispering gallery modes in hexagonal microcavities,” *Phys. Rev. A* **88**, 023807 (2013).
- [12] T. Kato, W. Yoshiki, R. Suzuki, and T. Tanabe, “Octagonal silica toroidal microcavity for controlled optical coupling,” *Appl. Phys. Lett.* **101**, 121101 (2012).

Presentations (international conference)

- [1] R. Suzuki, S. Fujii, A. Hori, and T. Tanabe, “Soliton trapping in a Kerr microresonator with orthogonally polarized dual-pumping,” Pacific Rim Conference on Lasers and Electro-Optics (CLEO Pacific Rim), W1B.3, Hong Kong, July 29–August 3 (2018).
- [2] R. Suzuki, A. Kubota, A. Hori, S. Fujii, and T. Tanabe, “Raman comb generation through broadband gain in a silica microresonator,” Conference on Lasers and Electro-Optics (CLEO), SW3A.7, San Jose, May 13–18 (2018).
- [3] R. Suzuki, A. Kubota, S. Fujii, A. Hori, T. Kato, and T. Tanabe, “Raman comb formation in silica rod microresonator,” Frontiers in Optics/Laser Science Conference (FiO/LS), JW3A.76, Washington DC, September 17–21 (2017).
- [4] R. Suzuki, T. Kato, T. Kobatake, and T. Tanabe, “Cavity optomechanical coupling to multiple resonances assisted by Kerr comb generation in toroid microcavity,” Conference on Lasers and Electro-Optics / Europe (CLEO/Europe), CD-P.7, Munich, June 25–29 (2017).
- [5] R. Suzuki, T. Kato, A. C.-Jinnai, T. Nagano, T. Kobatake, and T. Tanabe, “Kerr comb generation with suppressed cavity-optomechanical oscillation in toroid microcavity,” Conference on Lasers and Electro-Optics (CLEO), STu3Q.7, San Jose, June 5–10 (2016).
- [6] R. Suzuki, T. Kato, A. C.-Jinnai, T. Kobatake, S. Fujii, and T. Tanabe, “Effects with Kerr comb in silica toroid microcavity: Raman scattering and third harmonic generation,” Advances Lasers and Photon Sources Conference (ALPS), ALPS1-3, Yokohama, May 17–20 (2016).

-
- [7] R. Suzuki, A. C.-Jinnai, T. Nagano, T. Kobatake, T. Kato and T. Tanabe, “Influence of cavity optomechanics on Kerr frequency combs,” APS March Meeting, A51.00008, Baltimore, March 14–18 (2016).
- [8] R. Suzuki, T. Kato, T. Kobatake, and T. Tanabe, “RF noise measurement of a microcavity Kerr comb generated by dual pumping,” Advances Lasers and Photon Sources (ALPS), ALPS3-5, Yokohama, April 22–25 (2014).
- [9] R. Suzuki, T. Kato and T. Tanabe, “Octagonal toroid microcavity for mechanically robust coupling with optical fiber,” Conference on Lasers and Electro-Optics (CLEO), JTu4A.44, San Jose, June 9–14 (2013).

Presentations (domestic conference)

- [1] 鈴木良, 加藤拓巳, 小島知也, 田邊孝純, 「トロイド共振器における光カーコム発生時の共振器オプトメカニクス」, 応用物理学会春季学術講演会, 15p-E205-8, パシフィコ横浜, March 14–17 (2017).
- [2] 鈴木良, 小島知也, 加藤拓巳, 田邊孝純, 「シリカトロイド共振器を用いたパラメトリック発振のRFノイズ評価」, 応用物理学会春季学術講演会, 17p-F7-12, 青山学院大学相模原キャンパス, March 17–20 (2014).
- [3] 鈴木良, 加藤拓巳, 田邊孝純, 「8角形トロイド微小光共振器の光学特性評価」, 応用物理学会春季学術講演会, 28p-A2-4, 神奈川工科大学, March 27–30 (2013).
- [4] 鈴木良, 加藤拓巳, 田邊孝純, 「8角形トロイド微小光共振器の作製と光学特性評価」, Optics and Photonics Japan (OPJ), 24pPD2, タワーホール船堀, October 23–25 (2012).